# Towards Single Electron Interferometry

Nathan L. Johnson

Department of Electronic and Electrical Engineering

University College London

A thesis submitted for the degree of

Doctor of Philosophy

May 2017

# Declaration

I, Nathan Lee Johnson, confirm that the work presented in this thesis is my own. Where information has been derived or quoted from other sources, I confirm that this has been indicated in the thesis.

# Acknowledgements

Thanks are owed to many people I have met and worked with on this journey. First, thanks to Prof. Sir Michael Pepper, my principal supervisor, for support, encouragement and advice. Secondly, but no less importantly, thanks to Dr. Masaya Kataoka, my NPL supervisor, for giving me much support, on everything from practical techniques to paper writing, and always keeping a watchful eye over my experimental progress. Many thanks to my other colleagues in the NPL team: particularly Dr. Jonathan Fletcher, for invaluable assistance for practical techniques, and Dr. Patrick See for the fabrication, without whom there would be none of the samples in this project. Outside of NPL, special thanks to Dr. Clive Emary of Newcastle University, a collaborator who has who has helped me understand and model my at times anomalous - looking data, through our lengthy e-mail discussion and detailed notes. Thanks to you all for your patience and support.

*To Carmen, thank you for your patience and support.*

# Abstract

There have been many studies and suggested technological applications using the two dimensional electron system in the GaAs/AlGaAs heterostructure. These have mostly focused on the behaviour of electrons propagating at or close to the Fermi Energy. More recently, one such application of this two dimensional system is for an electron pump, which isolates electrons from the two dimensional electron gas and pumps them individually at energies typically 100 meV above the Fermi energy, using surface gates to create a dynamic quantum dot. This energy regime had been previously unobtainable. We can utilise the high accuracy output of the pump - consistency that each pumped electron has the same properties, to study fundamental single particle physics, and work towards technological schemes, at this high energy. In this work we set out to continue and extend the previous work in this field. We present new measurements that detail an electron detector barrier that we can use both as a sampling oscilloscope, with a bandwidth approaching 100 GHz, or to measure the wavepacket properties of electrons, including their energy and time of arrival with high resolution. After developing and establishing the electron detector, we detail a series of experiments that utilise it to measure the electron velocity, scattering mechanisms and wavepacket size. We show this work maps consistently to theory, and further, we begin to demonstrate control of the electron wavepacket, with the possibility that this hot electron system could have future technological applications. This is all put together in the construction of an interferometer, which seeks to complete our understanding of electrons in this system by measuring coherence of the wavefunction, a key step to demonstrating construction of a prescribed state.

# Contents

# List of Figures

# Chapter 1

# The Electron Pump: A Single Electron Source

## 1.0 Introduction

Historically, there have been few studies of fundamental single electron physics in the solid state, with most studies focusing on systems of interacting particles [1]. However, advancement of control and manipulation of single electrons in the solid state has now reached the levels required to move beyond simply generating current and into the realm where we begin to build nanoelectronic devices that utilise the properties of individual electrons, as this thesis demonstrates. The work detailed in this thesis is an initial investigation in to single electron electronics, and the rich spectrum of condensed matter physics that is encountered in trying to construct and understand such a system. The focus of this work is to demonstrate single electron interference. This would show coherence in this system, which is a key step to being able to utilise the electrons for potential quantum information applications.

In this work we will do this by utilising a single electron pump to capture and isolate electrons from a two dimensional electron gas that acts as a reservoir for the electrons. This is a device that uses electrostatic potentials to isolate electrons individually from a reservoir.

The reservoir we use is a two dimensional electron gas, a layer of electrons confined between layers in a GaAs/AlGaAs heterostructure. These isolated electrons are pumped, and leave the electron pump with an excess kinetic energy, and in the presence of a magnetic field, they will propagate in edge states that act as our waveguides. We then use a detector barrier, which can provide energy and temporal resolution of the electrons on arrival at the detector. By utilising different electron paths we can study fundamental electron physics, and this opens up the possibility of construction of single-electron based circuits. What we aim to show in this work is coherence of the electron wavepacket, as it propagates from pump to detector. This means that the electron wavefunction is determined by the action of the electron pump, and this state is preserved across the device, up to the detector. This is important to show if we wish to use this system for single-electron based circuits, including in quantum information protocols. In these uses, the electron pump could be used to create a specific state, which is then preserved along a path length. Arrival at the detector barrier, at given times or energies, could form a basis of a readout of a quantum information protocol, or entanglement scheme.

The necessary first step to realise these schemes is to show coherence across the device [2]. Decoherence processes, i.e. scattering mechanisms, will cause the wavefunction to change from that prescribed by the pump. If it can be shown that there is no decoherence bewteen pump and detector, then the pump can be used to make a prescribed state. One way of demonstrating coherence conclusively is to show interference. This is a pattern created by overlap of two electron wavefunctions, when we split the path taken by electrons leaving the pump. The visibility of the interference pattern is proportional to the congruence of the wavepackets in this system, so wavepackets of the same size will give the strongest interference pattern. Decoherence mechanisms are expected to change the wavepacket size, by changing its energy, and reduce the overlap and visibility.

In each chapter we will focus on each aspect of this system, working towards the goal of developing a system in which we can possibly find an interference pattern for pumped

electrons. In this first chapter, I will begin by introducing the electron pump as a current source, reviewing the field, and outlying the basic physics for single electron capture. This will focus on implementations, their uses, and the state of the art. From there I will proceed to discuss the single electron dynamics of the pump, the physics universal not just to this work, but all current implementations of single electron control in the solid state. I will discuss our method of single electron capture and control, demonstrate current quantisation, and briefly assess its stability. I will outline the fabrication and experimental method for creation of these devices. This will set the basis for forthcoming chapters in which we discuss experiments focused on the control of the electron pump's output - the single electrons themselves.

In chapter 2 we introduce the edge state system in which the pumped electrons propagate, and detail the detector barrier, and how we develop energy and temporal resolution of the electron wavepacket. We further this discussion by suggesting a technological scheme in which single electrons can sample a potential on the detector barrier, very similar to an oscilloscope. This electron detection technique forms the core of all the measurements made in this work, and is quite unique to this system.

In chapters 3 - 5 we implement the pump and detector barrier to study the single electrons produced by the pump. We begin by performing a time of flight measurement to find the electron velocity, which had not previously been directly measured. From the velocity we derive the potential profile in which the pumped electrons propagate, and by studying the field dependence, understand their motion. In chapter 4 we measure the rate of the principal mode of decoherence, the LO-mode phonon emission. We develop a scattering theory for this process, and show that by modification of the potential profile, we can suppress the emission rate by many orders of magnitude, which is zero for all practical purposes. In chapter 5 we delve more deeply into what the electron detector tells us about the wavepacket, deriving a relation for its temporal and energy size in terms of the pump action.

Finally, in chapter 6 we put all of the previous chapters' work together and attempt to

show interference, utilising what we understand of the pump, detector, and the potential profile environment. Although we were not successful in demonstrating interference, we certainly made much progress in understanding the electron propagation in this behaviour, being among the first to be fully quantitative regarding the electron velocity, phonon emission rates, and potential profile form.

Let us first return to the basis of this work: the single electron pump. We will discuss what it is, how it works, and how we fabricate and measure it. This should convince the reader that we can reliably use an electron pump to give us a stream of single electron wavepackets, each wavepacket being very similar, if not identical, to all others produced by the pump.

## 1.1 Single Electron Sources

With the development of transistors in the 1970s - 1980s beginning to pick up pace, and a solid body of physics behind it to support their working, the idea of 'single electron electronics' became within the realms of possibility [3]. Better fabrication techniques, principally in Molecular Beam Epitaxy (MBE) [4, 5] were allowing for purer, more ordered structures and heterostructures. Störmer [6] and Mimura [7] were amongst the first to develop a 2DEG embedded in a GaAs/AlGaAs heterostructure, and descendants of this first structure remain in use today, including in this work. The central idea is to create a potential well sandwiched between two layers of semiconductor - typically GaAs/AlGaAs (as in this work, but it is also possible in other III-V heterostructures). This well can then be populated by free (conduction band) electrons. The well is one dimensional, perpendicular to the plane of the layers, so electrons may move freely in the other two dimensions. Hence, this creates a two dimensional electron gas (2DEG), a layer of free electrons only constrained in one dimension. Much work has been conducted on the nature of electrons occupying the 2DEG, and their motion within the gas. However, in our electron pump system, we do not work at

the Fermi energy, but much higher ($\sim$ 100meV) energies [8], and so a lot of the richness of 2DEG phenomena are not present in our system and we shall not discuss them here. This presents an elegant, but different, electron system studied in this work.

The 2DEG and its high mobility are useful for constructing a single electron source. This is a source of single electrons, that should be able to produce a well defined current. One of the first demonstrations of this, and remains still a useful tool today, is the Quantum Point Contact (QPC). When a 2DEG is constrained to have similar dimensions to the electron Fermi wavelength by a gate, current quantisation is observed, such that the current passing the QPC when biased by a voltage $V$ displays conductance plateau at integer values of conductance quanta $2e^2/h$, with $e$ the electron charge and $h$ Planck's constant [9,10]. Since this discovery, other sources, based on a similar principle, have been demonstrated. These include hot barriers [11], tunneling junctions [12], mesoscopic capacitors [13, 14], and turnstiles [15] which have shown promising current quantisation. These work by electrons tunneling over a potential barrier in the presence of a bias (source-drain or quantum dot-drain). The above referenced works have demonstrated this process with single electron tunneling events. Another more recent single electron source is the tunable-barrier single electron pump. It has undergone much development by several groups, and is a candidate for being the most accurate current source available, and can be used to redefine the SI Ampere current unit, having been shown to have an accuracy better than $10^{-6}$ [16]. Again, this pump operates using similar physics to the other methods. This (almost) device independence arises due to the elegant electrostatic system that these devices exploit, which we shall detail next. In this work, we use exclusively the NPL electron pump in an AlGaAs/GaAs heterostructure as our single electron source. In the next section we discuss it extensively, and as mentioned, a lot of the following discussion will have an equivalent interpretation to the other types of source.

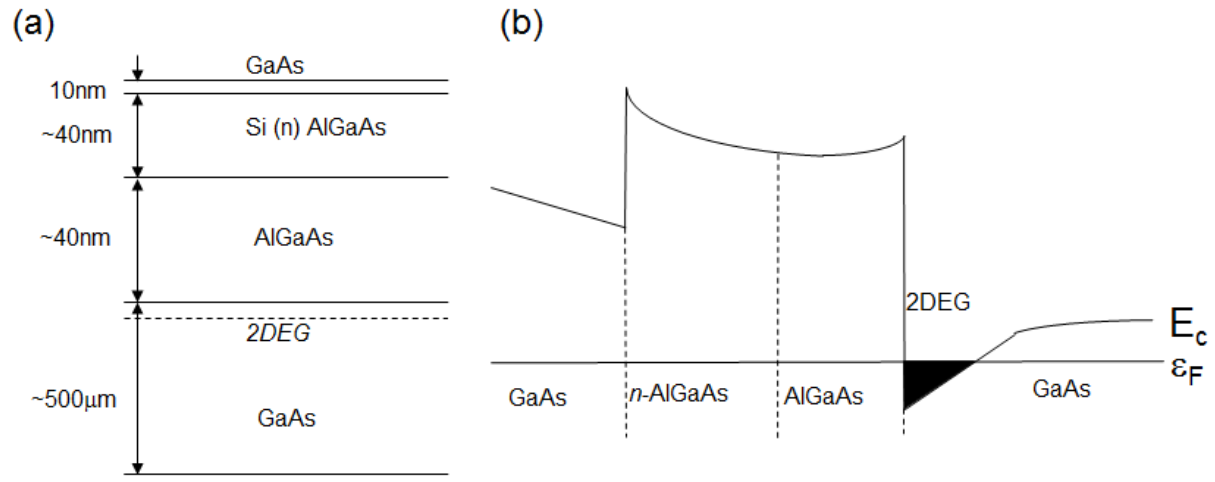


Figure 1.1: The heterostructure used in this work. (a) The spatial schematic, in the growth direction, with approximate dimensions. (b) The conduction band profile $E_c$, along the growth direction, in the populated case. The quantum well, shaded in black, defines a two dimensional electron gas (2DEG). $\epsilon_F$ is the Fermi Energy.

## 1.2 The NPL Electron Pump

The NPL electron pump serves as our source of electrons in all experiments in this work, and with its excellent accuracy, gives us identical single electron wavepackets with each cycle of the pump. We understand much of the mechanism by which it works although a few subtleties remain. We now detail the electron pump and its beautiful physics.

### 1.2.1 A source of electrons

We use the GaAs/AlGaAs heterostructure sketched in Fig. 1.1(a), drawn with its corresponding populated band structure in (b). On the surface, there is a 10nm GaAs cap to stop oxidation. The next layer is made of Si doped (n - type) AlGaAs, of dimension 40nm. The next layer, of AlGaAs, is a spacer of 40nm. For both layers of AlGaAs we require $Al_xGa_{1-x}As$; x $\sim$ 0.3. In the donor layer, Si level varies but is typically 1-2% ($\sim 10^{20}/cm^3$; c.f. AlGaAs density is $\sim 10^{22}/cm^3$); this must be chosen carefully to avoid parallel conduction. The undoped spacer AlGaAs presents a potential barrier relative to the doped

layer and the substrate beneath it, which serves to reduce the silicon impurity level near the 2DEG, which would reduce the electron mobility. The substrate wafer is the bottom layer of GaAs, of dimension $\sim$ 0.5mm. The bandgap of AlGaAs is different to that of GaAs (by about +300meV), which creates a heterojunction in which the two dimensional electron gas (2DEG) forms, $\sim$ 90nm below the surface. Some donors will ionize (the Silicon donates electrons from its $D^0$ state), with liberated charge collecting principally to the surface, but also downward into the quantum well at the heterointerface [17]. High mobility is achieved by noting there is little scattering off of the interface owing to well matched lattice constants in GaAs ($\sim$ 5.65Å) [18] and AlGaAs ($\sim$ 5.66Å) [19], differing to no more than $\sim$ 1% [20]. For carriers to sit towards the ground state of the potential well, we require cryogenic temperatures for formation of the 2DEG, typically below 100 K, and this work was performed partly in a He-3 cryostat with base temperature $\sim$ 300mK and partly in a dilution refrigerator with base temperature $\sim$ 30mK. Carrier concentration may be important for pump accuracy; a higher concentration should allow for a more easily defined quantum dot (QD), but it may suffer more heating from crosstalk with the pump drive. In this work we use a carrier concentration of 1.6-1.9 $\times 10^6$ cm$^{-2}$.

## 1.3 Device Fabrication

The heterostructure wafer is grown by the University of Cambridge by Molecular Beam Epitaxy (MBE); a typical wafer is large enough for many samples employed here and we batch process. Dr. Patrick See of NPL performs the rest of the fabrication, with assistance from Cambridge. Fig. 1.2(a) shows a photograph and micrograph of a sample, with the fabrication features annotated. Each image is a zoom-in of the boxed region of the one above.

A sample is 2mm square. Photoresist (PR) is spun onto the surface of the heterostructure. A mask is aligned on the top of the sample and ultraviolet (UV) light shone to break up the

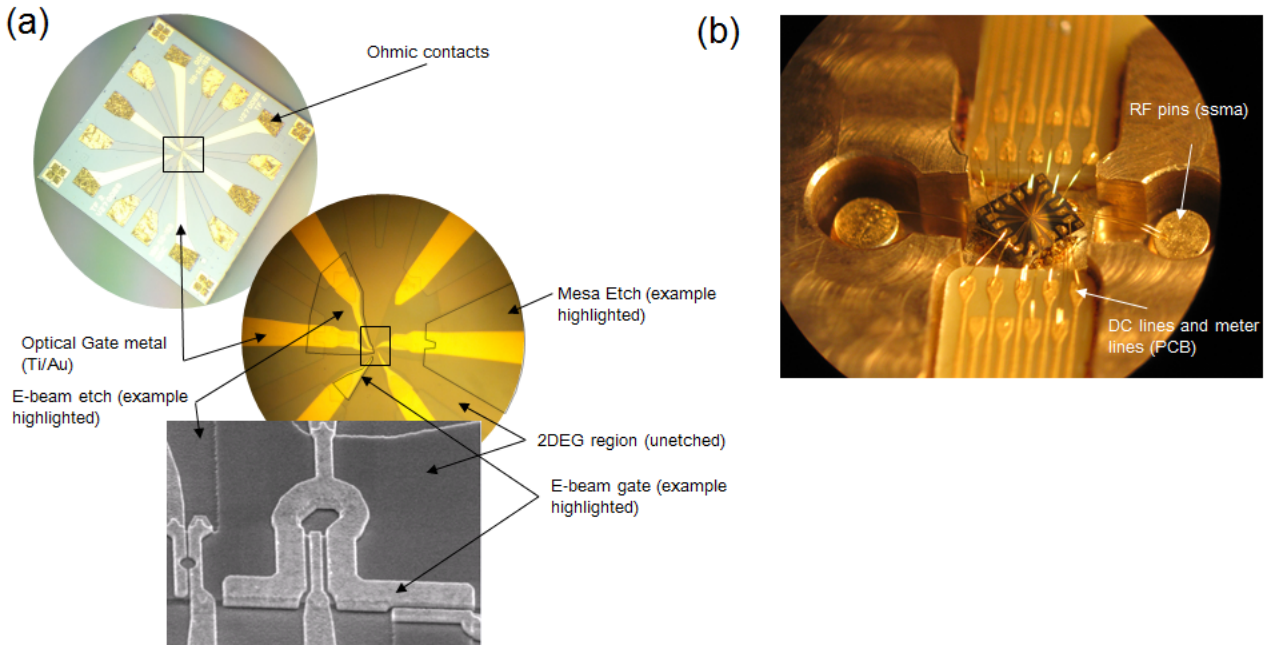


Figure 1.2: (a) From top to bottom, photographs (x1, x25) of a sample chip, and SEM micrograph, of the boxed region in the image above. Device features are highlighted and labelled. (b) Mounting of a sample on specialised sample holder with gold connecting bondwires from PCB (DC) and SSMA pins (RF AC).

PR not concealed by the mask. This loose PR is washed away in solvents. A chemical mesa etch is now used to remove material not concealed by the PR, down to the wafer to deplete the carriers (typically 100nm), and hence removing the possibility of 2DEG formation. This is labeled as the optically defined mesa etch on Fig. 1.2(a). Next, another mask is used to create ohmic contacts and ohmic bondpads for gate lines, at the edge of the sample (see Fig. 1.2(a)). Ohmic contacts are formed using a AuGeNi slug, and then annealed for 80s at 430 °C for spike-down. Gold is evaporated onto the surface of the contacts for bond adhesion. AuTi metallic gates are evaporated onto the surface from these contacts using another mask (the optical gates, as illustrated in Fig. 1.2(a)). For the active area of the device, we use first e-beam etching to define the channel geometry. This is use of e-beam lithography to break up resist, which can achieve finer spatial resolution, just as with writing. But, the resist is washed away, and then a chemical etch is used to remove typically 30-50nm of the heterostructure material. Again, this removes donors and prevents 2DEG formation and

conduction in this region. For the finer work we employ e-beam lithography to form AuTi gates, with typical thickness 40nm and width 50-300nm. These will form Schottky barriers when energised. Here we employ the above method for all samples; only the e-beam etch and lithography designs are changed to create the various geometries. In Fig. 1.2(b) we show a mounted sample on a custom made sample holder. DC gates connect via PCB and RF AC by SSMA pins, and gold bond wires connect all contacts to the side bond pads for ohmic contacts and gate lines.

## 1.4 The Electron Pump Mechanism

A micrograph of the electron pump is shown in Fig. 1.3 (a), with a schematic of the electrical connections made to it (we discuss the circuitry in more detail in the next section). The electron pump is defined by two surface gates spanning a 1.5 $\mu$m channel. A quantum dot (QD) is defined by the circular cut out between the gates. The two metallic gates form a potential barrier to the 2DEG when a negative voltage is applied. Gate $G_1$ is the "entrance" barrier and $G_2$ the "exit" barrier. We apply a fixed DC potential to $G_2$, $V_{G2}$, and an AC potential to $G_1$, $V_{G1}^{AC}$, (typically 0.1 - 1 GHz) with a DC offset $V_{G1}^{DC}$. The pump cycle is illustrated in Fig. 1.3(b). The sketch shows the potential profile created by the two gates, with the QD between them. Below each panel we show the approximate stage of the RF cycle $V_{G1}^{AC}$ at which that stage occurs. In case A, loading, the QD is populated by electrons in the low part of the AC potential, as $G_1$ drops below the Fermi energy $\epsilon_F$. As it rises (case B, backtunneling), the potential of $G_1$ rises higher than $\epsilon_F$ and the QD is isolated. At this point, backtunneling occurs, with excess electrons returning to the source. As the potential $V_{G1}^{AC}$ continues to rise (case C, stabilisation) the QD is stable with a single electron. Tunneling to source nor drain is preferred. Towards the maximum barrier height (case D, ejection), the dot confining potentials are imbalanced, causing forward tunneling to be favourable, and the electron is pumped.

The resultant pumped current, $I_p$, formed by the net motion of electrons from source to drain (left to right in Fig. 1.3 (a)), shows quantisation according to the number of charges pumped per cycle of $V_{G1}^{AC}$. This is elegantly expressed as $I_p = nef$, for $n$ charges pumped per cycle at a frequency $f$ of fundamental charge $e$. An example current trace of this quantisation is shown in Fig. 1.3 (c). If we map the potential (voltage) phase space $(V_{G1}^{DC}, V_{G2})$ of the two gates we see a characteristic shape to potential coordinates that give forward tunneling, which we call the "pump map". An example is shown in Fig. 1.3 (d). In the right side panel, we take the horizontal derivative $dI_p/dV_{G2}$ which more clearly shows the pump plateaus. The process outlined in Fig. 1.3(b) is approximately scalable to have a stable QD with multiple occupancy, giving the higher $n$ plateaus seen in Fig. 1.3(c),(d). Plateaus above the main one, at more positive $V_{G1}^{DC}$, are due to stably loading $> n$ electrons but pumping only $n$. We do not conduct the experiments described in this work in this regime.

The realisation of quantised current in this way was first reported by Blumenthal [21] with a $10^{-4}$ accuracy, although the same cycle had been demonstrated in different semiconductor systems (for example [22]).

This phenomenological explanation of the electron pump mechanism can be understood from the theory of quantum dots (QDs). Beenakker [1] was one of the first to lay down a comprehensive theory of QD transport. At its core is the constant-interaction (CI) model, a quasi-classical but effective description of the Coulomb Blockade [23–25]. This simple model states that for an electron in a quantum dot, all Coulomb interactions with all other electrons within and outside of the QD can be simply described as a capacitance $C$. For us this is the source, drain and two gates. Secondly, the available states and their spacing in the dot is not changed by the presence of nearby charges. Hence, the density of states in the QD is given by the single - particle time independent Schrödinger equation. This depends only upon the confinement of the dot, and magnetic confinement in field (we perform all of our measurements in a magnetic field perpendicular to the 2DEG plane). We can define the addition energy, i.e. the energy required to confine a second electron in the QD, as

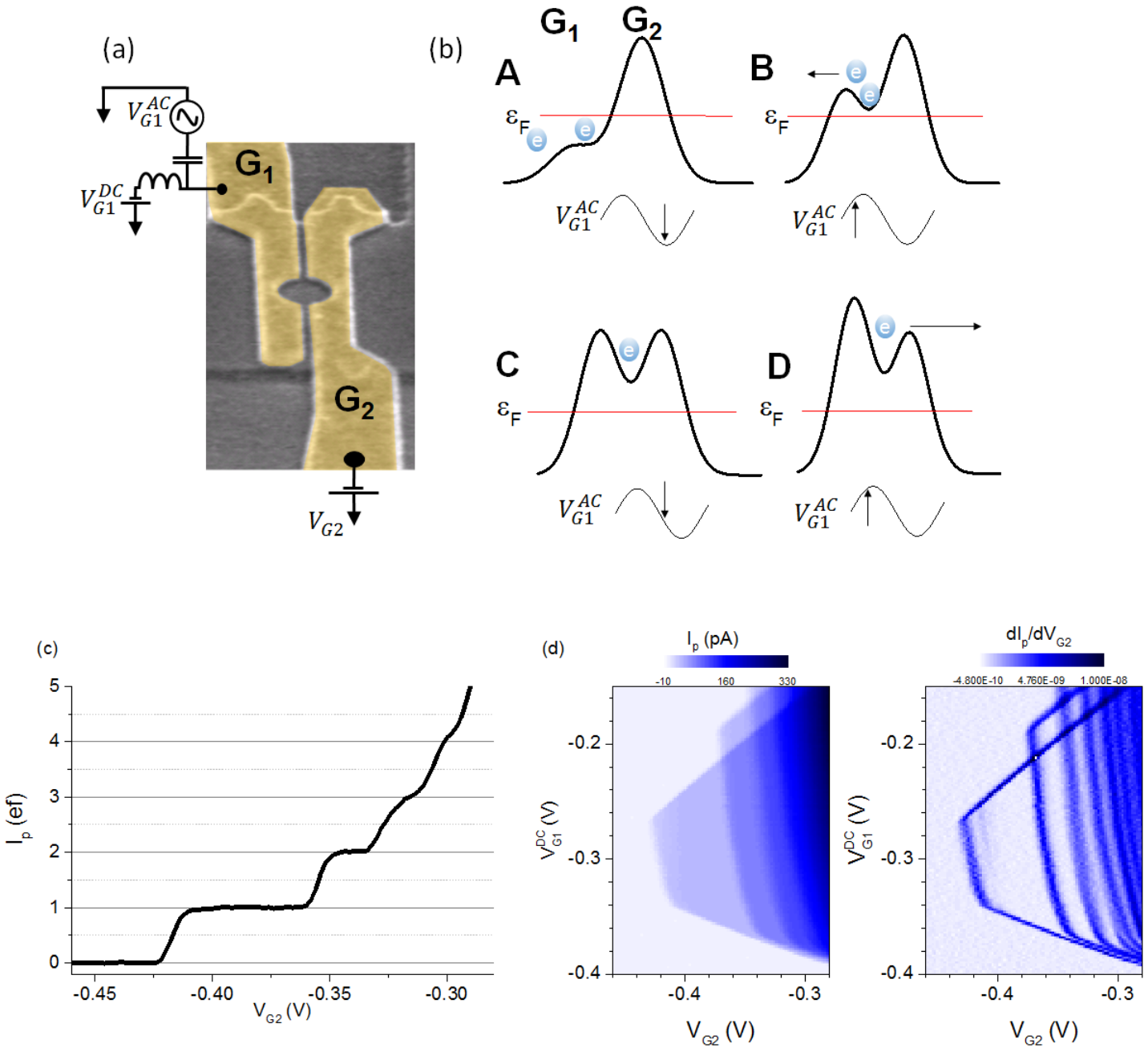


Figure 1.3: (a) Micrograph of the electron pump, with schematic of electrical contacts made to it. (b) Schematic of the potential profile during the pumping cycle, with the key stages of the pump cycle illustrated. Below, the approximate part of the driving waveform $V_{G1}^{AC}$ at each key stage. (c) Example pumped current trace $I_p$, showing clear quantisation (Taken at $V_{G1}^{DC} = -0.32V$ in plot (d)). (d) The pump map, with the colourscale current in the left panel and the horizontal derivative $dI_p/dV_{G2}$ for clarity in the right panel.

$E_a = e^2/C + \Delta E$, with $e^2/C$ the charging energy and $\Delta E$ the level spacing. Importantly, the addition energy is equal to the change in chemical potential, $\Delta\mu_{QD}$ when adding an electron to the QD. This defines the forward and backward tunneling conditions: forward or backward tunneling occurs if $\mu_{QD} > \mu_{drain}$ or $\mu_{QD} > \mu_{source}$ respectively.

For the level spacings we assume a parabolic confinement, and so solve the traditional quantum harmonic oscillator problem giving the energy levels as $E_{n,l} = (2n + |l| + 1)\hbar\omega_0$, for $\omega_0$ the frequency, $n$ the principal quantum number and $l$ the angular momentum quantum number, hence drawing analogues with atoms [24–26].

For this dynamic case, it was found empirically that certain parameters increase pump accuracy. Blumenthal [21] and others [16, 27–29] found decreasing accuracy with increasing frequency (particularly into the GHz). Perpendicular magnetic field was found to greatly increase pumping accuracy, as first reported by Wright [30] and developed by others [28, 31, 32]. The potential profile shape of the loading stage of $V_{G1}^{AC}$ (case A in Fig. 1.3(b)) can change the pumping accuracy, by slowly loading the electrons and suppressing backtunneling, as found by Giblin [16] and others [33–35]. Temperature and QD geometry are likely important factors too. Verification of equivalent methods in other materials [13, 36–40] which exploit much of the same physics, demonstrates material independence as we would expect for a system almost entirely dominated by the gate electrostatics. Further verification arises in the observation of excited states [32], which degrade the pumping plateau. Electrons excited above the ground state during loading of the QD (case A) have an increased likelihood of backtunneling, reducing the pumped current from the expected value. This additional backtunneling is found to occur at well defined energies, described by the Fock-Darwin spectrum [24] of single particle states, which follows from the CI model in a perpendicular magnetic field. One way of this occurring is by increasing the frequency such that the relaxation time to the ground state in the dot is slower than the rate of change of the levels.

It is worth noting that accuracy measurements have had to develop to allow the electron pump accuracy to be established, driven by metrological motivations [41–43], which propose

the electron pump to define the Ampere by pumping a fixed number of charges per second. Error detection mechanisms have helped complete the empirical picture described above [44–46]. (By errors we mean "pump two electrons on the first plateau" or "pump no electrons on the first plateau" per cycle).

The accuracy, its dependencies and material independence demonstrate nicely that the CI model is broadly correct in our need only to consider the electrostatics, although it does not handle time dependence. A dynamic theory was proposed by Kaestner [47, 48] and fully developed by Kashcheyevs [49], now known as the "decay cascade" model, which extends the CI model. This is the explicit description of the electron pump that underpins our understanding of the pump cycle.

The decay cascade model is based on the balance of forward vs back tunneling probabilities at any given time in the pump cycle. For most accurate pumping, we require an adiabatic (Markovian) process; that is, the loading and pumping are decoupled by a stable QD. For this, electron relaxation time must be less then the rate of change of the QD levels, so that deexcitation to the QD ground state is favourable over back tunneling. Formally, this is done by writing down the rate of change of QD population as a function of the rate of forward and backtunneling (a rate equation), evaluated over a time interval in which the dot levels, and so the electron relaxation time, change as a function of time. This yields the pumped current as $I_p = ef\langle n\rangle = ef\sum_n nP_n$ for $n$ electrons occupying the QD with probability $P_n$ and $\Gamma_n$ the tunneling rate out of the QD at an occupation of $n$ electrons. Numerical evaluation of $P_n$ gives $P_n \propto exp(-\int_t \Gamma_n) \times exp(-\int_t \Gamma_{n+1})$, which gives the double exponential staircase plot of Fig. 1.3(c).

For this work, we are not so concerned about accuracy, as our measurements are long averages and so we are quite insensitive to pump errors. Our measurement system has only $\sim 0.5$pA resolution, which is $\sim 1\%$ of the pumped current. We take it as established that the electron pump in this form, utilising this physics, has accuracy to at least ppm level if not better, and whilst proving and improving accuracy is a hot topic for the community, it

will not feature in this work. Practically, observation of current quantisation (flat to within our resolution) and a pump map visibly similar to those obtained in the literature [16] are sufficient for us to work with. No quantitative analysis was performed on the accuracy of the pumps used in this work.

## 1.5 Experimental Setup

We have established the fabrication of the electron pump and its method of operation. Now I detail the experimental setup with which we measure the devices. This is mostly consistent throughout the rest of the chapters, unless otherwise stated.

Devices are very sensitive to electrostatic discharge (ESD), which means they can be "spiked" (change of channel conductance) or blown up (gate metal ripped off surface) by discharge of voltage from floating gates or introduction of floating metal to the system. This is quite a common problem. With this in mind, we take care to make sure all connections are grounded when introducing them to the sample, and the sample is handled with all gates and ohmic contacts grounded. Samples are prescreened in a 4 K dipping dewar to test operation, as a fast way to establish if the device is working. Fig. 1.4 details the experimental setup.

### 1.5.1 The Experimental Setup

For this work, two cryostats were used - a sorption pumped 3-He system (chapters 2-3), with base temperature $\sim$ 300mK, and a dilution refrigerator (chapters 4-6) with base temperature $\sim$ 28mK. The connections made to the sample in each case are nearly the same.

We now describe the setup with reference to the letters in red on Fig. 1.4. We use a Uninterruptible power supply (UPS) to provide isolation against mains noise and voltage spikes (we utilise its switched mode power supply rather than its battery) [A]. An isolation transformer [B] isolates the rack from mains noise. Additionally the ground is broken here - downstream of the transformer we use a dedicated scientific ground [C], which is a separate

ground rod only for the two cryostats. To keep the grounds separate, communications from the PC to instruments are via optical lines [D]. Within the rack, communication is via GPIB or ethernet (green). DC gate voltages are provided by Keithley 213 DACs [E], which have their output filtered against voltage spikes. AC voltages are provided by an Arbitrary Waveform Generator (AWG) [F] (either a Tektronix 7122C or 70K series). The pump drive, $V_{G1}^{AC}$, is filtered by a LP 630 MHz or 6 GHz filter. [G] highlights the efforts made to reduce voltage noise that would otherwise reduce our voltage resolution. We use room temperature filtering, cryogenic filtering, AC chokes, DC blocks and AC attenuation, to reduce noise from ground loops or ambient pick up loops and prevent transmission of voltage spikes to the device. For RF gates, a DC offset is also added via a bias tee (room temperature on cryostat, MC temperature on fridge). Attenuation in the lines is approximately 8 dB fridge/3 dB cryostat. The sample [I] is shown schematically. We show two gates, one DC and one RF, for simplicity. Ohmic contacts (crossed boxes) provide the measurement line. Unused ohmics are grounded at the breakout box. Measurement lines are passed through Femto DDPCA-300 or DLPCA-200 variable gain amplifiers (we normally use $10^{10}$ V/A). HP34401A electrometers are used to measure the amplifier voltage readout.

The reader should be convinced by the extra effort to remove voltage spikes that ESD protection is our major concern. When connecting the sample, we use extra grounding straps to ensure all connecting lines are grounded.We also aim to reduce noise, with the inductive chokes and careful grounding to avoid ground loops. All of this gives us typically no more than $1-2$ pA peak-to-peak current noise. Some 50 Hz powerline pickup is still frustratingly visible in the data, however. Fig. 1.4(b) shows some photographs of the experimental setup to complement the schematic of (a). We now have an electron pump and setup to measure it in. Next we move on to the first experiment, pumped electron detection.

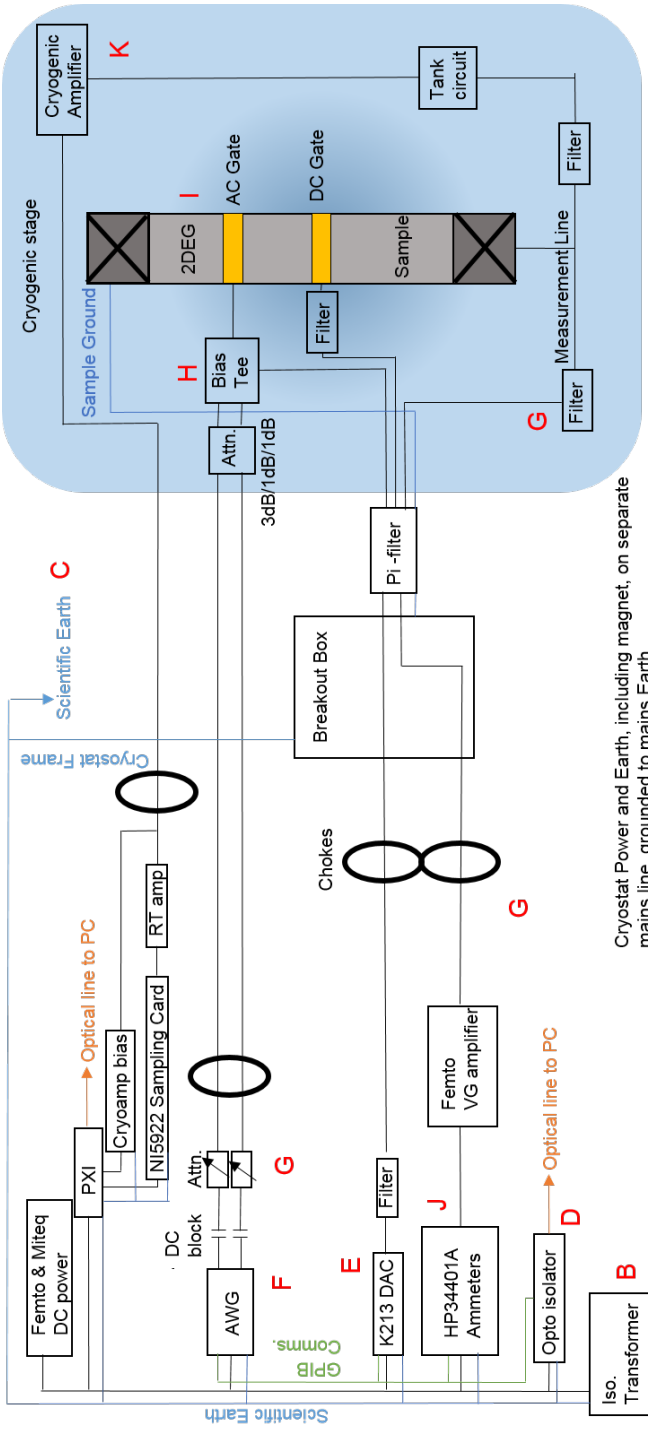


Figure 1.4: (a) Schematic of the experimental setup used throughout this work. Power and measurement lines are shown in black, grounding lines in blue and communications in green/orange. Area shaded in blue is within the cryostat. Labels in red highlight points discussed in the text.

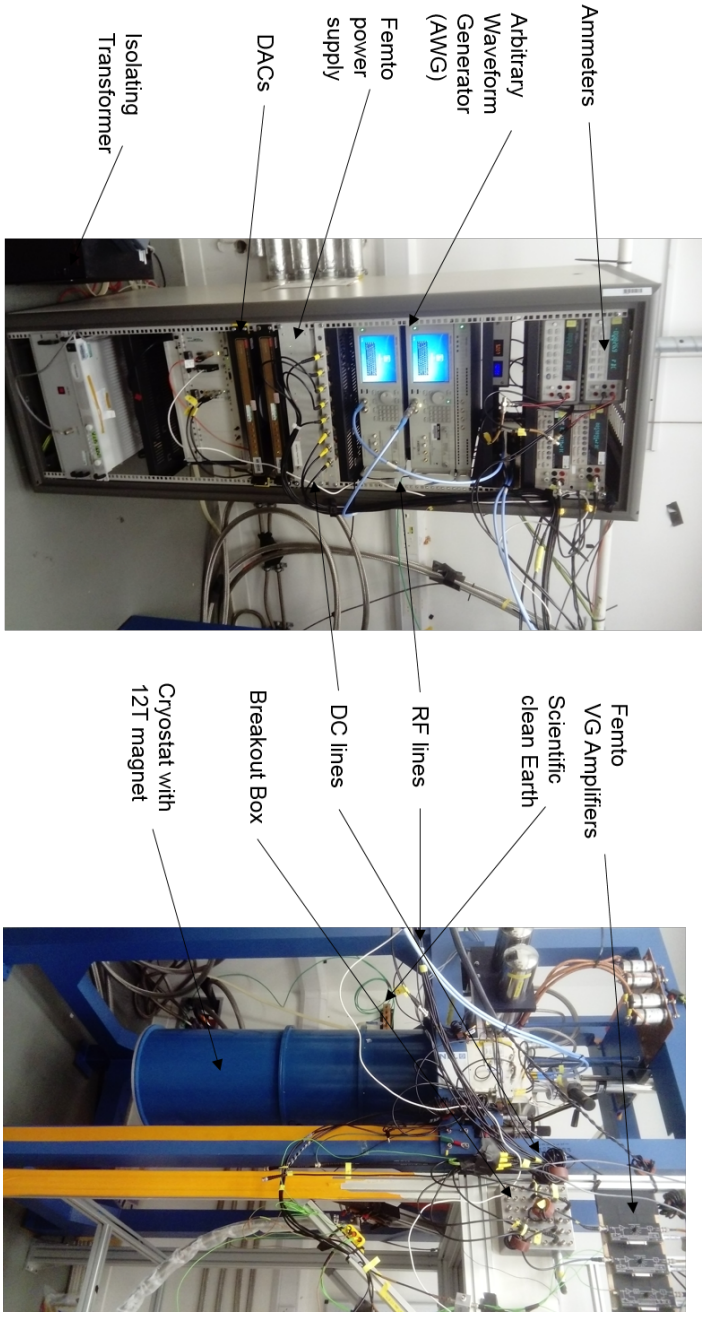


Figure 1.4: (b) The experimental setup shown on the dilution refrigerator, with key features labeled.

# Chapter 2

# Electron Detection

## 2.0 Introduction

In the previous chapter we described our source of single electrons, the NPL electron pump. We are now in a position whereby we have an accurate electron pump that produces individual electron wavepackets. What we can do with these wavepackets is the subject of the body of this thesis. We begin with the technique at the heart of all the experiments described in this work: the detector barrier. I will begin by introducing hot electron transport, the method by which our pumped electrons propagate across the device. Then, I will review the previous work on electron detection by use of a detector barrier, which established energy and temporal resolution of the pumped electrons. We will then move on to my own contribution, which furthers the development of the temporal bandwidth of the detector. As I will describe, I undertook a series of experiments to quantify and improve temporal resolution of the detector barrier, which ultimately culminated in a publication for Applied Physics Letters (APL), which we believe is the current state of the art for electron detection in the hot GaAs/AlGaAs 2DEG system.

Associated publication: **Ultrafast Voltage Sampling using Single-electron Wavepackets**

N. Johnson, J. D. Fletcher, D.A. Humphreys, P. See, J.P. Griffiths, G.A.C. Jones, I. Farrer, D.A. Ritchie, M. Pepper, T.J.B.M Janssen, and M. Kataoka

Appl. Phys. Lett. 110 102105 2017

goo.gl/FV47Om

*Author Contributions: N.J. Performed the measurements, analysis and wrote the paper, with support from M.K; P.S. performed the fabrication with assistance from J.P.G, G.A.C.J, I.F, D.A.R; D.A.H, J.D.F, T.J.B.M.J, M.P. provided supervision.*

## 2.1 Hot electron propagation in GaAs

As established, the electron pump is a source of single electron wavepackets, that are typically pumped (i.e. tunnel over the "exit" barrier $G_2$) $\sim 100$ meV above the Fermi Energy $E_F$ [8]. Our concern now turns to what happens to these wavepackets afterwards, on leaving the quantum dot that defines the pump. We consider only the case of a magnetic field applied perpendicular to the plane of the 2DEG in the $\boldsymbol{E} \times \boldsymbol{B}$ drift regime (strongly confined, we justify this in the next chapter). In this regime, we can expect to see transport at the Fermi energy governed by the Quantum Hall Effect (QHE) (indeed the fractional effect, with carrier concentrations between 1.6-2.1 $\times 10^{11}\text{cm}^{-2}$ giving $\nu \sim 0.6 - 0.8$). However, we note our pumped electron is at a much higher energy than the Fermi energy and so we can make some simple assertions to derive propagation without a full treatment of the quantum Hall effect. Halperin [50] proposed the existence of current carrying edge states at high energy. These states arise from the Landau Levels branching towards $V = \infty$ at the sample edge.

### 2.1.1 Landau Levels

For a magnetic field perpendicular to the 2DEG ($\boldsymbol{B} = B_z > 0$) an electron residing in the 2DEG has a Hamiltonian of the form

$$H = \frac{1}{2m^*} \left(\boldsymbol{p} + e\boldsymbol{A}\right)^2 \tag{2.1}$$

with $m^*$ the reduced mass ($0.067m_e$ in GaAs), $\boldsymbol{p}$ the canonical momentum ($= -i\hbar\nabla$), $e$ the electron charge, and $\boldsymbol{A}$ the vector potential ($\boldsymbol{B}_z = \nabla \times \boldsymbol{A}$). Because $\boldsymbol{B}$ has a simple form, $H$ can be taken as a harmonic oscillator, because $\boldsymbol{p}^2, \boldsymbol{A}^2 \propto x^2, y^2$ for $x, y$ describing the plane of the 2DEG, and is hence soluble (the electron propagates away from the pump in $x$). The (time-independent) Schrödinger equation is $H\psi = E\psi$ with eigenenergies $E$. We can make use of the gauge used in Jain [51] to solve for $E$. We get the familiar quantum harmonic oscillator energy levels [52, 53]

$$E_n = \left(n + \frac{1}{2}\right) \hbar\omega_c \tag{2.2}$$

with $\omega_c = \frac{|e|B}{m^*}$ the cyclotron frequency. The label $n$ is denoted the Landau Level Index. An important consequence, noted by Halperin [50], was that each of these levels has a spatial dependence [53].

Away from the edges of the 2DEG, i.e. where the electron wavefunction has minimal overlap with the physical edge, we have the ladder of equally spaced states given by the above expression. The overlap is defined by $|\psi|^2$, which is symmetric about the charge centre and negligible for distance greater than the cyclotron radius $r_c = \frac{\sqrt{2m^*E}}{eB}$. Halperin's insight arises from the need for the electron wavefunction to be completely constrained to the 2DEG, i.e. the physical edge of the sample represents a totally forbidden region. Simplifying his derivation to an electron propagating in a channel in $x$ with transverse position $r_m$ and with a sample boundary running parallel a distance $r_3$ away, we deduce the spatial dependence

of the wavefunction $\psi$ as

$$\psi_m n(r) = const. \times \exp(imz) g_n(r - r_m) \tag{2.3}$$

with $\psi_r$ the 1D wavefunction perpendicular to the travel direction and $m$ the magnetic quantum number. $r_m$ is the length scale such that

$$B\pi r_m^2 = m\Phi_0 - \Phi \tag{2.4}$$

with $B$ the field perpendicular to the 2DEG plane, $\Phi$ the magnetic flux and $\Phi_0$ the flux quantum. If we examine our eigenvalues $E_n = \left(n + \frac{1}{2}\right)\hbar\omega_c$ with this spatial dependence, we find that if our electron is centered far from the edge, so $r_3 - r_m >> r_c$ (i.e. no overlap with the edge), then we recover the ladder derived above. As our electron approaches the edge, we define a point $r_2$ where $r_m = r_2$ where our eigenvalue is $E_n = \hbar\omega_c\left(2n + \frac{3}{2}\right)$, and as the electron gets closer $E \longrightarrow \infty$ as $(r_m - r_2)^2 e^2 B^2/2m^*$ for $r_2 - r_m < r_c$. We plot this curvature in Fig. 2.1, taken from Halperin [50]. In this plot, he shows the symmetry across the channel by including an opposite edge and equivalent point $r_1$. Our channels are usually many microns wide, narrowing only where gates span the channel, so we do not consider the other edge as it is so far away.

In our case, the pumped electron propagates above the Fermi Energy, and so is confined to the edge of the sample, where the current carrying states bend upwards. There is no evidence of any levels $n > 0$ occupied by pumped electrons (see next chapter).

### 2.1.2 Ballistic Transport

Observation of Ballistic transport has been observed by many [11, 54–58], with Chklovskii deriving the theory [59]. It is found that the electron propagates individually in an edge state without loss until a scattering event occurs, with little to no impurity scattering. At the Fermi energy, scattering events are dominated by electron - electron interactions [59].

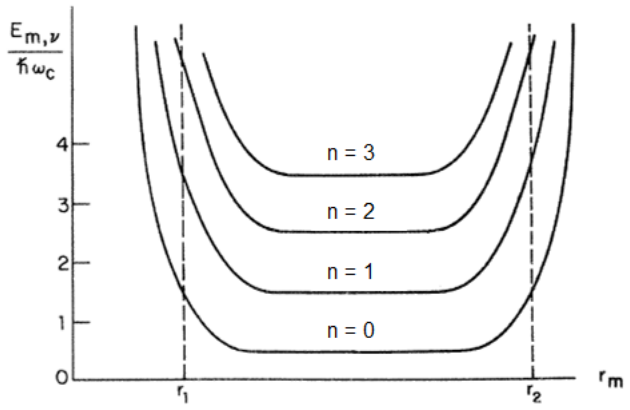


Figure 2.1: Sketch of Halperin's derivation of edge state transport, adapted from Halperin [50]. Here, $r_m$ is a distance coordinate transverse to the electron propagation direction. Where there is no overlap of the wavefunction with the physical edge of the heterostructure, the familiar ladder of equally separated states is found. Where there is overlap, the states bend upward towards infinite potential, approximately parabolically.

For us at high energy, our pumped electron is well separated from the 2DEG in energy, suppressing interaction, and may also be physically further away too. Even for energies only slightly above the Fermi Energy, electron-electron scattering is greatly suppressed [55]. We explore the nature of scattering and edge state transport for our regime fully in Chapter 4. As we measure in Chap. 4, the main scattering mechanism at this energy is the LO phonon.

Within this ballistic regime, electrons are expected to behave semi-classically, obeying $\boldsymbol{E} \times \boldsymbol{B}$ drift, i.e. there is drift of a guiding centre about which the electron gyrates with frequency $\omega_c$ and radius $r_c$. This confines transport to the edge of the sample, as complete loops form locked orbits [60], but at the edge the electron must scatter from the forbidden region, giving spatial dependence. Our measurements of Chap. 4 provide some support of this view.

## 2.2 Electron Detection

We have established the mode of propagation across the device as edge states, analogous to quantum Hall edge states, as physical edge confined ballistic transport. We can use e-

beam etching to define a geometry of interest, and hence create a waveguide for the pumped electrons. The two most common techniques for charge detection in a two dimensional electron system are the Quantum Point Contact (QPC) [45] and the Single Electron Transistor (SET) [61]. These have been shown to be very successful. Here, we present a slightly different method of electron detection, that can provide better energy and temporal resolution, although it does not have the single shot capability of the QPC or SET (yet, but it should be possible). In a more general approach, schemes have been proposed that have utilised electrons traveling in 2DEGs or in QDs for quantum information processing [62–64], and perhaps there is some translational ability to construct such systems with our detector. The electron detector as presented here can help as a charge read out system, which can be potentially used for these quantum information technologies. In this chapter, we develop the properties of the electron detector and show it can be used for single - electron electronics.

Our detector barrier is simply an e-beam lithography defined AuTi gate spanning the surface of the 2DEG channel, exactly as we use for the pump gates $G_1$ and $G_2$. When a negative voltage is applied to it, it forms a potential barrier in an analogous way to a Schottky barrier. By tuning this potential to match the pumped electron energy we develop energy and temporal resolution. We will now discuss this fully and determine the resolution of this method.

## 2.3 Energy Resolution

Palevski [11] and later Taubert [57] had already utilised a single gate as a barrier, with which to selectively permit electron transmission based on energy, to understand hot electron relaxation. This works by assuming a classical transmission across the barrier for nearly all energies, with wavepacket splitting being possible only in a very small range of voltage. That way, finding the highest potential at which hot electrons would still be able to make it across the barrier (i.e. be transmitted) is a direct measure of their energy. The NPL group under

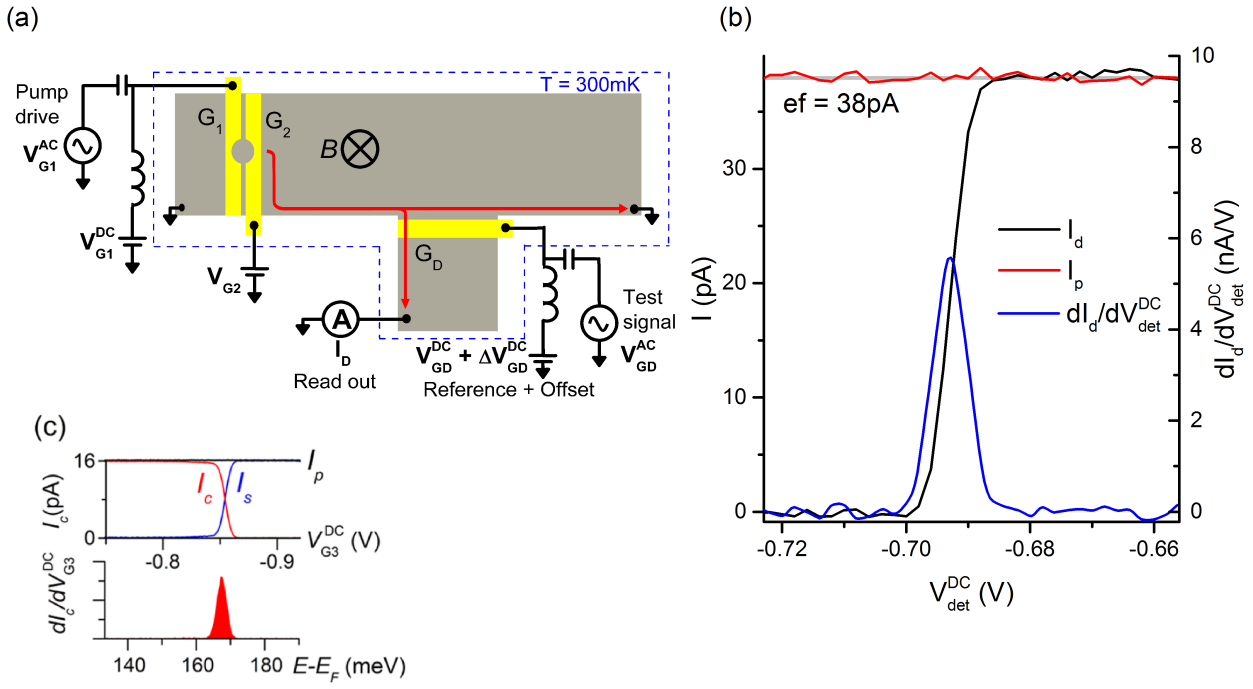


Figure 2.2: (a) Sketch of the simplest device geometry, with pump defined by gates $G_1$ and $G_2$ and detector $G_D$, with electrical schematic, adapted from Johnson [65]. (b) The pump produces a current of $I_p = 38$ pA, and the transmitted current across the detector $I_d$ is seen to vary from 0 to $ef = I_p$. The derivative $dI_d/dV_{det}^{DC}$ gives the profile of transmission from T = 0 to 1. (c) Figure from Ref. [8] showing the first realisation of the detector output.

Fletcher et al. [8] utilised this idea of a energy selective barrier to study the output of the single electron pump. Transmission across the barrier is only permitted when the electron energy is greater than the potential on the detector barrier, with a small transition region of $< 10$ meV in which the current is split. Adding the currents in the reflected and transmitted channels is found to equal the total pumped current, in agreement with Kirchoff's current law. By using a source drain bias, the absolute potential on the detector barrier can be calibrated. Fig. 2.2 demonstrates the concept.

In Fig. 2.2(a), electrons propagate in edge states (red) from pump across the device, impacting upon the detector barrier $G_D$ with potential $V_{det}^{DC}$. If the electron energy is greater than this potential, the electron can tunnel across the barrier, passing underneath the gate towards the lower ohmic contact. Otherwise, it is deflected to the right hand side terminal. An ammeter connected to the far side contact, as marked in the figure, will only record a

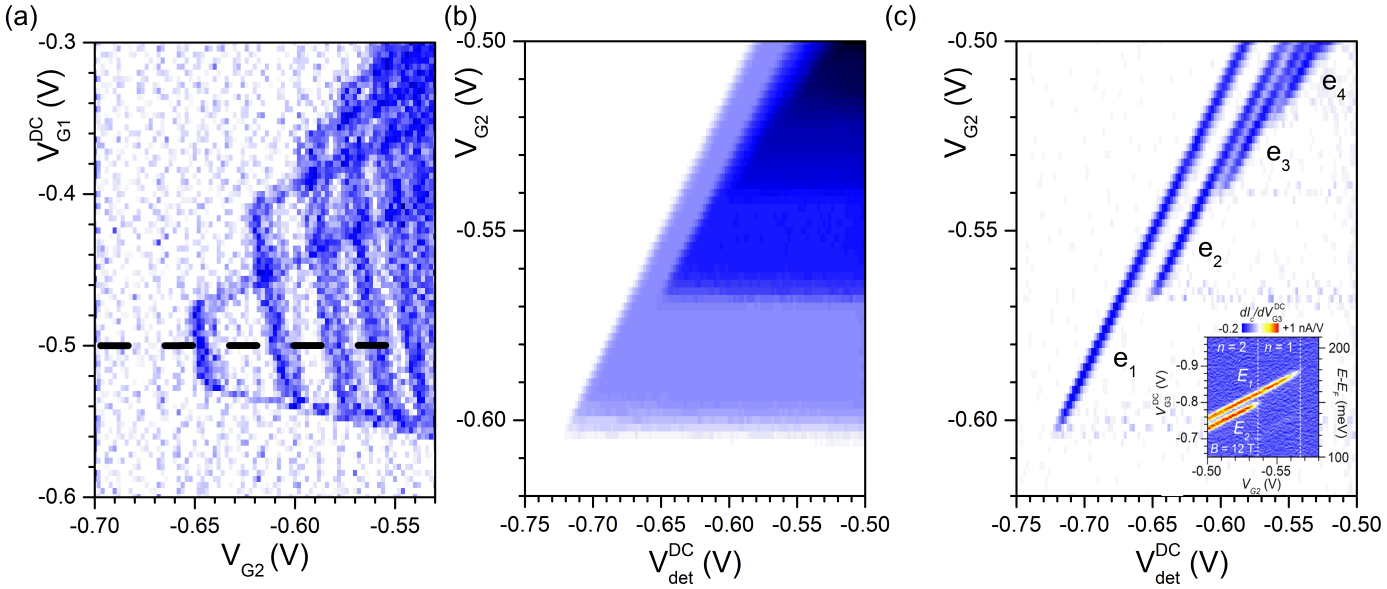


Figure 2.3: (a) Pump quantisation map, equivalent to Fig. 1.3(d), with dashed line showing line of measurement in (b). (b) A typical "detector" map, spanning the voltage space of the detector $V_{det}^{DC}$ (horizontal axis), providing energy resolution, and the pump exit barrier $V_{G2}$ (vertical axis), setting the pumping energy. We see a linear relationship between the gate voltages and the electron energy. (c) Horizontal derivative of (b), $dI_d/dV_{det}^{DC}$. This shows more clearly the onset of current across the detector. Each pumped electron per cycle possesses the same linear relationship, offset in energy. Each contribution is labelled $e_{1-4}$. Inset: An equivalent map taken from [8], the first published example of this plot.

non-zero current when the detector barrier has a transmission $T > 0$. Hence, we can develop energy resolution by tracking the onset of non-zero current.

At this point it should be remarked that such a method relies on a large number of electrons interacting with the detector (sequentially). In principle, however, the detector barrier could be coupled with a QPC or SET to sense transmission of a single electron across the detector barrier, although we have not constructed such a system [61, 66]. However, we normally pump with frequency 120-240 MHz at 1 NPLC measurement so many electrons sample a data point. This can be improved and can be made to be a faster measurement.

In Fig. 2.2(b) we plot a current trace across the detector opening point. The pump is producing a constant output current of $I_p = ef = 38$ pA, as shown by the red trace. The ammeter on the detector far side contact records the transmitted current $I_d$ in the black trace. This is seen to vary from 0 to $ef$ as the barrier opens up, over a range of $\sim 10$ mV. This range

defines the partial transmission $0 < T < 1$. We also plot the derivative $dI_d/dV_{det}^{DC}$, which gives the energy distribution across the barrier, and more clearly shows us the arrival energy of the electron wavepacket. In Fig. 2.2(c) we plot the equivalent figure from Ref. [8], the first published example of this plot, for comparison. Correspondingly, the reflected current $I_S$ is seen to vary from $ef$ to 0 over the same voltage range (red). This is of course as we expect, satisfying Kirchoff's current laws and the normalisation $T + R = 1$; $I_C + I_S = I_P (= ef)$.

A perfect detector barrier [1] (that is, one with a transmission $T = \Theta(E - E_c)$, with $\Theta$ the Heaviside step function and $E_c$ the distribution centre) will satisfy

$$\frac{dI_d}{dE} = \frac{d}{dE}\Theta(E - E_c) = \delta(E - E_c). \tag{2.5}$$

We note that in the limit of a finite rise time of the detector barrier, a representation of $\Theta(E - E_c)$ is the error function

$$\Theta(E - E_c) = \frac{1}{2}\lim_{\epsilon \to 0} \operatorname{erfc}\left(-\frac{E}{\epsilon}\right) \tag{2.6}$$

for small broadening $\epsilon$. Hence the energy distribution is

$$\frac{d}{dE}\left(\frac{1}{2}\operatorname{erfc}\left(-\frac{E}{\epsilon}\right)\right) = -\frac{1}{\sqrt{\pi}}\exp\left(-\left(\frac{E}{\epsilon}\right)^2\right) \tag{2.7}$$

which is a normal distribution [2].

In Fig. 2.3(a) we show the pump quantisation map, and in Fig. 2.3(b), we create a 2D map of transmitted current $I_d$ as a function of electron energy at the point on the quantisation map marked by the line. On the horizontal axis we plot the detector barrier voltage $V_{det}^{DC}$, and on the vertical the pump exit barrier voltage $V_{G2}$, which is proportional to the pumped electron energy. We see a linear relation between pumped energy and $V_{G2}$, and in the regime

[1] In the limit that the electron possesses no energy spread, which we will discuss further in Chap. 5.

[2] The reverse case is more intuitive, that is $\lim_{\sigma \to 0} G(E) = \delta(E)$ for a Gaussian $G$, and is an elegant verification of transmission across a classical barrier.

where the detector is fully open (lower $\left|V_{det}^{DC}\right|$) the ammeter records the pump output, with the familiar $I = nef$ plateaus visible from $n = 1$ to 3. In Fig. 2.3(c) we take the horizontal derivative $dI_d/dV_{det}^{DC}$ of the same data. This better shows the onset of transmission across the detector, and hence from now on we shall mainly use derivative maps. In a perfect Schottky barrier, the point of maximum derivative would be equivalent to half transmission across the barrier. This may not be so if it has more complicated pinch-off characteristics. This is not so important however; our requirement only being to track some known transmission, not necessarily $T = \frac{1}{2}$. In all samples used in this work, the point of maximum derivative was found to correspond to the half transmission point to within our 1-2 mV resolution, and henceforth we take the point of maximum derivative as our pumped energy.

As an example, we typically see (for this design of electron pump, driven by a sinusoidal waveform $V_{G1}^{AC}$), that when pumping two electrons per cycle ($I_p = 2ef$) that the electrons are energy separated. It is not possible to derive this result from current measurements alone, but our detector easily distinguishes each contribution. This shows up as two clear lines in the derivative (labelled $e_1$, $e_2$ on Fig. 2.3(c), up to the fourth electron $e_4$). In the inset to Fig. 2.3(c) we compare our measurement with [8], the first published result of this map, and find excellent agreement.

Resolution is, in theory limited only by the DC voltage source capability. In practice, we are handicapped mostly by crosstalk from the pump drive $V_{G1}^{AC}$, and the current noise measured by the ammeter, which is typically 1-2 pA. This gives a voltage resolution of $\sim 2\text{mV} \approx 1\text{meV}$ (there is some sample-to-sample variation with this).

## 2.4 Temporal Resolution

Fletcher [8] also went on to add a small AC oscillation to the detector barrier and showed that when the form of this oscillation is a sine wave, the transmission across the detector tracks the form of the wave. This shows that the electron wavepacket profile in time is small

compared to the rate of change of the AC oscillation. This was extended and formalised by Waldie [67] and then myself [65].

To develop temporal resolution, we add a small oscillation to the detector barrier, $V_{det}^{AC}$, in addition to the DC potential $V_{det}^{DC}$. The transmission is modified accordingly as shown schematically in Fig. 2.4. We plot the time delay between $V_{G1}^{AC}$ and $V_{det}^{AC}$, $t_d$ (horizontal axis) against our energy $V_{det}^{DC}$ (vertical axis). In (a), $V_{det}^{AC} = 0$, so detector barrier transmission is not a function of time, and the barrier half transmission point is at a single $V_{det}^{DC}$ value, but in (b), when $V_{det}^{AC} \neq 0$, the barrier half transmission point is modified according to the amplitude of $V_{det}^{AC}$.

We utilise the fact that the electron wavepacket is small in the temporal and energy domains (just how small is the subject of chapter 5). The size of the wavepacket in the temporal domain determines how long the electron interacts with the detector barrier. Transmission is determined by the instantaneous barrier potential $V_{det} = V_{det}^{DC} + V_{det}^{AC}$ ($V_{det}^{AC}$ is assumed quasistatic over this short interaction time). In Fig. 2.4(b), we see how transmission is modified as a function of time $t_d$. In the left panel is our previous case of $V_{det} = V_{det}^{DC}$. Here there is no time dependence and we trivially record a horizontal trace in a current transmission map as a function of time. When we introduce an AC signal, so $V_{det} = V_{det}^{DC} + V_{det}^{AC}$ ($V_{det}^{AC} \neq 0$), transmission is modified according to when the electron arrives at the detector, as seen in (b). The derivative of current $dI_d/dV_{det}^{DC}$ still tracks the (nominally) $T = 1/2$ point. We will formalise this argument in the next section.

We would expect each electron to be pumped from the same part of the pump drive waveform $V_{G1}^{AC}$ for each cycle of RF. Hence, if we are to construct a map of the form of Fig. 2.4(b) we have to shift the phase of $V_{det}^{AC}$ with respect to $V_{G1}^{AC}$, and it is this relative shift we plot as $t_d$. Practically we have always implemented this by using the Arbitrary Waveform Generator AWG (Tektronix 7122C) with two outputs, one for each AC signal, and shifted them with respect to one another using the inbuilt skew (hardware) control. Other methods are possible, such as using a delay line.

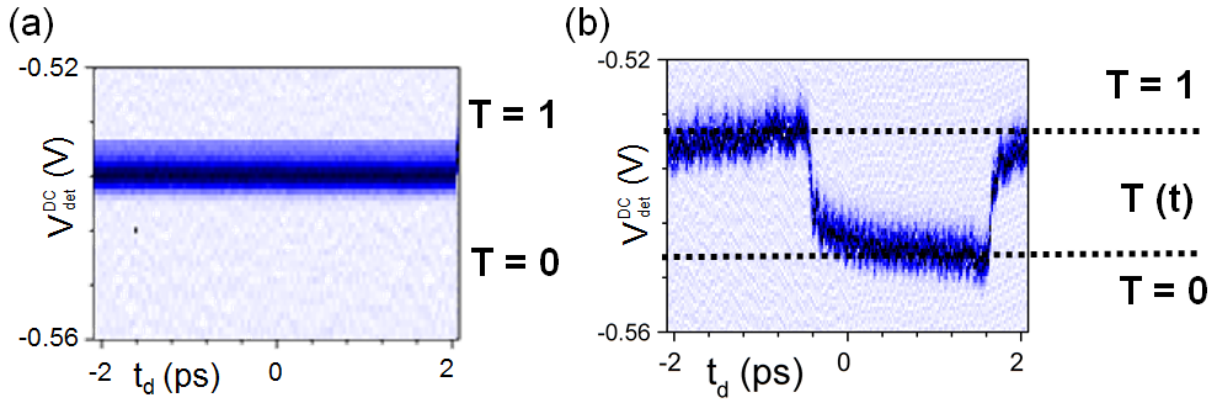


Figure 2.4: Temporal resolution of the detector. The time delay $t_d$, equivalent to the temporal axis, is plotted against the detector barrier energy axis. (a) In the DC case, $V_{det}^{AC} = 0$, there is no time dependence in the detector barrier transmission, so the transmission point is unchanging in time. The two regimes of transmission ($T$) are marked. (b) In the AC case, $V_{det}^{AC} \neq 0$, transmission across the detector is seen to vary as a function of time, introducing a third transmission regime $T(t)$.

To continue our example from the previous section, when pumping two electrons per cycle with a sine wave drive, not only are they energy split, but they are also temporally split, as shown in Fig. 2.5. This plot again tracks the isoline of energy in time, but at each electron's distinct energy. Such observations were developed by Fletcher [8] and Waldie [67] to develop an understanding and control of the pump cycle. Observations such as those shown here elegantly verify the CI/decay cascade models in the pump's QD: electrons sit at different levels in the QD (the field leaves no degeneracy), and each has a different coupling to the drain lead, causing tunneling at different times. The QD levels are dynamic, being driven by $V_{G1}^{AC}$, and so the electron energy changes during the time between the first and second electron leaving. After one electron leaves the QD, the chemical potential of the dot $\mu$ decreases by the addition energy. This will decrease the tunneling probability for the remaining electron, and we wait for the driving waveform to elevate the potential sufficiently for tunneling to occur. Effectively, the last electron to be pumped from the QD is always from a "one-electron" QD, and that is why the emission line (see Fig. 2.3(c), i.e. the point at which the detector barrier opens up is the electron emission energy) is continuous across the

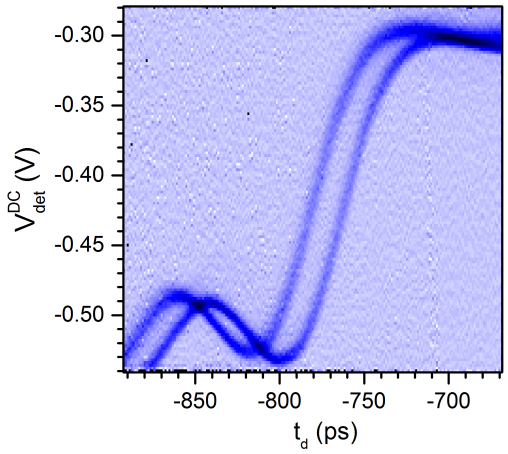


Figure 2.5: Pumping two electrons per cycle will result in the electrons having non-simultaneous arrival in the detector.

plateaus. The same argument can be extended to the second electron emission line onto the third plateau, etc. In this simple argument, we have assumed that the electron relaxation time is far shorter than the period of the driving waveform ($V_{G1}^{AC}$) such that the driving waveform is quasistatic over the relaxation time. However, this condition was relaxed in work by Ryu [68] without qualitative detriment to the argument.

## 2.5 A Single Electron Oscilloscope

Now we discuss my own contributions to the development of the detector barrier. I largely extend the preceding discussion and results. In doing so, we effectively create a "single-electron oscilloscope". This is a formalised sampling scheme as we discuss here. I showed that such a scope has high bandwidth (up to 100 GHz) and high fidelity. This has many potential applications. The nature of the small energy scales in quantum physics means many interesting effects are destroyed by high temperature. For the foreseeable future, such experiments are confined to the cryogenic realm. Applications of such effects, such as some quantum information processing protocols [63, 69–71] are also limited to cryogenic working. High frequency signals are needed in such schemes to establish and implement specified states. While there exists commercially available sampling oscilloscopes to measure such

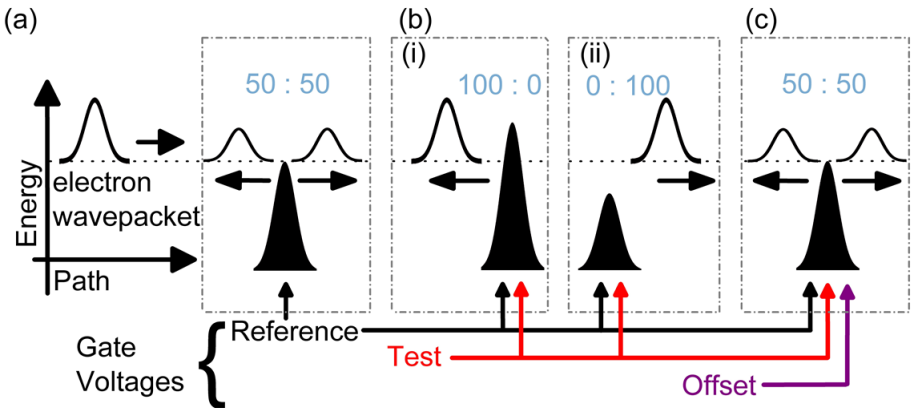


Figure 2.6: The single electron sampling (SES) scheme. (a) The electron pump produces a single electron wavepacket which propagates toward the detector barrier. (b) We tune the detector barrier such that $V_{det}^{DC}$ gives half transmission. We denote this voltage our "Reference". (b) When an unknown periodic "Test" signal $V_{det}^{AC}$ is added, transmission across the detector is modified according to case (i) or (ii). (c) We adjust $V_{det}^{DC}$ to bring the barrier back to half transmission by addition of an "Offset". The Offset has equal amplitude but opposite sign to the unknown test signal. Taken from Johnson [65].

high frequency pulses (up to 100 GHz [72–74]), there is a difficult barrier to overcome in the long measurement lines and many joints involved in connecting to a cryogenic sample. The losses from these lines limits the measurable bandwidth significantly. Our proposal is for a cryogenic analogue of the sampling oscilloscope, whereby the signal under test propagates onto the detector barrier, and pumped single electrons establish its form by transmission as a function of time delay between the pumped electron and test waveform phase.

We define our formal scheme the "Single Electron Sampling (SES)" scheme and it is illustrated in Fig. 2.6. In this scheme, we define the detector gate voltage as consisting of three components. First, we establish the DC opening point of the barrier, when $V_{det}^{AC} = 0$. This is equivalent to the energy resolution scheme above. We define the voltage at which we see half transmission (really the maximum derivative) the "Reference". When we introduce an unknown AC "Test" signal (the only requirement is that it is periodic) $\left|V_{det}^{AC}\right| > 0$, transmission across the detector is modified as Fig. 2.6 (b)(i) or (ii), depending on the sign of the signal. We then introduce another DC component to the barrier, known as the "Offset". This is the voltage required to bring the detector back to half transmission, and is

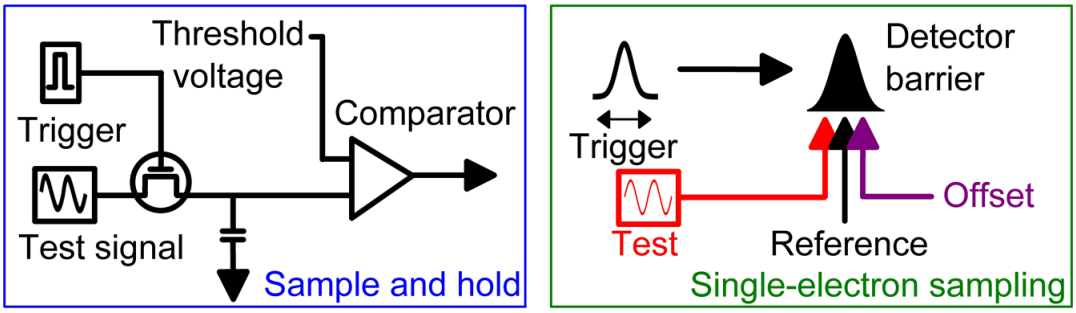


Figure 2.7: Comparison of a commercial sampling oscilloscope sampling technique (left panel) with the SES scheme (right panel). Taken from Johnson [65].

therefore the amplitude of the unknown AC signal (with the opposite sign).

The analogy with commercial room temperature sampling oscilloscopes is illustrated in Fig. 2.7. These scopes are based around the use of a sampling gate using the sample-and-hold technique [75]. A semiconductor switch is triggered with a picosecond pulse that allows it to open. The input signal is then transmitted onto a capacitor, charging it. The switch is closed, and the capacitor slowly discharges the input voltage into a comparator, which compares the input voltage to a known reference. High bandwidth is achieved by making the switch pulse as short and sharp as possible, sampling, or constructing sampling circuits in parallel. Parasitic loss in this trigger pulse, as well as of the input across the switch itself, limit the bandwidth [75].

In the left panel, we show a simplified schematic of a sample and hold scheme implemented in a commercial scope [72, 76]. In the right panel, we draw analogies to our detector barrier method. In our detector system, the trigger pulse is represented by the pumped electron wavepacket. This samples the instantaneous potential on the detector (see arguments above). The transmission of the wavepacket across the detector barrier is a binary output, just as is the scope's comparator circuit, depending on the reference voltage, equivalent to the threshold voltage in the comparator.

We proceed to demonstrate first the accuracy of the SES method. The result of applying our SES method is shown in Fig. 2.8(a). We obtain a current map, with transmission as a function of delay. The point of half transmission tracks the shape of the waveform. Here,

the test waveform is a sine wave. We extract the point of maximum derivative in (b) (black), and fit it to a sine curve (red). The inset to this is the residual of the data and the fit. We see that it is on average zero, indicating high fidelity. Our voltage replication is accurate to within the linearity of our source, a Keithley 213 which should be accurate to 250 $\mu$V. Fig. 2.8(c) shows some examples of the SES scheme with different test waveforms, showing the wide variety of signals we can sample.

To more quantitatively develop our temporal resolution, we consider Fig. 2.8(d). We take a sine wave construction (i) as our Test signal and measure it as per the SES scheme, obtaining the current map (ii). We extract the point of maximum derivative by performing a Gaussian peak fit to the (vertical) derivative $dI_d/dV_{det}^{DC}$, which we plot in Fig. 2.8(d)(iii) in black. This waveform contains higher harmonics, that are artefacts of the 6 GHz AWG sampling rate (in Fig. 2.8(a) we have used a 630 MHz LP filter to remove this contribution). We include them here as resolution of this feature implies high temporal resolution. On the same plot, in red, we plot the same waveform as measured by a commercial Tektronix MSO72304DX sampling oscilloscope (scaled by factor 2, owing to the scope having 50 $\Omega$ input termination vs. the open ended sample). For this, we remove the measurement probe from the cryostat, and simply connect a 1 m coax line to where we would connect the sample holder, which feeds in to the scope. Differences in transmission due to temperature and shielding should be negligible, although we note that the different input termination could have a small effect. Qualitatively, the traces look similar. We repeat this analysis in Fig. 2.8(f) with the case of a square wave as the Test waveform, finding again a strong similarity in the measured waveforms.

To be quantitative, we choose the highest frequency waveform we can generate with our AWG (Tektronix 7122C), which is a 2-point construction run at the maximum sampling rate of 12 GS/s (6 GHz), shown in Fig. 2.9(a). We perform the SES analysis and scope measurement, arriving at the traces in Fig. 2.9(b), equivalent to Fig. 2.8(d),(e)(iii). Here, we see some discrepancy in the traces. We take the Fast Fourier Transform (FFT) in Fig. 2.9(c).

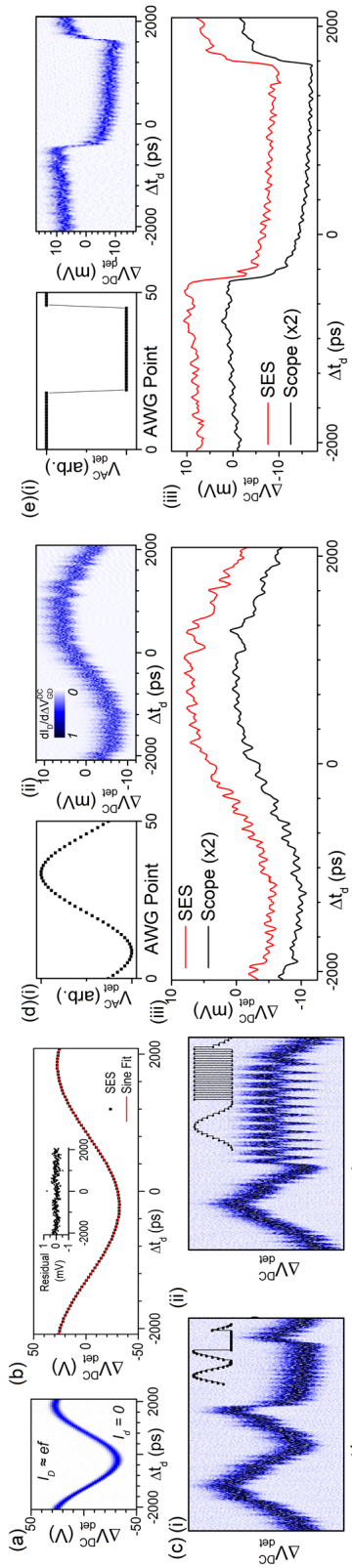


Figure 2.8: Example results from use of the SES scheme. (a) A detector map, as seen in Fig. 2.4, with the form of $V_{det}^{AC}$ a sine wave. (b) Extraction of the point of the maximum derivative $dI_d/dV_{det}^{DC}$ gives the position of the waveform in voltage space (black points). We fit a sine curve (red) to the data, and taking the residual (inset) shows excellent agreement. (c) Further examples of SES measurement outcomes, with different Test signals. The AWG construction is sketched in the inset. (d)(i) For quantitative analysis of the accuracy of the SES method, we construct a sine wave on the AWG. (ii) The SES measurement result from this Test signal, noting that the AWG output is not filtered so higher harmonics are also present. (iii) Extraction of the peak points (red) show very clear similarity to the same waveform as measured by a Tektronix MSO72034DX sampling oscilloscope (black). (e)(i-iii) As (d) with the case of a square wave as the Test waveform, showing good agreement in the step. Adapted from Johnson [65].

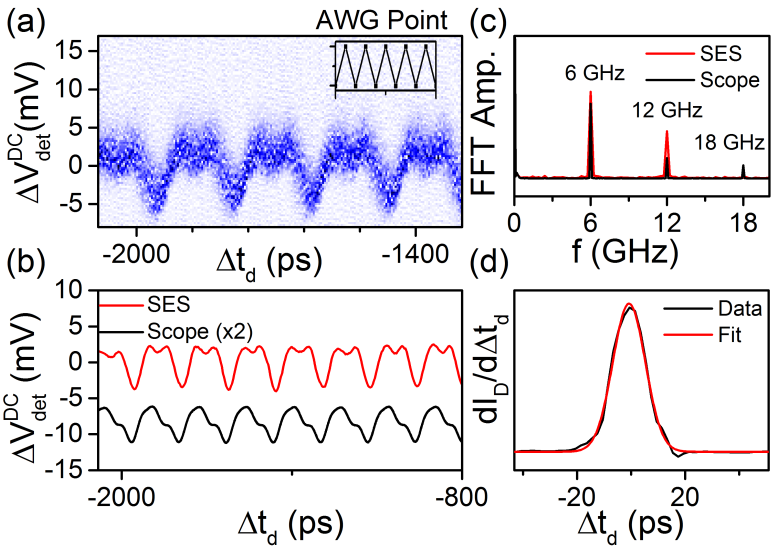


Figure 2.9: (a) The highest frequency waveform we can construct: a two point construction (inset) run at 12GS/s gives a 6 GHz waveform. However, our SES scheme result shows a further oscillation. (b) The extraction from the colourmap (a) of the SES scheme result (red), and the equivalent trace as measured by the sampling oscilloscope (black). (c) The FFTs of the two traces in (b) shows similarity, except the scope records a peak at 18 GHz which is not seen in the SES scheme trace. (d) Estimation of the bandwidth of the SES system by measurement of the wavepacket temporal size. We perform a Gaussian fit to the trace (red) to find the Full Width at Half Maximum (FWHM). Taken from Johnson [65].

The peaks here are from the 6 GHz sampling rate, with the first and second harmonic also visible. The SES scheme reports a higher amplitude of the 6 and 12 GHz peaks, but no 18 GHz peak, which is only visible in the scope trace. It is difficult to be sure of the origin of this discrepancy, but we suggest it arises where the lines for each measurement differ. For the scope measurements, we use the probe on the bench, and in place of the sample and sample holder, we connect a coaxial line of $\sim 1$ m to the scope. This suggests that the sample holder, and/or the Au bond wires, or the lines on the sample itself, have a lower bandwidth than the probe lines. This is plausible owing to the several non-conventional joints made to connect with the sample. However, at this stage, we cannot rule out that the absence of an 18 GHz peak is due to the SES method alone.

We suggest the measurement lines are the limiting factor to the bandwidth over the SES method due to the short interaction time of the electron with the Test waveform on the detector barrier. But to understand the SES bandwidth, we need to know how long the electron interacts with the detector barrier. This is the convolution of electron wavepacket temporal size (the Arrival Time Distribution (ATD)) with the detector barrier transmission, which together determine the time taken for transmission across the detector to vary from 0 to 1. This idea is more fully developed in Ch. 5. The ATD of the electron wavepacket is the fundamental limit to the bandwidth (we can always make the detector barrier transmission function sharper by increasing the detector line bandwidth, in theory at least). We measure the ATD by examining the minimum temporal width of transmission, which occurs when using a sharp riser in $V_{det}^{AC}$ such as the square wave used above. This minimises the contribution to the ATD of the detector transmission. Such a measurement is shown in Fig. 2.9(d), where we again plot the derivative $dI_d/d\Delta t_d$. This trace fits well to a Gaussian, as we expect (see Sec. 5.1) as shown in red. Taking the FWHM of this fit as fair measurement of the ATD width, we arrive at a value of 14 ps.

Now we are in a position to comment upon the bandwidth of the SES scheme. From the FFT alone, we could only conclude that the limit of the SES scheme may be only a

little more than 12 GHz. But examining the wavepacket we can see that plausibly we can sample $\frac{1}{2}\frac{1}{14ps} \sim 35$ GHz, and that our limitation here is due to the lines alone. Further, we see evidence that the ATD is tunable (this is the subject of Ch. 5), and we can measure smaller temporal size [77]. This is supported by a theoretical study by Ryu [68]. To develop 100 GHz resolution we require a width of 5 ps, which as we will show later, is plausible.

## 2.6 Conclusions

We have developed a technique whereby we can detect propagating hot electrons with 1 meV and $\sim 5$ ps resolution. There is scope to increase these further, with bandwidth improvement and use of a component of $V_{det}^{AC}$ in antiphase to $V_{G1}^{AC}$ to reduce crosstalk. In theory, this will work in single shot mode, for example by using a QPC or SET [61, 66] as a charge sensor on one of the terminals downstream of the detector. Whilst this would make us sensitive to pumping errors, it is far more likely there is a sensing error at the current level of sensitivity of single shot charge detectors. One could parallelise this method, thus building up our waveform picture, with each detector/QPC contributing a pixel. Of more significance to the wider community, we have provided a means by which high frequency signals can be measured in the cryogenic environment. These signals are hard to extract from this environment owing to the bandwidth restriction imposed by having multiple lines and joints present. We have developed a step towards matching room temperature capability in the cryogenic environment, which could be used in performing quantum measurements.

# Chapter 3

# Measurement of Electron Velocity

## 3.0 Introduction

In this chapter we put our electron pump and single electron sampling scheme to use in measuring the velocity of pumped electrons. The velocity, along with the wavepacket size in time and propagation direction, have important implications for the design of an interferometer. Also, this was a unique study in itself: the velocity had never been measured before. As we shall see, this study also produced very intriguing results that I further studied in the next chapter.

Associated publication: **Time-of-Flight Measurements of Single-Electron Wave Packets in Quantum Hall Edge States**

M. Kataoka, N. Johnson, C. Emary, P. See, J.P. Griffiths, G.A.C. Jones, I. Farrer, D.A. Ritchie, M. Pepper, and T.J.B.M Janssen

**Physical Review Letters 116** 126803 *2016*

goo.gl/azTp9D

*N.J. performed the measurements and analysis; M.K. wrote the paper and provided supervision; C.E. provided theory; P.S fabricated the sample with assistance from J.P.G, G.A.C.J, I.F, D.A.R; M.P and T.J.B.M.J provided support.*

## 3.1 Electron Velocity

To utilise the electron pump system as more than a current source, we need to demonstrate coherence of the wavepacket. This would then mean the pump can possibly be used to create specific states for use in quantum information processing [63,78] or as an entanglement source [79] or flying qubit [80]. One way we are actively working to demonstrate wavepacket coherence is through performing the "Fermion quantum optics" experiments. This is the electronic analogue to quantum optics, experiments that reveal interference and the quantum behaviour of light. Finding interference in this hot electron system is the necessary first step to these technological applications. In order to do this, we need to know some properties of the electron wavepacket. The original idea was to construct an Aharanov-Bohm ring (see Sec. 6.2), which consists of splitting the electron paths into two, and recombining them [81, 82]. Presence of Aharanov-Bohm oscillations would imply phase coherence of the wavefunction on leaving the electron pump. We need to know the wavepacket length in the propagation direction (i.e. within the edge state) for self interference. This will tell us what the path length in the ring will need to be to see self interference. Secondly, we need to know that the propagation in the edge states is robust (i.e. there are no decoherence mechanisms). For these applications, we will need to know the velocity and dispersion, and that is what we measure in this chapter.

There are a few precedents. The velocity of quasiparticles propagating in edge states at the Fermi Energy $E_F$ has been studied [83–86], although these states are not expected to be coherent. Perhaps the closest precedent to this study is the work of McClure [87], which measured edge state velocity in a more direct way comparable to what we do here, although again close to $E_F$. Recall we understand electrons to propagate in edge states analogous to those seen in transport at the Fermi Energy in the presence of a perpendicular magnetic field to the 2DEG plane but at a much higher energy. They will undergo motion as $\mathbf{E} \times \mathbf{B}$ drift. We shall discuss this motion in the context of our results later.

## 3.2 First Device

The first device tested is shown in Fig. 3.1, with electrical schematic. This sample was measured in the He-3 cryostat. The electron pump gates $G_1$ and $G_2$ are shown in red. Pumped electrons travel in the edge states marked in red or blue in the presence of a perpendicular magnetic field. These electrons are incident upon the detector barrier $G_{det}$. Between the pump and detector, we have two deflection gates $G_{def}$, shaded in yellow. By tuning these gates we can determine which route the current takes. If the potential on the deflection gates is lower than the pumped electron energy (more positive voltage), the hot electron current can pass over the barrier and underneath the gate, and hence taking the "short" route (red line in Fig. 3.1 of length 5 $\mu$m). If the potential on the gates is high (more negative voltage) the hot electron current is deflected from the barrier, and takes the long route (blue) of length 9 $\mu$m. There is a small voltage region in which we see partial transmission. The ring is defined by e-beam etching, and so no current may tunnel across this void, and is forced to travel around the ring. We note that in the path lengths common to both short and long routes, we expect the spatial location of the paths to be the same. On the far side of the lower $G_{def}$ the paths are reunited for detection. Hence, we have defined a path of known length that we can measure the time of flight along. This is the path length given by the difference between long and short route, which is the length around the ring. The upper deflection gate $G_{def}^{up}$ is not so important for velocity measurements. It was designed in case we could try interferometry, and could then be used at half transmission to drain charge to ground at the top ohmic. As we found out, such an experiment is not possible with this design.

We note that we require a separate path as we cannot measure velocity along the short route directly. This is because it is difficult to know the phase difference between the two AC signals $V_{G1}^{AC}$ and $V_{det}^{AC}$ with picosecond accuracy. Further, even if that could be achieved, we would not know the point in the driving waveform $V_{G1}^{AC}$ at which the electron is emitted from the pump with high accuracy [67]. Therefore, we are forced to conduct a time of flight

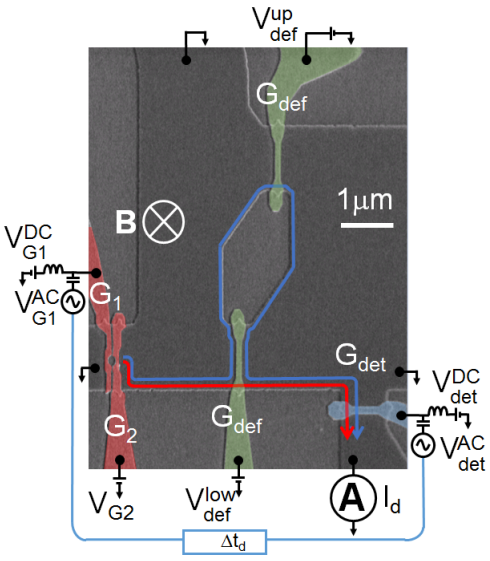


Figure 3.1: The first device, with schematic of electrical contacts. The 2DEG region is the darker coloured region, with a hole etched in the middle (lighter region). Gates are shaded: pump gates $G_1$ and $G_2$ (red), detector gate $G_{det}$ (blue), and deflection gates $G_{def}$ (green). The electron edge states are shaded: red, short path, of length 5 $\mu$m, and blue, long path, of length 9 $\mu$m. In the shared lengths, these paths will be in the same position.

measurement.

### 3.2.1 Results

For this work, we run the electron pump at 240 MHz, producing a current $I_p = 38$ pA. If we send this current via the short path, the detector records the map shown in Fig. 3.2. Here in (a), the horizontal axis is $V_{det}^{DC}$, ($V_{det}^{AC} = 0$), and the vertical axis $V_{G2}$, proportional to the pumping energy (c.f. Fig. 2.3). In the left panel we plot $I_d$ in the colourscale and in the right panel $dI_d/dV_{det}^{DC}$ for clarity. For the rest of this work we shall only use the derivative maps as they more clearly show transitions of current in the detector. In this plot we see that we do not recover the pumped current $I_p$ at a single energy. The sharp diagonal lines in the derivative (b) show that the energy we recover current at is quantised. We conclude the electrons are relaxing by emission of Longitudinal-Optical (LO) phonons, which is quantised in GaAs at 36 meV and has been observed before [8, 54, 57, 67, 88]. We study this emission in Chapter 4. For now, we conclude that this has a detrimental effect on the experiment. If

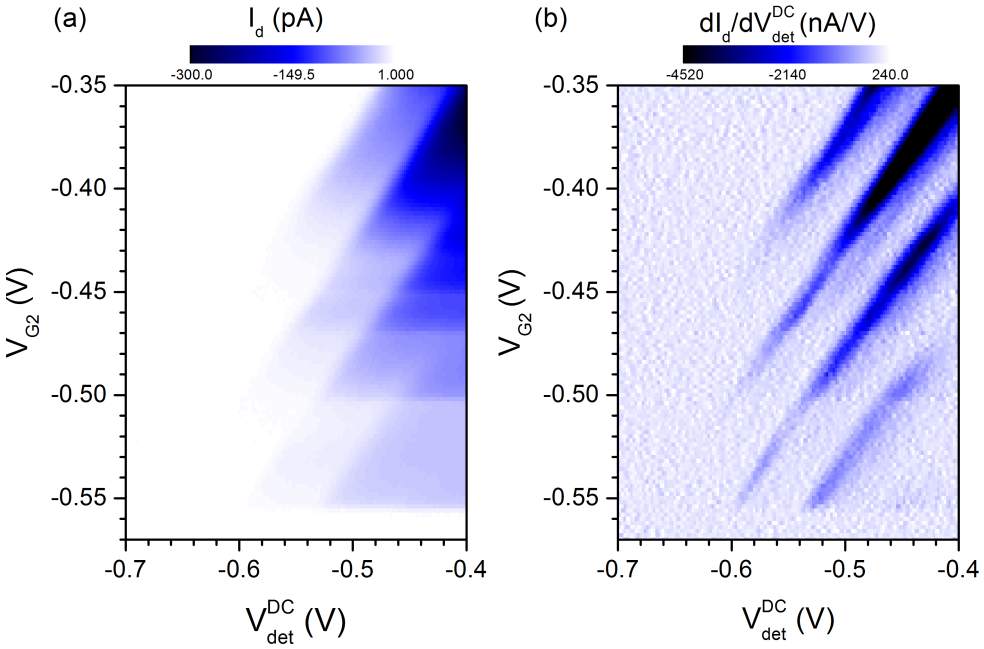


Figure 3.2: Detector maps showing multiple LO-phonon emissions. (a) Current $I_d$ in the colourscale, (b) with derivative $dI_d/dV_{det}^{DC}$. In each case we see the clear transition of current across the detector, as was presented in Fig. 2.3, duplicated by electrons that have emitted one or more LO-phonons. The leftmost (highest energy) transition shows electrons propagating at the original pumping energy. We explore this in more detail in Fig. 3.3.

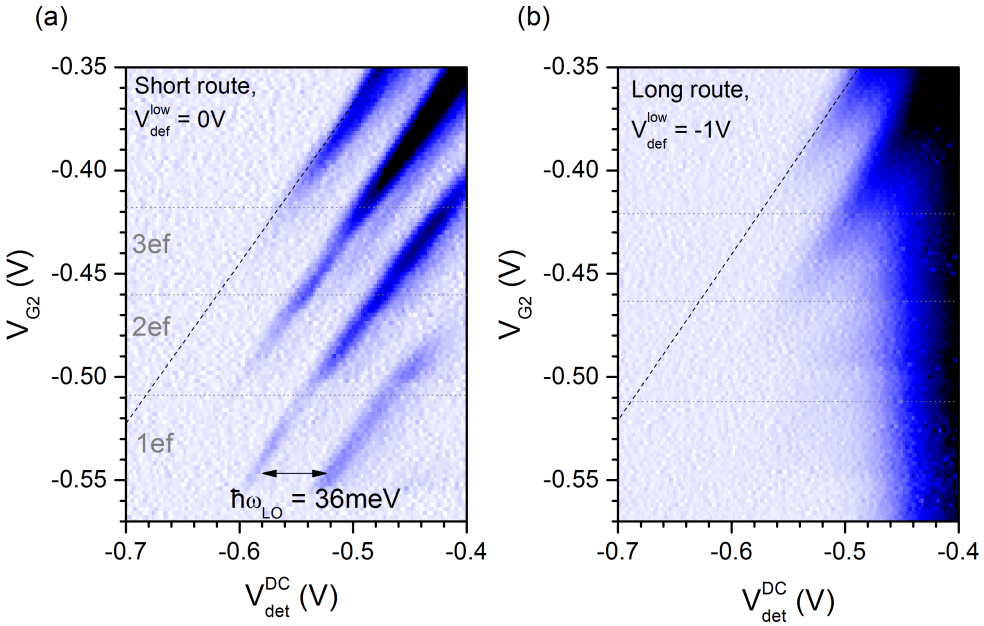


Figure 3.3: Comparison of the current after traveling the short (a) and long (b) routes. The dashed line marks the original pumping energy. Arrival at the detector in quantised energies implies LO phonon emission.

electrons relax to $E_F$ they are not detectable [1]. We wish to measure the velocity as pumped only.

In Fig. 3.3(a) we explore this energy loss further. First we extend the line seen at the highest energy, corresponding to the pump emission energy. Horizontal dotted lines mark transitions between pumping plateaus. For the first pump plateau ($I_p = 1ef$), no current is recovered at the pumped energy, with multiple LO emissions taking place. As we move to higher plateaus, the electron energy and timing spacing becomes closer together, and is much harder to resolve. In Fig. 3.2(b)(ii) we plot the equivalent map with the current taking the long route. We see there is more phonon emission, with the weight of the lines reflecting a higher current value recovered at that stage. This is because there is more LO emission in the longer time of flight. We only change $V_{def}^{low}$ to change the current path from short to long route.

This is impossible to work with in this form. The path lengths are long enough for

[1]Due to rectified current from $V_{G1}^{AC}$, our detector barrier has no resolution of energies up to many tens of meV above $E_F$.

multiple phonon scattering events to be observed, which occurs at an increased rate at higher energy (on the first plateau). However, two upsides come of this situation. Firstly, we can use the quantised value of the LO phonon to calibrate the detector energy axis. As shown on Fig. 3.3(b)(i), the separation of the LO emission lines must be 36 meV [57]. Secondly, we observe deflection gate dependence of the emission, which is shown in Fig. 3.4.

In Fig. 3.4, we compare the form of $I_d$ under four different propagation conditions. Recall, in each panel, the leftmost transition (line) marks the original pumping energy. The coordinates above each panel denote the two deflection gate voltage values (lower $V_{def}^{low}$, upper $V_{def}^{up}$). In (a), we duplicate Fig. 3.3(a), with $(V_{def}^{low}, V_{def}^{up}) = (0,0)$V and the current taking the short route. In panel (b) we observe that we can recover more current at higher energies with less LO phonon emission if we set the lower deflection barrier to be high (but not so high to induce pinch off). We also observe that if we increase the top deflection barrier, there is less hot current preservation relative to (a), as shown in (c), with deflection barrier potentials (0, -0.4)V. Note that the hot current takes only the short route here, and also the off-scale current to the right of the plots is rectified current from AC oscillations in the 2DEG or ohmic contacts from the pump drive, and is known to be strongly a function of the gate voltages [46]. In (d), we see the clearest definition of the quantised transitions at the empirically tuned barrier potentials (-0.675, -0.2)V. The working theory we derived was that voltage on the gates raises the potential profile beneath the hot electron (as per a Schottky barrier). When the profile bottom was raised to be closer to the pumped energy, less emission was seen. Formalisation of this statement is the subject of Chapter 4. Some mystery remains regarding the action of the upper deflection gate on the lower route, which seems to decrease definition of the current fractions with increased potential. Perhaps this is a subtle form of electron-electron interaction, with pumped electrons interacting with Fermi sea electrons propagating in edge states driven by rectified current, and moved physically closer to the pumped current by the upper deflection barrier.

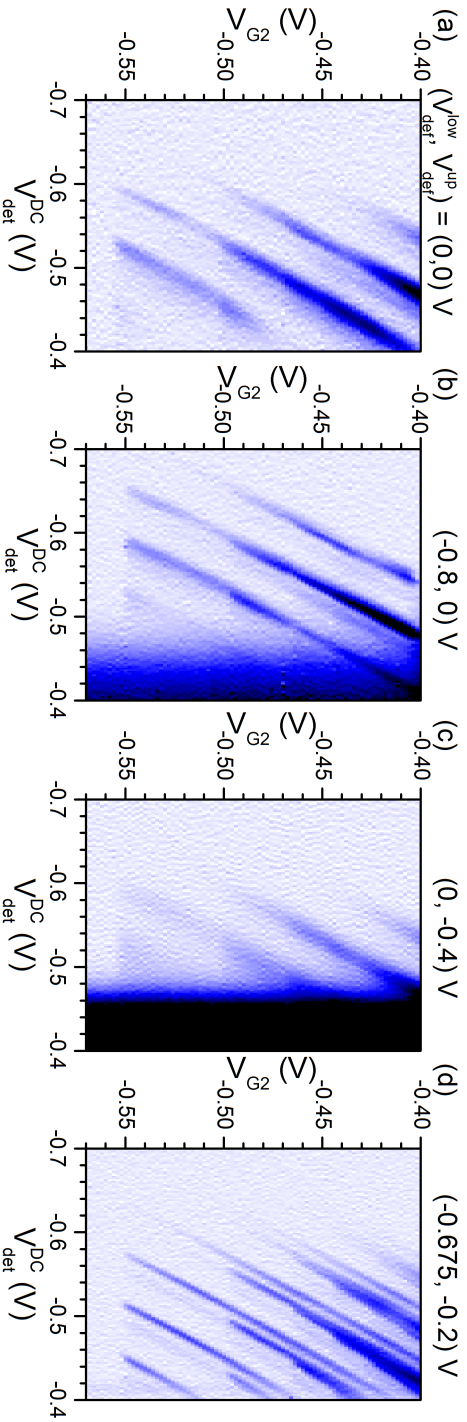


Figure 3.4: Dependence on the deflection gates of the quantity of the LO-phonon emission. As we change the parameters $V_{def}^{up}$ and $V_{def}^{low}$ we notice the quantity of LO emission varies, as shown by the line intensities, and also the definition of the current fractions also changes. Refer to text for discussion of the meaning of the line intensities.

## 3.3 Second Device

This last result in mind, we extended what was the upper deflection gate to cover the entire path length. We rename this gate the "depletion" gate. This device is shown in Fig 3.5(a).

The device is colour coded as before (Fig. 3.1). The new gate, in yellow, is the depletion gate $G_{dep}$ with potential $V_{dep}$. In Fig 3.5(b) we show the equivalent detector energy maps to Fig. 3.3, with current taking the short route in (b)(i) and the long route in (b)(ii). We see we can now recover the full current at a single energy transition, equal to the pumping energy when $G_{dep}$ is energised. In the publication we used two devices of this form, with different ring lengths, to confirm that we measure the same velocity trends in each. In both, the short route is 5 $\mu$m and the long routes 20 or 13 $\mu$m.

### 3.3.1 Velocity Measurement

Fig. 3.6 shows the principle of the measurement. We choose a square wave for the detector temporal measurement ($V_{det}^{AC}$), shown in (a), because it has a sharp time profile in the step, which makes its position in the time domain easier to track, shown in full in the left hand panel, with the sharp step highlighted in the boxed region. We choose a small amplitude of $V_{det}^{AC}$ to avoid back-action on the pump. This was determined by establishing the amplitude limit at which the temporal wavepacket ATD was not seen to change its temporal width (we now know this idea to be a bit flawed, see Ch. 5).

The procedure for measuring the time of flight is as follows. Throughout the rest of this chapter, $V_{dep}$ is held at a constant value, tuned such that no LO phonons were seen to be emitted around the long route. When $V_{def}$ is low (more positive) the pumped current can pass over the barrier and takes the short route (case (b)(i) in Fig. 3.6). It arrives at the detector, sampling the square waveform as explained in Chapter 2. We note down the position in time of the sharp step in $V_{det}^{AC}$, which will be some arbitrary phase between the two AC sources, $\Delta t_d$. As we increase $V_{def}$ (more negative voltage) we reach a point with

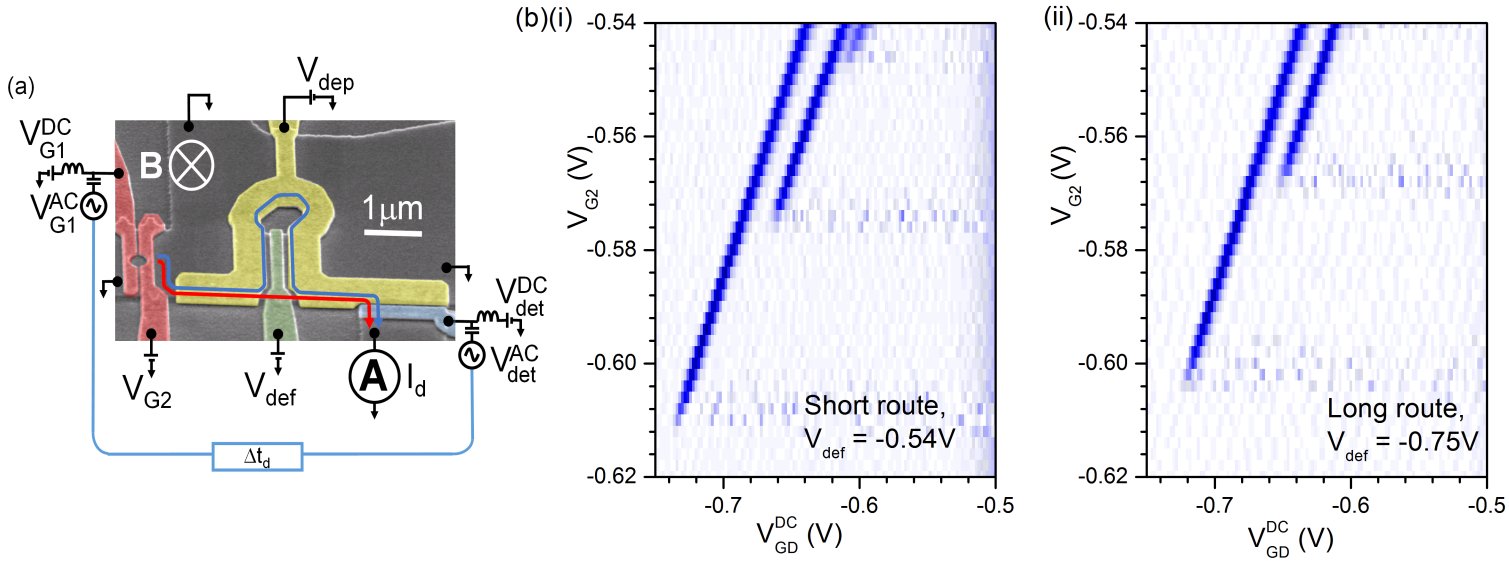


Figure 3.5: The second device, with gates using the same colouring as for the first device (shown in Fig. 3.1), with the new depletion gate in yellow. (b) The two detector energy maps, showing only one energy at which the pumped current is collected - the original pumping energy, for both the short (left) and long (right) routes. Note the second line at lower energy is the contribution from the second pumped electron per cycle.

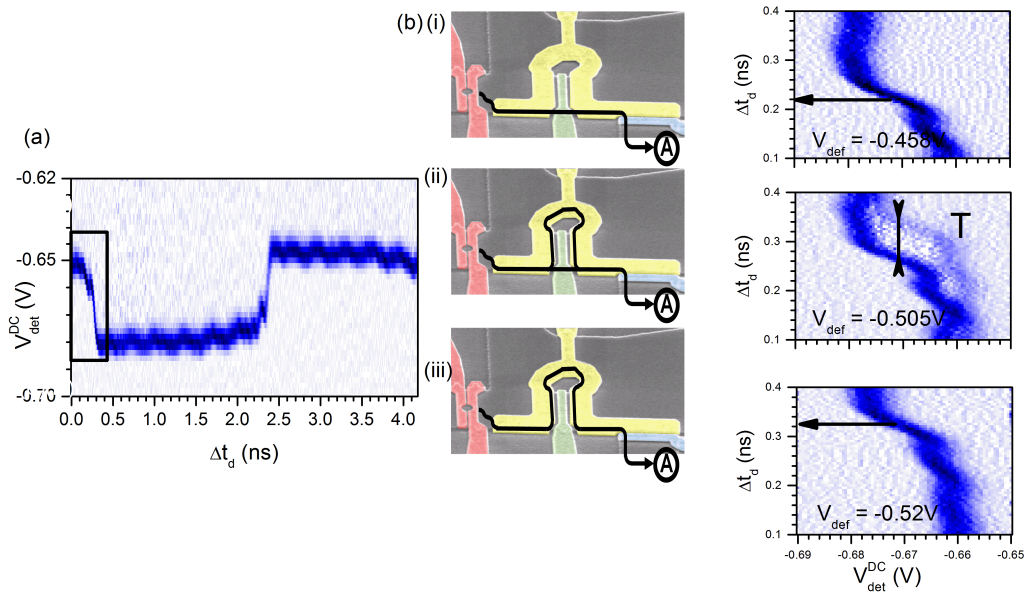


Figure 3.6: The time of flight measurement principle. (a) We use a square wave form for $V_{det}^{AC}$ and track its sharp time profile at the step (boxed region). (b) As we change the electron route using $V_{def}$ from short (i) to long (iii), we see the time of arrival change as the electron has further to travel. This difference in arrival time is a measure of the time of flight $T$, as marked.

half transmission across the barrier (case (ii)). We see now that while some of the current still takes the short route, and arrives at the previously observed time, some current travels around the ring with an extra 5 $\mu$m and hence arrives later. We also use another sample with the same design and a ring length of 2 $\mu$m. It then samples the detector barrier potential $V_{det}^{AC}$ as before, but this is offset in the time axis. If we continue to increase the height of the deflection barrier by increasing $V_{def}$, then all current is forced to take the long route, and arrives at the later time (case(iii)). The time of flight $T$ is then easily read as the interval between the two sharp steps in the waveform, as shown in case (b)(ii). However, when we track the electron time of arrival in this way, we observe that the time of flight is strongly a function of the deflection gate voltage $V_{def}$. This is plotted in Fig. 3.7.

In the discussion here, we take our path lengths to be the lithographically defined lengths, but we have no information about the actual path taken by the electron. What we may assume is that whatever the path length, it is likely to not vary much across our measured energies, because we record smooth dependency in the velocity as a function of energy. This

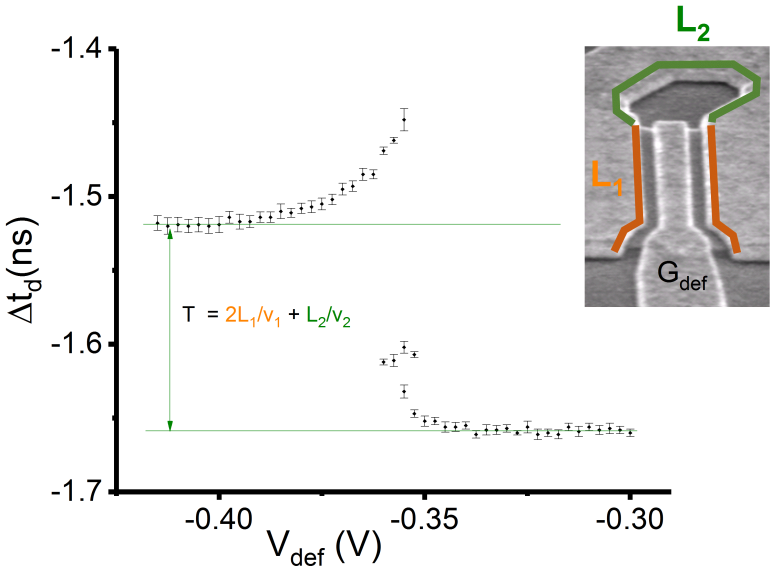


Figure 3.7: How the time of flight changes as a function of $V_{def}$. To explain this, we split the long route into two regions, $L_1$ and $L_2$. The interval between the stable values for each route is taken to calculate the velocity $v$.

adds the same systematic error to all velocity values, but does not affect the conclusions we make. The error in the time of flight arises because our ATD spans a range of $\Delta t_d$, so it is proportional to the width of the derivative $dI_d/dV_{det}^{DC}$.

In Fig. 3.7, the current transitions between short and long routes (right to left on the plot). Arrival time is stable when the potential $V_{def}$ is much less than the pumped electron energy. As $V_{def}$ approaches the hot electron pinch off region (middle of plot), the time of arrival begins to move to a later time. Past pinch-off the current is deflected to take the long route and we see a jump in the time of arrival to the later time. As we increase $V_{dep}$, the time of arrival smoothly moves to an earlier time, gradually tending to a stable value. This can be explained as follows. In the regime close to pinch off, the current is still taking the short route, but perhaps a different path underneath $G_{def}$. This increases its total path length and hence the current arrives later. This can be understood by considering that the gate may not pinch off uniformly across the 1.5 $\mu$m channel, due to impurities creating an inhomogeneous potential profile. Additionally, there will be some change in the velocity in

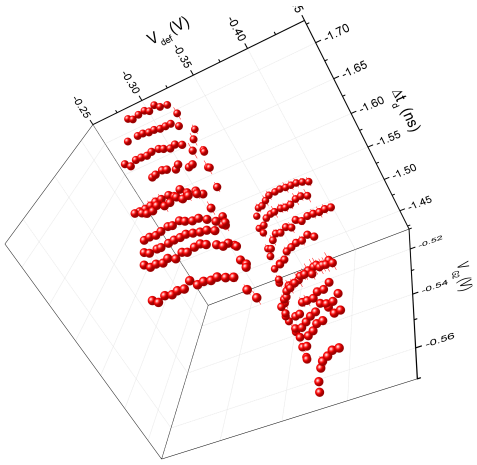


Figure 3.8: Times of arrival as a function of $V_{def}$ and pumped energy, set by $V_{G2}$, showing the similarity of the form of the transition from short to long route, as all the traces make the transition from short to long route with the same form.

the vicinity of the gate due to the change in potential profile (see later), but because the gate width is only 300 nm out of 5 $\mu$m, this contribution is minor compared to the longer route. We interpret the settling of the time of arrival in the long route as due to the action of the deflection gate. There exists two potential profiles in the long route (three including the section common to the short path, but this length is not important). The first is in the length alongside $G_{def}$, 3 $\mu$m (2 $\times$ 1.5 $\mu$m), which we denote $L_1$, and the second is the ring length $L_2$. The potential profile, which sets the velocity (as we establish in the next section), is constant for the ring $L_2$ but will strongly depend on $V_{def}$ in $L_1$. The total time of flight around the ring is then $T = \frac{2L_1}{v_1} + \frac{L_2}{v_2}$, with $v_{1(2)}$ the velocity in each length $L_{1(2)}$. As $V_{def}$ increases, the potential profile along the barrier becomes sharper, and so $v_1$ increases. Hence we see the time of arrival stabilise because the the contribution to the time of flight $T$ from the term in $L_1$ becomes ever smaller. To calculate the velocity we take the stable short and long route times of arrival, as marked on Fig. 3.7. This calculates the velocity $v \equiv v_2$ using the ring length only (excluding the path alongside $G_{def}$).

We note that the form of the deflection trace as plotted in Fig. 3.7 is general, and has been observed at all pumping energies and in all samples. An example of this is shown in Fig. 3.8. In this plot we present the trace of Fig. 3.7 as before, but with a third axis, the

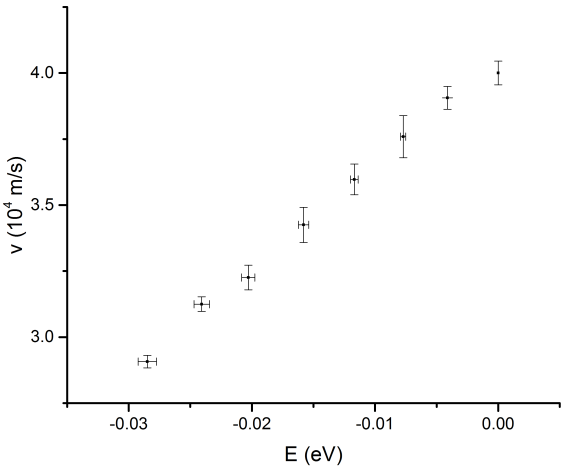


Figure 3.9: Velocity $v$ as a function of pumping energy $E$. Note we take $E = 0$ as the highest attainable energy by the pump.

electron pumping energy (set by $V_{G2}$). We see the familiar trace of Fig. 3.7 at all energies (and for subsequent pumped electrons, not shown). This plot shows us that for all energies, nothing "special" happens along the path lengths. All electrons interact with the barrier $G_{def}$ in a similar way. Also, we see a change in the time of emission in the pump probably due to the crosstalk between the gates. This is the shift to later times in short path times of arrival in the energy $V_{G2}$ domain. This should not affect the measured velocity.

We are now in a position to plot the velocity $v$ as a function of pumping energy. This is plotted in Fig. 3.9. In this figure, we plot in real energy units by using the LO phonon to calibrate the detector barrier and the gradient of $V_{G2}$ (see Fig. 3.3). We choose the highest attainable pumping energy to have the coordinate $E = 0$. $v$ varies almost linearly with $E$, whereas perhaps it should vary as $\sqrt{E}$, although we measure quite a small energy range so it is a little ambiguous.

Next, we repeat the measurement of velocity as a function of the perpendicular applied magnetic field $B$. This is plotted in Fig. 3.10. This shows a clear $1/B$ dependence, which is in agreement with the electrons' motion as $\mathbf{E} \times \mathbf{B}$ drift. The significance of this is discussed in the next section.

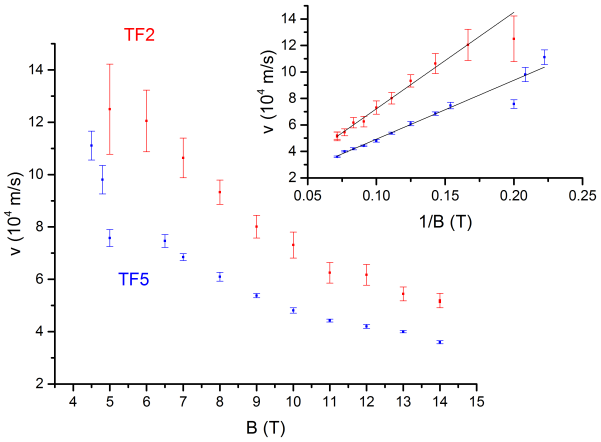


Figure 3.10: Velocity $v$ as a function of field $B$. Upper right panel: plotting the data with $1/B$ on the horizontal axis shows clearly the $\mathbf{E} \times \mathbf{B}$ drift.

## 3.4 Measurement of the potential profile

So what determines $v$? It should be the potential profile through the confinement $\omega_y$ [52]. It is understood this profile should be parabolic in $y$, from our derivation of the edge states (see Sec. 2.1, also [50]). We find there are two ways to measure this potential profile: empirically or via the dispersion relation.

### 3.4.1 Determination of profile via Electric field

For the empirical way, we evaluate the Lorentz force acting on the propagating electron. This is $\mathbf{F} = e\mathbf{E} + \mathbf{v} \times \mathbf{B}$. Here, $\mathbf{E}$ is the electric field (NB. we use $E$ as the electron energy). The velocity is found as $(\mathbf{E} \times \mathbf{B})/B^2$, which in a perpendicular magnetic field simplifies to $v = \frac{E}{B}$ [1]. Hence, by multiplying each measured velocity by $B$ we derive a local electric field value.

We note the electric field has units of inverse length, so we rearrange to get a (relative) translation in $y$ (perpendicular to electron motion). This is the change in pumping energy

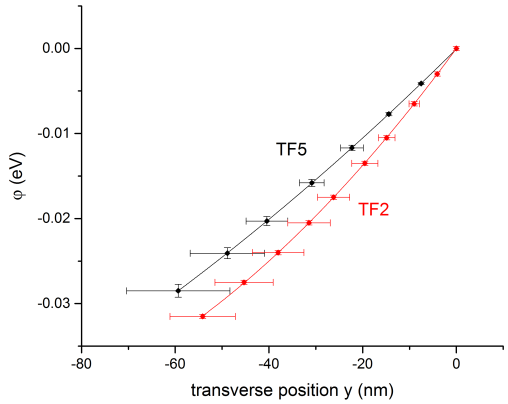


Figure 3.11: The transverse profile $y$ as a function of potential $\phi$, found by varying the pumping energy $E$ for the two samples used in the paper, the 2 and 5 $\mu$m ring lengths denoted by TF2 and TF5 respectively.

$E$ / average electric field $\mathbf{E}$, taken pairwise:

$$y_n = y_{n-1} - \frac{|E_n - E_{n-1}|}{\frac{1}{2}\left(|\mathbf{E}_n| + |\mathbf{E}_{n-1}|\right)} \tag{3.1}$$

Fig. 3.11 shows the derivation of transverse displacement $y$ as a function of the potential $\phi$, which is related to the energy $E$. We see that the errors will accumulate pairwise.

This displacement maps the potential profile. We fit a parabola to this data, which fits reasonably, as we expect. (However, one could argue that a linear fit could be more appropriate, but the agreement between theory and experiment discussed next supports a parabola.) Some quick check measurements of the velocity found it to be broadly independent of $V_{G1}^{DC}$ and $V_{G1}^{AC}$. We can calculate the transverse ($y$) confinement energy $\hbar\omega_y$ by noting the form of the potential profile is $\phi = -m^*\omega_y^2 y^2$ and rearranging.

### 3.4.2 Determination of the potential profile via the dispersion relation

An alternative, but complementary, way to determine the potential profile as we did in the previous subsection is to calculate the confinement energy, as suggested by our co-author C.

Emary. For this, we follow the elegant derivation of sub-bands in Datta [52].

These magneto-optical sub-bands are somewhat similar to the Landau Levels. We again solve the QHO (in the limit that our confining potential is parabolic) and so have eigenvalues of form

$$E(n,k) = \epsilon_0 + \left(n + \frac{1}{2}\right)\hbar\left(\sqrt{\omega_y^2 + \omega_0^2}\right) + \frac{\hbar^2 k^2}{2\ m^*}\frac{\omega_y^2}{\omega_y^2 + \omega_0^2} \tag{3.2}$$

with $\epsilon_0$ the lowest band energy, $n$ the Landau Level index, $\omega_c$ the cylcotron energy ($= \frac{eB}{m^*}$), $m^*$ the reduced mass and $\omega_y$ the $y$-confinement. The potential profile must be parabolic to admit this solution, of form $\phi = -m^*\omega_y^2 y^2/2e$. The eigenvectors of the Schrödinger equation form plane waves, which travel with group velocity

$$v = \frac{1}{\hbar}\frac{dE}{dk}. \tag{3.3}$$

Equating these two expressions, and simplifying for $\omega_c > \omega_y$ (high field limit, as in the experiment) we derive

$$\frac{1}{2}m^* v^2 = \frac{\omega_y^2}{\omega_c^2}\left(E - \epsilon_0 - \frac{1}{2}\hbar\omega_c\right). \tag{3.4}$$

To extract $\omega_y$, we take a straight line fit to a plot of $v^2$ vs $E$, as shown in Fig. 3.12. This assumes a parabolic confinement of the form above.

A linear fit to the data implies this is in agreement, and we measure $\hbar\omega_y \sim 1.8$ meV (TF2 - 2$\mu$m ring length) and 2.7 meV (TF5 - 5$\mu$m ring length) for each sample used in the published work. At very low energies, a linear fit may not be appropriate (not parabolic confinement), as there is deviation from the straight line fit, and we omit the lowest energy point for TF2 device from the fit. A fit also shows us how far our electron propagates from the band bottom, denoted $\Delta E$, of -61 and -47 meV for each sample. Again, the potential energy of the electron can be found as $-e\phi$ ($\phi = -m^*\omega_y^2 y^2/2e$). We can then solve the above equation for $y$.

Comparing the two methods of determining the confinement $\hbar\omega_y$ gives 1.6 meV (electric field approach) and 1.8 meV (dispersion relation approach) for TF5 and 2.7 meV for both

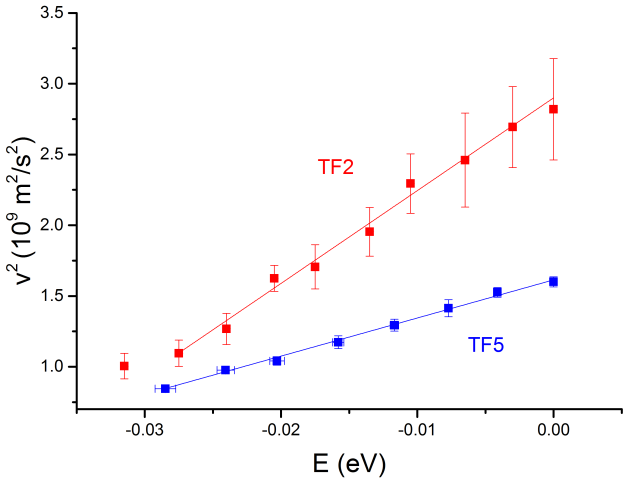


Figure 3.12: Plot of $v^2$ with electron energy $E$ shows good linearity except at the lowest energies, with the fit giving the transverse confinement $\hbar\omega_y$.

approaches for TF2. We would expect the values obtained to be the same, and the discrepancy probably arises from the parabola more accurately fitting all the data, including the lowest energy point which lies some way from the fit line of linear dispersion in Fig. 3.12. This implies that the profile is deviating from a parabola at these energies, or that we cannot assume linear dispersion. We suspect that this is near the bottom of the potential profile, which may not be completely smooth. We defer discussion of this for the next chapter, in which we shall delve deeper into the nature of the potential profile.

## 3.5 Conclusions

We have made the first measurement of electron velocity at an energy higher than the Fermi Energy. This value is typically in the range 5-10 $\times 10^4$ m/s. We mapped this to a potential profile using two methods with good agreement. We found that the edge potential profile is approximated best by a parabola, as expected. We find that electrons pumped at any energy sit on the same potential profile curve, implying pumping into just a single Landau Level. From the field dependence we confirm electron motion as $\mathbf{E} \times \mathbf{B}$ drift, with the breakdown of

1/B agreement at low field possibly because we see transition to skipping orbits (although it could just be that the velocity is hard to measure, as the time of flight becomes very short). We can estimate our wavepacket dimensions. The wavepacket size in $y$ should be set by the magnetic length $l_B = \sqrt{\frac{\hbar}{m^*\omega_c}} \sim 6 - 9$ nm. In the propagation direction $x$, the wavelength can be estimated using the technique described in Sec. 2.5. Taking 14 ps as an upper limit of wavepacket size in the temporal domain $t$, and a higher end velocity $v \sim 10^5$ m/s, then an upper bound to the wavepacket size is $tv \sim 1.5\mu$m. This has implications for an interferometer. If we want to measure self interference, we shall need to keep a path length less than this, which is impractical on fabrication grounds. This is why we moved to a Mach-Zehnder geometry in Ch. 6, as opposed to an A-B ring. We will also discuss a more quantitative approach to measuring the wavepacket size in Ch. 5. Next, we utilise our technique of mapping the potential profile to return to the issue of LO-phonon suppression we began this chapter with.

# Chapter 4

# Study of Hot Electron Relaxation

## 4.0 Introduction

In chapters 2 and 3, when we began experimenting with the detection barrier, we observed that the hot electrons lose energy. This has been reported by others in the literature, who identify the dominant relaxation mechanism as an LO-phonon emission. Further, we noted that we could suppress this relaxation by use of a depletion gate in Sec. 3.3. We went on to measure the electron velocity with this system. In this chapter we return to consider in detail the action of the depletion gate, and we derive a quantitative model to explain its action. We show that the experimental results elegantly map a theory based upon Fermi's Golden Rule for the case of LO phonons.

Associated publication: **Study of LO-phonon emission and suppression in a GaAs/AlGaAs heterostructure high above the Fermi Energy**

N. Johnson, C. Emary, S. Ryu, H.-S. Sim, P. See, J.P. Griffiths, G.A.C. Jones, I. Farrer, D.A. Ritchie, M. Pepper, T.J.B.M Janssen, and M. Kataoka

To be submitted to **Physical Review B**

*Author contributions: N.J. performed measurements, analysis and wrote the paper with assistance from M.K., C.E. provided numerical analysis for FGR with assistance from S.R,*

*H.-S.S; P.S fabricated the sample with assistance from J.P.G, G.A.C.J, I.F, D.A.R; M.P. and T.J.B.M.J provided support.*

## 4.1 LO-phonon emission

We have already established that pumped hot electrons propagate ballistically in edge states analogous to those observed in the quantum Hall effect. In the previous chapter, we mapped the spatial position of this state, and it was seen to be continuous over our measured energy range, implying transport in only a single Landau Level (likely the outermost (zeroth), also supported by the theoretical findings in Ref. [68]). When propagating in these states the hot electrons are seen to relax, as was first shown in Fig. 3.2. We reproduce this data in Fig. 4.1 and mark the interval concerned. In (a) we show the resulting detector map when LO-mode emission is present. We indicate the 36 meV LO-mode emission on the plot. In (b) we recover the situation in which we conducted the velocity measurements of the previous chapter, in which there is no detectable LO-mode emission. This arises only from increasing the potential of the depletion gate $V_{dep}$.

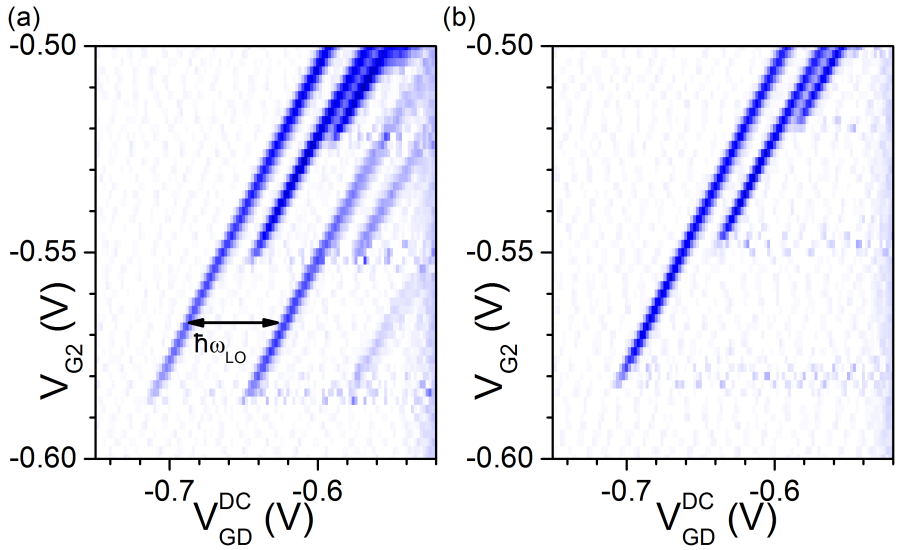


Figure 4.1: (a) Detector map showing clear LO-phonon emission, easily visible due to its quantised emission energy $\hbar\omega_{LO} = 36$ meV. (b) This emission may be suppressed by application of a potential $V_{dep}$ to the depletion gate $G_{dep}$.

Hickmott [89] had observed quantised emission when biasing current through a point contact, which was attributed to this mode. Optical measurements by Blakemore [90] had identified the LO mode to be dominant and quantised. Further studies using non - optical methods have confirmed this observation [54, 55, 91, 92], with some early theory of scattering [93]. Additionally, this quantised relaxation has been reported previously in our samples [8, 67]. The most comprehensive studies of this emission are due to Taubert [57, 94] and Emary [95]. These works present a comprehensive picture of LO-mode emission, but whilst the quantised energy of 36 meV has been measured many times and is now straightforward to identify, a measured rate has been elusive, owing to the need to know the electron velocity, which was not directly measured until the previous chapter of this work [57, 87]. The scattering theory is largely in place [88,92,95,96], but requires experimental verification, which has not been done before, because of this lack of direct rate measurement.

Next, we proceed to experimentally map the dependencies of this mode on our pumping parameters, and we then match this to a simple scattering theory based on Fermi's Golden rule (FGR) as constructed by Emary [95]. Importantly, we will see how the action of the depletion gate can suppress the emission, allowing far longer path lengths to be achieved, and allowed us to do the measurements of the previous chapter.

## 4.2 Measurement of LO phonon emission

For this work we use a time of flight device as was used in the last chapter. This sample was measured in the dilution refrigerator. Fig. 4.2 shows the sample and schematic of electrical connections made to it.

For this device we use a longer long path with ring length 20 $\mu$m. This allows for a more accurate determination of the phonon emission, as more phonons are emitted (explained next) and also gives an improvement in the accuracy of a measurement of velocity through a longer time of flight. As with the device of the preceding chapter, we have our electron pump

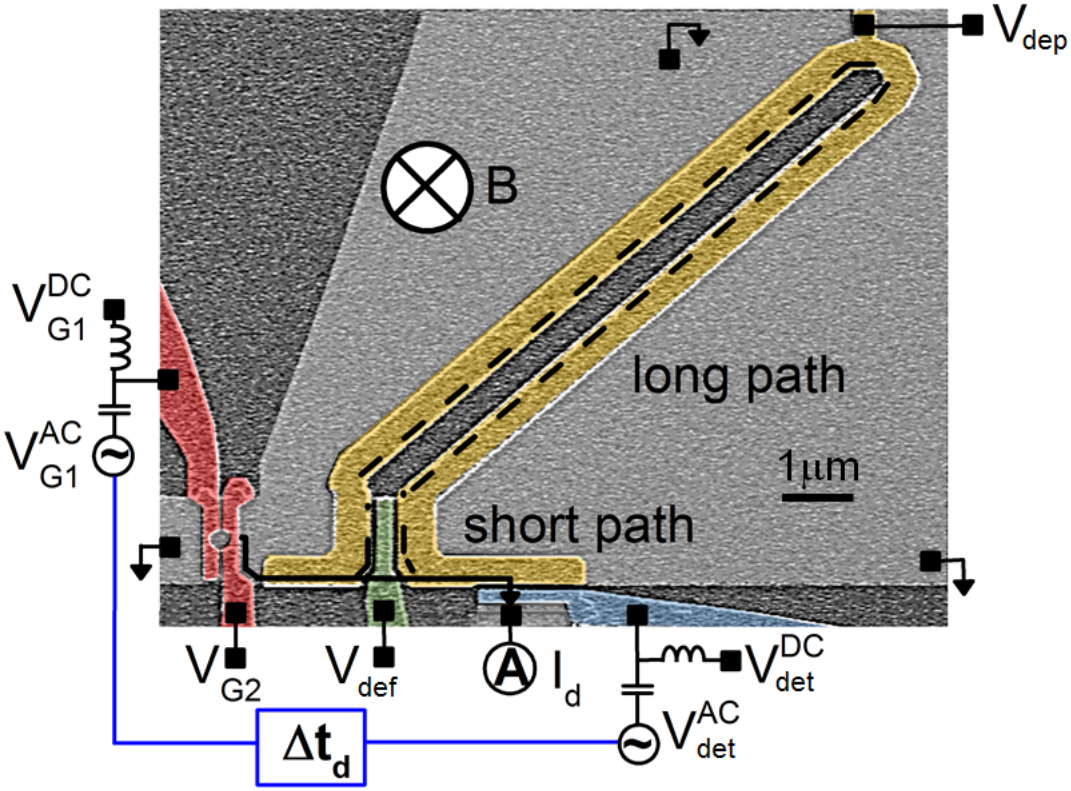


Figure 4.2: The time of flight design used in this work. It is almost identical to the devices used to measure the electron velocity in the previous chapter, except it has a much longer ring length of 20 $\mu$m. Short path length is 5 $\mu$m, long path is 28 $\mu$m. Gates are colour coded as Ch. 3: $G_{1,2}$ pump (red), $G_{det}$ detector (blue), $G_{def}$ deflection (green) and depletion $G_{dep}$ (yellow).

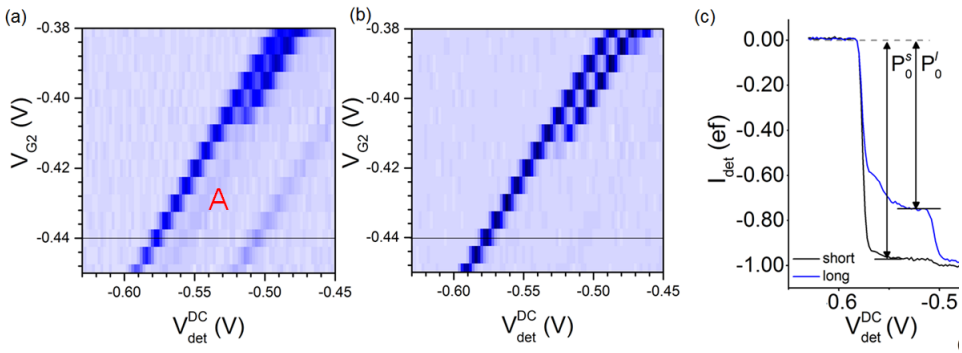


Figure 4.3: (a), (b) Detector maps of current taking the long route (a) and short route (b) show varying amounts of LO-phonon emission due to the difference in path length. The letter 'A' marks an unknown feature (light shading) at $\sim$ 10 mV lower potential $V_{det}^{DC}$. (c) Line cuts at the point marked by the black line in (a), (b) show clearly the fraction of current arriving having emitted zero or one phonon, which allows us to define the survival fraction $P_0$. Note that in (a), (b) we plot the horizontal derivative $dI_d/dV_{det}^{DC}$, whereas in (c) we plot the (non-differentiated) current $I_d$.

shaded in red ($G_1$ and $G_2$), with potentials $V_{G1} = V_{G1}^{AC} + V_{G1}^{DC}$ and $V_{G2}$. Our detector gate $G_{det}$ is shaded in blue, with potential $V_{det} = V_{det}^{DC} + V_{det}^{AC}$. The deflection gate $G_{def}$ is shaded in green with potential $V_{def}$ and the depletion gate $G_{dep}$ in yellow with potential $V_{dep}$. The gates are operated as for the velocity measurement, with $G_{dep}$ being used to suppress the LO-phonon emission. We find this gate can reduce the emission in the longer path length to zero, as with the smaller previous devices. The total path lengths for this device are short path 5 $\mu$m, and long path 28 $\mu$m, with the time of flight path (ring length) being 20 $\mu$m.

To calculate the quantity of LO phonon emission in the 20 $\mu$m path we proceed as follows. We set the potential $V_{dep}$ such that there is a single LO-phonon emission between pump and detector. As discussed, this shows up in our detector energy maps as a well defined arrival of current 36 meV below the original pumping energy. In Fig. 4.3(a) we plot the detector barrier energy map with a single LO-phonon emission visible. . In (b) we plot a similar map with no LO phonons present for comparison.

To be quantitative, in Fig. 4.3(c) we take a horizontal scan of the map in the position marked by the black line in the colourmaps (a) and (b), at $V_{G2} = -0.44$ V. This shows how the detector transmitted current $I_d$ varies as we open the detector by changing $V_{det}^{DC}$ (note

that for this measurement $V_{det}^{AC} = 0$). For the scan of the long route (a), we see that $I_d$ opens up to the pumped current value $I_p$ in one transition at -0.58 V. We introduce an additional ammeter on the pump source lead (see Fig. 4.2) which measures the pumped current $I_p$, so that we can check the fraction of $I_p$ constituting $I_d$ (we invert the sign of $I_p$). When there is LO-phonon emission present, we recover the pumped current $I_p$ in two steps, as shown in Fig. 4.3(c). We can also see a smaller transition of current approximately 10 mV below the pumping energy, marked with a letter A in Fig. 4.3(a). The origin of the energy loss of this fraction of current is unknown. One idea could be that this current is changing path slightly underneath the detector barrier and so arriving later, which would be recorded as a lower energy in the detector (because we sweep $V_{det}^{DC}$ from high to low). It has been recorded in samples from before the development of the depletion gate. Nevertheless, it does not perturb our measurement, because we record the fraction arriving at the LO-phonon energy, ignoring transitions happening between this point and the pumping energy.

We take the fraction of current arriving at the LO phonon emission of the pumped current $I_p$, which is measured by another ammeter on the pump source lead. This defines a "survival" fraction, $P_0^{l,s}$ for each of the long ($l$) and short ($s$) paths from pump to detector. This is the probability that an electron will traverse the path length from pump to detector without emitting an LO phonon.

We wish to convert this survival to a rate of emission so we may compare with scattering theory. As was detailed in the previous chapter, we can measure the time of flight around the ring. But we will need to separate the contribution to $P_0^l$ from the ring and from the rest of the path length. To do this, we compare the survival fraction along the short route, $P_0^s$ with the long route, $P_0^l$, for the same pumping energy. This is done by selecting $V_{def}$ values where velocity $v$ is not varying with $V_{def}$ (see Fig. 3.7). This is shown in Fig. 4.3(c), with the arrow denoting $P_0^{l,s}$ marked at the location of $V_{det}$ where the fraction is taken.

We then measure the velocity in an identical method to that detailed in Ch. 3. We find the velocity values to be very comparable in this device, with $4 < v < 12 \times 10^5$ m/s. We

calculate the survival fraction for the ring as $P_0 = P_0^l/P_0^s$, and convert to a rate of emission as $\Gamma_{LO} = -v/L\ln(\mathrm{P}_0)$ with $L$ the path length ($20\mu$m). As with the velocity measurements of the last chapter, we use the LO phonon emission to calibrate the detector barrier, finding $1mV_{det}^{DC} = 2meV = 1.45mV_{G2}$. In the next section we apply this method to explore the dependencies of the LO emission.

## 4.3 Potential profile dependence of the LO phonon emission

We first proceed by changing the energy of the pumped electrons, by changing the potential barrier height $V_{G2}$. We plot the survival $P_0$ as a function of energy in Fig. 4.4(a). Additionally, in Fig. 4.4(a) we also plot the survival $P_0$ as a function of $V_{dep}$. This shows us a very clear energy and depletion dependence. We see that emission of a LO phonon has a stronger dependence on the electron energy than the depletion, but the effects are not greatly mismatched. In Fig. 4.4(b) we provide the equivalent data set when converted to a rate of emission $\Gamma_{LO}$. In Fig. 4.4(c) we take the case of $V_{dep} = -0.25$ V and measure the emission as a function of field $B$ (the measurements of (a)-(b) are performed at 11 T).

Now we are in a position to combine these trends quantitatively. From the velocity, we derive a potential profile form for each $V_{dep}$ value, using the empirical local electric field method of Sec. 3.4.1 (we note also that this sample, more so than those previously studied, does not show $v^2$ vs $E$ correspondence at low energy). This is plotted in Fig. 4.5, with $\phi$ the potential, found by varying the electron energy $E$.

As with the results of the last chapter, we take $(\phi, y) = (0, 0)$ as the highest attainable pumping energy. The error is cumulative based on the pairwise calculation of $y$, as shown in the inset. We omit the error from the main plot for clarity. This plot shows us two important results. Firstly, the potential profile changes with $V_{dep}$. We would expect this as $\mathrm{G_{dep}}$ is simply a Schottky barrier and as we increase the potential we move the gate closer

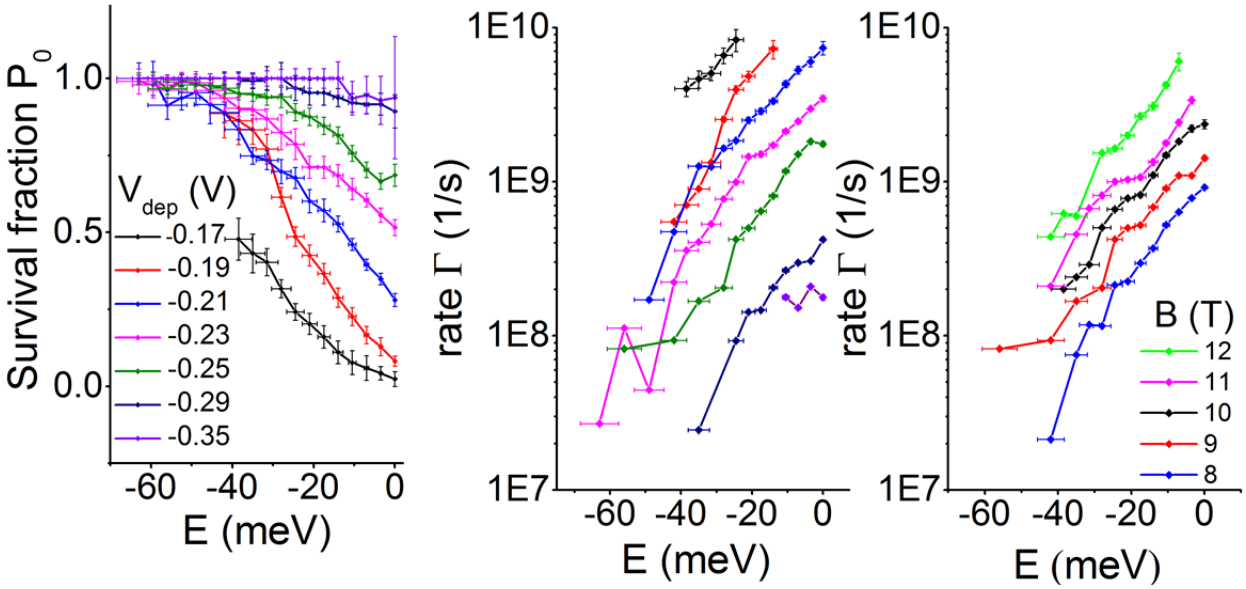


Figure 4.4: (a) Survival fraction $P_0 = P_0^s/P_0^l$ as a function of energy and depletion gate voltage $V_{dep}$. (b) Rate of LO-mode phonon emission as a function of energy and depletion gate voltage (colour scheme as (a)). (c) Rate as a function of energy with magnetic field, for the case $V_{dep} = -0.25V$.

to pinch-off. The fact that we measure this change is proof that our hot electrons propagate underneath $G_{dep}$ as we intended. The second is that the observed emission rate dependence with $V_{dep}$ is due to the potential profile shape. This confirms a Fermi's Golden Rule (FGR) type approach to be valid, as state overlap will depend on the curvature of the profile. We will develop this argument quantitatively next.

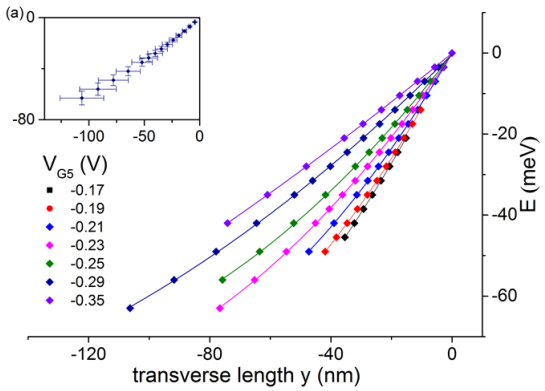


Figure 4.5: Mapping of the potential profile $\phi$, as a function of $V_{dep}$. We see the shift in the bottom of the profile with increasing $V_{dep}$ (more negative voltage) matches the action of a Schottky barrier. Inset: the error, cumulative, for the case $V_{dep} = -0.25$V, omitted from the main plot for clarity.

## 4.4 Cross-checks

Before we link our rate variation with FGR, we must perform two crosschecks. These are that we see that we have an accurate average rate of emission, and that we match the path length taken for the velocity with the path length taken to extract $P_0$. Both of these concerns address the question of where the phonons are emitted, which we cannot overlook. So far, we have a $3\mu$m discrepancy in the paths we use for $v$ and $P_0$. This is because, for $v$, we do not include the contribution from the length along the gate $G_{dep}$ (see Fig. 3.7). However, in calculating $P_0^l$ we are including this path length, as we use the difference in length between the long and short paths which includes the gate length along $G_{def}$. To balance these, we must measure the dependence of $P_0$ with $V_{def}$, which we plot in Fig. 4.6.

In this plot we take the case of $V_{dep} = -0.21$ V at $B = 11$ T and measure $P_0^l$ for varying $V_{def}$. We see that, to within our resolution, the curves are in the same position, showing LO emission is not dependent on $V_{def}$. This is what we would expect. When calculating long and short routes, we take values of $V_{def}$ where the arrival time is not varying with $V_{def}$. This means the contribution to the velocity from the potential due to $V_{def}$ is vanishingly small. Hence, the electron travels significantly faster in this region around the gate, and it becomes much less likely that an emission will take place within the gate length. So, in calculating

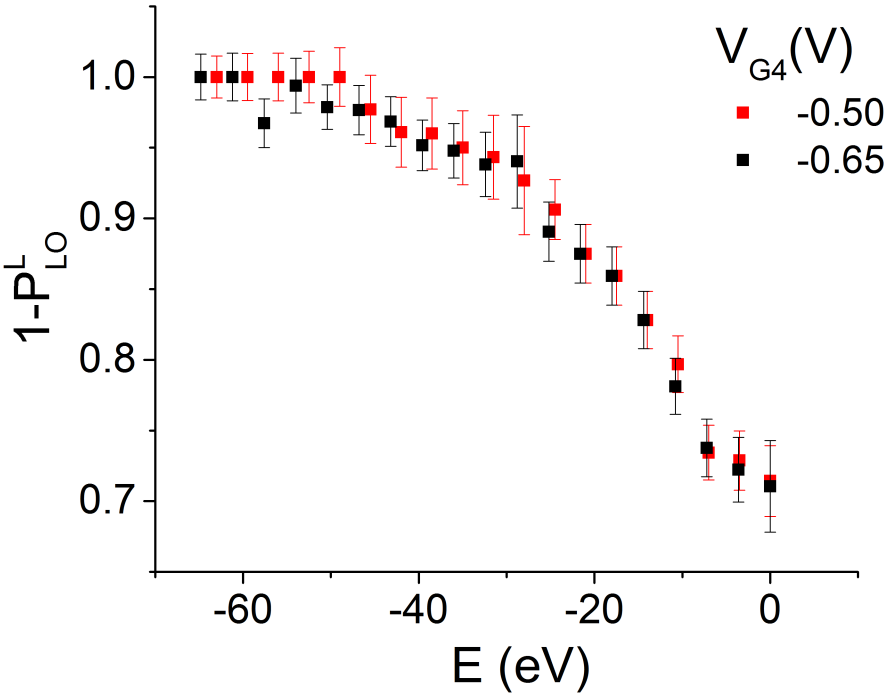


Figure 4.6: The survival fraction in the ring, $P_0$, as a function of energy for the case of $V_{dep} = -0.21$ V at $B = 11$ T. As we change $V_{def}$ between a value just enough to deflect the electrons to the long route (-0.5 V) and the value used for the long route measurements (-0.65 V), there is no significant change to the form of the survival, indicating there is no contribution from the length along $G_{def}$ because the velocity is much higher in this region than the ring.

$P_0$ in the previous section, we can assume we have not included a contribution from path along the gate length and our path lengths with which we calculate $\Gamma_{LO}$ are equivalent.

To address the first concern, that we measure the average rate, we consider the path itself. As stated in the previous chapter, we take our path lengths to be the lithographically defined lengths, but we have no information about the actual path taken by the electron. This adds the same systematic uncertainty to the $v$ and $P_0$ which again does not stop us from drawing conclusions. However, $v$ is an average taken around the ring, and so we must make sure that $P_0$ is too. We could imagine that there may be a small section of the gate length of $G_{dep}$ in the ring that did not deplete effectively, and hence there would be a much larger rate of emission ($\Gamma_{LO}$) for this short length. This would not perturb our measurement of $v$, because the velocity in this region would be very fast (an equivalent argument to the contribution of $V_{def}$), but it would perturb $P_0$ greatly, as we only require a small variation in $\Gamma_{LO}$ to make a measurable contribution to the current measured at the emitted stage. Hence, error in $v$ would mostly arise from the potential profile being shallower than that measured, and error in $P_0$ would mostly arise by the potential profile being shaper than measured.

We can check if our hypothetical situation is actually occurring. We measure the arrival time distribution (ATD, described in Sec. 2.5), $dI_d/d\Delta t_d$. As we measured in Fig. 2.6, this is normally a Gaussian with FWHM $\sim$ 14 ps. If we compare the ATD of current that has emitted a LO phonon, we should find a continuous distribution to the ATD because the LO emission event can take place anywhere in the path length. We compare the ATD for the case of no emission and one emission in Fig. 4.7.

In this figure, our horizontal axis plots the time domain $\Delta t_d$ and the vertical axis the magnitude of the ATD. In black, we plot the trace for $V_{G2} = -0.4$ V at $V_{def} = -0.29$V, $B = 11$ T and not undergoing any LO phonon emission. This looks like a Gaussian distribution as we found from in the work of Ch. 2. In red, we plot the equivalent ATD for the current emitting 1 LO phonon (from the same pumping energy). This is noisier because there is less current emitting a phonon, and so this ATD is close to our noise floor. Hence,

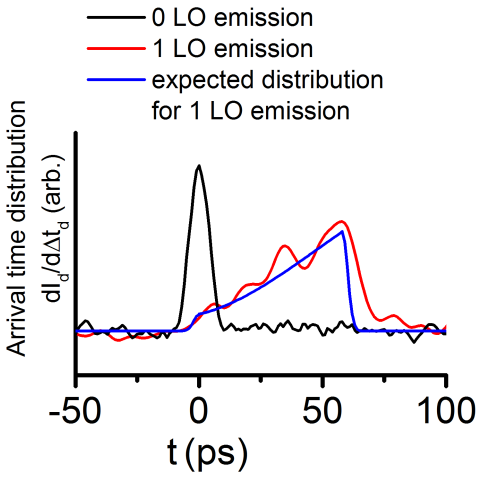


Figure 4.7: Comparison of the arrival time distributions (ATD) between each case of no LO-phonon emission (black), and one emission (red). We see that in the case of one LO-phonon emission, the distribution is much broader, and maps to an expected cumulative distribution (blue), if scattering events were taking place throughout the ring.

oscillations in this ATD are attributed to noise only. In blue, we plot the expected distribution $A(x,t)$, for electrons emitting LO-phonons throughout the ring length. This has been derived numerically by our collaborator C. Emary according to a method based on Emary et al. [95], with the full method to be published elsewhere. This is given by

$$A_{LO}(x,t) = \frac{v^1\Gamma}{2\left(v^0-v^1\right)}\exp\left(\frac{\Gamma}{2\left(v^0-v^1\right)^2}\left(w^2\Gamma-2\left(v^0-v^1\right)\left(x-v^1t\right)\right)\right) \\ \times\left(\mathrm{erf}\left(\frac{w^2\Gamma-\left(v^0-v^1\right)\left(x-v^0t\right)}{\sqrt{2}w\left(v^0-v^1\right)}\right)-\mathrm{erf}\left(\frac{w^2\Gamma-\left(v^0-v^1\right)\left(x-v^1t\right)}{\sqrt{2}w\left(v^0-v^1\right)}\right)\right) \tag{4.1}$$

with $v^{0(1)}$ the velocity of the electron having emitted no LO-phonons (0) and 1-LO phonon (1); $\Gamma$ the rate of phonon emission, extracted from the data; $w$ the FWHM of the Gaussian distribution describing the (as-pumped) electron wavepacket; $x$ the distance from the pump (here, this is the long route path length of 28 $\mu$m). For the given pumping and profile conditions used here, we evaluate $A_{LO}(x,t)$ with parameters $v^0 = 11.6\times10^4$ m/s, $v^1 = 8.7\times10^4$ m/s, $\Gamma = 6.3\times10^9$ /s, $w = v^0\times 1$ ps $\sim 10$ $ps$.

This plot shows us there is approximately continuous emission around the ring. If the

phonon was emitted at the end of the path, we expect the current to arrive at the same time to the detector, which we see. When the LO-phonon is emitted, we expect that its velocity would decrease by $\Delta v \sim 3.6 \times 10^5$ m/s and so it would arrive $\sim$ 56ps later, if the electron emitted the phonon at the start of the ring, which we observe. The distribution accumulates and is non-zero throughout the ring length. The ATD has no clear substructure implying excess emission along the path length. This also implies the potential profile does not change much around the ring, and so $v$ is reasonably an average value. We plot in blue the expected distribution, which is based on a cumulative distribution in length. It could also be calculated by solving the partial differential equation $(\partial/\partial t)(\rho^{(1)}) + v(\partial/\partial x)(\rho^{(1)}) = \Gamma(x)\rho^{(0)}$, where $v$ is the initial velocity and $\rho^{(0,1)}$ is the probability distribution in the non-emitted (0) or single-emitted (1) state. This expression assumes rate is dependent on length $x$, with $x$ the electron propagation direction [95].

So we may trust that there is agreement between measurement of $v$ and $P_0$, and they both represent the averages around the ring. This gives us the most accurate data to fit to the model which we do next.

## 4.5 A quantitative model for phonon emission

We collaborate with Dr. Clive Emary of Newcastle University, and fit our data to his previously studied scattering theory [95]. Qualitatively the scattering proceeds as follows. We employ Fermi's Golden Rule (FGR) to dictate the scattering rate. This rule is very general and not isolated to our system. It states that the rate of transition between any two states is proportional to the overlap of the wavefunctions in each state. We define the rate of transition $\Gamma$ between an initial state $i$ and a final state $f$

$$\Gamma_{if} = |M|^2 \rho_f = \int \Psi_f^* V \Psi_i dt' \tag{4.2}$$

where $M$ is a matrix element that details the coupling between states $i$ and $f$ which are

described with a wavefunction $\Psi_{i,f}$, $\rho_f$ the density of final states and $V$ the perturbation giving the interaction between states $i$ and $f$. This is derived from time dependent perturbation theory [97, 98].

Application of FGR to the case of phonon emission from electrons in a 2DEG, or bulk semiconductor, have been considered in detail [88, 96–100]. Specifically, for the hot electron in edge state case, we follow the derivation of rate by Emary, which we summarise below, and is based on the previous referenced works, which he published in Ref. [95]. First, we consider the form of the Hamiltonian for the electron propagating in the edge state. This is derived from the effective mass approximation as [52]

$$H = \frac{1}{2m^*}\left(i\hbar\nabla - e\mathbf{A}\right)^2 + U(y) \tag{4.3}$$

with $m^*$ the effective mass ($0.067m_e$ in GaAs), $-i\hbar\nabla$ the canonical momentum and $\mathbf{A}$ the vector potential. $U(y)$ is the potential confinement in the transverse ($y$) direction, which we have measured in the previous chapter to have a parabolic form: $U(y) = \frac{1}{2}m^*\omega_y^2 y^2$. This Hamiltonian describes a quantum harmonic oscillator, and has solutions that are plane waves propagating in $x$ with eigenvalues that describe the electron energy

$$E_{nk} = \hbar\Omega\left(n + \frac{1}{2} + \frac{1}{2}\left(\frac{\omega_y y_c(k)}{\omega_c l_\Omega}\right)^2\right) \tag{4.4}$$

which has a form similar to the quantum harmonic oscillator. $l_\Omega$ is a wavefunction characteristic width $l_\Omega = \sqrt{\frac{\hbar}{m^*\Omega}}$, where $\Omega = \sqrt{\omega_y^2 + \omega_c^2}$ (and is scarcely different from the magnetic length $l_b = \sqrt{\frac{\hbar}{eB}}$ in our case as $\omega_c >> \omega_y$). $y_c$ is a guiding centre about which the electron precesses according to the $\mathbf{E}\times\mathbf{B}$ drift, as $y_c = \frac{\omega_c^2\hbar k}{\Omega^2 eB}$.

To develop the electron - phonon interaction we use the Fröhlich Hamiltonian [101]. This states that we may break down the total Hamiltonian for the electron - phonon system into electron, phonon and coupling terms: $H = H_{el} + H_{ph} + H_{el-ph}$. We have considered the electron wavefunction. The phonon wavefunction can be considered very similarly, because

although it is a boson, we only deal with single (or sequential) phonon emission as that is all we observe in this system. Hence, the phonons are also described as plane waves, with their energies determined by the momentum change $\delta k$ [102]. We further constrain ourselves to the LO mode, so our emission energy is limited to 36 meV. For the interaction, we employ FGR, deriving

$$H_{el-ph} = \sum_{nn'} \sum_{kk'} \sum_{\mathbf{q}} M_{n'n}^{k'k}(\mathbf{q}) c_{n'k'}^{\dagger} c_{nk} \left( a_{-\mathbf{q}}^{\dagger} + a_{\mathbf{q}} \right) \tag{4.5}$$

$c$ being the annihilation operator for electrons in state $nk$, $a$ annihilation for phonons governed by the coupling matrix element $M$, with $\mathbf{q}$ the possible momentum change, $k(k')$ the initial (final) $k$-values and $n(n')$ the initial (final) $n$ quantum number values. We can impose limits on the acceptable range of $k$ and $\mathbf{q}$ allowed, because we know that only a single, LO-mode phonon emission is seen (36 meV) and the hot electron energy $E$ is much greater than the phonon energy (otherwise we could not detect the electron).

We then write our coupling as

$$M(\mathbf{q}) = \frac{4\pi\alpha\hbar \left(\hbar\omega_{LO}\right)^{3/2}}{\sqrt{V}\sqrt{2m^*}|\mathbf{q}|} \tag{4.6}$$

with $\alpha$ a coupling constant and $V$ the volume.

Emary [95] solved this numerically to derive a rate of LO-mode emission

$$\Gamma_{n'n}(E) = \frac{\alpha\Omega\omega_{LO}}{2\pi\omega_y} \sqrt{\frac{\hbar\omega_{LO}}{\Delta_{n'}}} \Theta\left(\Delta_{n'}\right) I_{n'n}\left(\delta_g\right) \tag{4.7}$$

where $\Delta_{n'} = E - \hbar\Omega(n' + 1/2) - \hbar\omega_{LO}$ is the electron energy after emission of an LO-phonon, $\Theta$ is the Heaviside step function and $I_{n'n}$ an integral governing the change in position in guide centre $\delta_G = \left(y_G - y_G'\right)/l_\Omega$. The numeric analysis shows the rate to be strongly a function of energy and field, as we have experimentally seen.

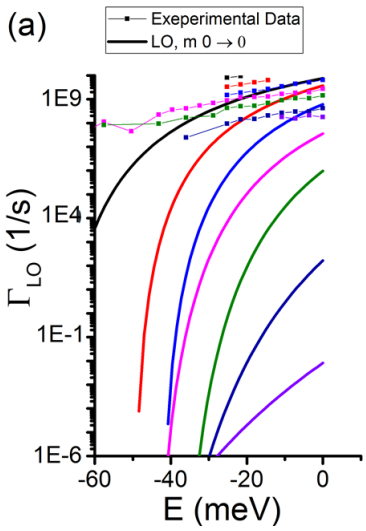


Figure 4.8: Comparison between the measured rates, points, and the expected rate for LO-mode emission within the same zeroth Landau Level, solid line.

### 4.5.1 Results of the model

Now we use the above derived rate to calculate the expected rate of LO-phonon emission for our experimental situation. We calculate the expected rate of LO-emission within the zeroth Landau Level. So, our parameters are as follows. We take $n' = n = 0$, $\omega_y = 1 - 4$ meV, depending on which $V_{dep}$ value we are using and $B = 11$ T. Fig. 4.8 shows the result of the model, as a function of energy and depletion ($\omega_y$). Here, the points show the rates extracted from the data, and the lines the rates calculated from the model.

We see poor agreement in our first approximation. The calculated rate is several orders of magnitude lower than the measured rate across all the measured points. First, we consider if our rate is erroneous. Recall that our reported rate is based on an average velocity and average potential profile shape around the ring. We note that, in deriving the rate, the velocity term is more sensitive to velocities faster than the average, whilst the survival fraction is more sensitive to velocities slower than the average. So, is it possible that our measured velocity is too high (weighted by some small anomalously sharp curvature), or our survival is too low (weighted by some small anomalously shallow curvature)? On first inspection we answer no, based upon Fig. 4.6 and Fig. 4.7. These plots show us that to

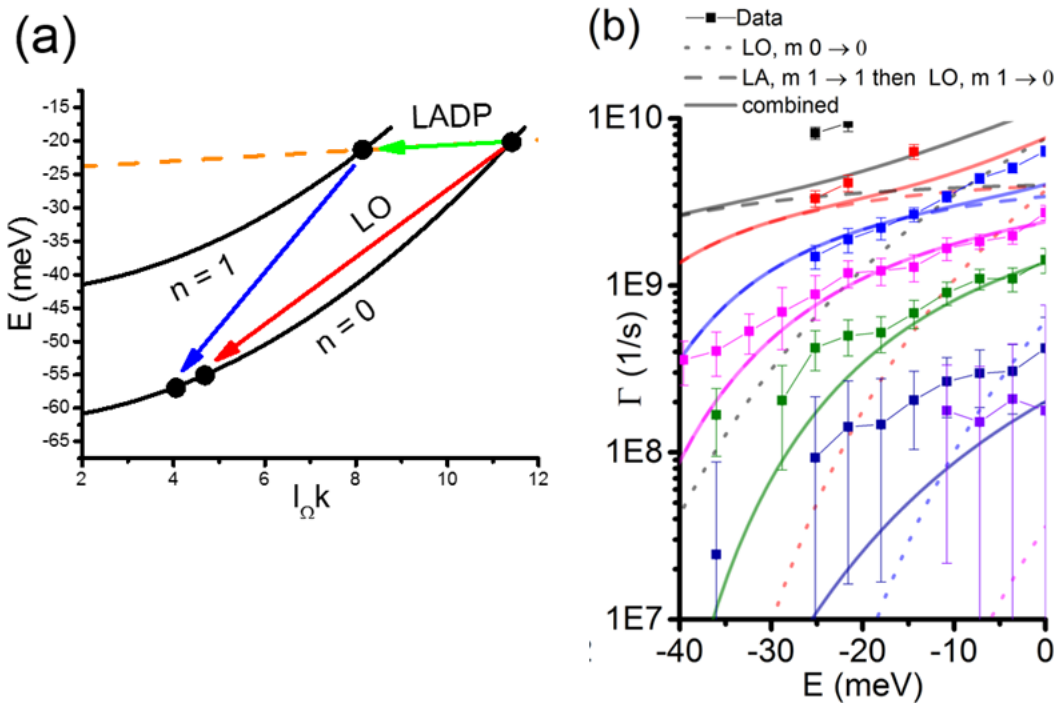


Figure 4.9: (a) Plot of the profiles measured for the case of $V_{dep} = -0.25$ V (black), and spatial shift expected for each mode: red arrow, intra-level LO-phonon scattering, blue, inter-level LO-phonon scattering, and green, LADP-mode scattering. As the LADP mode is a continuous emission process, the dashed yellow line indicates the maximum possible energy loss. The length scale $l_\Omega k$ is equivalent to units of the magnetic length. (b) The measured rates and expected rates for the combined process of the two modes plotted in (a) (solid lines), with their constituent processes LADP (dashed) and LO-mode only (dotted).

within our measurement resolution emission of phonons is uniform across the ring length and do not occur in the length alongside $G_{def}$. Invoking disorder to match the measured rate seems inappropriate, as we would require the velocity to be orders of magnitude less for some section of ring length, or the ring length to be many microns longer than the lithographic length.

Instead, we turn to our expression for the rate, and find we can explain the observations if we allow inter-Landau Level scattering to occur: we let $n \neq n'$ (also found to be possible in [92]). This argument can be considered from the overlap alone. Fig. 4.9(a) plots our situation, for the case of $V_{dep} = -0.25$V.

In black, we plot the measured curvature for the zeroth Landau Level ($n = 0$), and

calculate the position of the first ($n = 1$) case as per Ref. [50]. The red arrow denotes the intuitive intra-level emission of a single LO-phonon. We notice that, for a given final energy ($E - 36$meV), the $n = 1$ state has a greater overlap than the $n = 0$ state. A high rate of scattering could occur if electrons could easily transition to the next Landau level. One way of this occurring is via a longitudinal acoustic via deformation potential (LADP) mode phonon [88, 92, 95, 99]. This is a continuous emission process, so the yellow dashed line on Fig. 4.9(a) indicates the maximum energy loss possible, and is a few meV. Then, once in the $n = 1$ state, the overlap with a state in $n = 0$ at an energy $\sim 36$ meV below the pumped energy is significant; this is why perhaps we do not see any current arriving at the detector in this state (which would have a different velocity and so present as a separate ATD). The end distributions, shown as the black filled circles in the $n = 0$ state, are at most centred less than 4 nm apart, and therefore only present as one distribution in the detector as the energy broadening of the wavepacket is approximately the same size as the energy difference between these two states in the $n = 0$ case (we discuss this broadening in Ch. 5).

In Fig. 4.9(b) we plot again the measured rate data, but with the two possible modes and combined rate. The dotted lines show $n = 0 \rightarrow 0$ LO-mode emission, the dashed lines show LADP + LO - mode, and the solid lines show the combined rate of both. We see the combined rate is much closer to the measured rate, at least now at the same order of magnitude. Further, there is a qualitative agreement at low $V_{dep}$ in the turning point seen at the crossover between the LO-mode dominated and LADP-mode dominated pumping energies.

We need to be careful about invoking LADP emission, because if this mode is permitted and observed in our system, then we should observe other modes too. An important other mode to consider is LADP emission alone - which should happen at all of our measured points. Also there are small but finite contributions from other acoustic modes, and up-scattering too, which has never been observed. Observation of these processes may require better energy resolution in the detector than we presently have.

We have characterised the mechanism by which electrons lose energy in our system. Importantly for development of a protected state, we have found a way to suppress this emission, by increasing the scattering length from $\sim 1\mu$m to 1 mm, making fabrication of devices with a long path length possible, opening up many possibilities. In the next chapter we return to our concept of the arrival time distribution. We have been implicitly using it here, but next we shall explore quantitatively what constitutes it and how we can possibly tune it.

# Chapter 5

# Study of the Electron Wavepacket

## 5.0 Introduction

We have studied two important properties of hot electrons as produced by our electron pump, namely their velocity as they propagate in edge states, and their modes of relaxation. Throughout this work, and that of the oscilloscope in Ch. 2, we have subtly used the concept of the electron wavepacket. The temporal wavepacket was used to establish the SES scheme bandwidth. We implicitly use the concept of wavepacket whenever we use a derivative of the current $I_d$, which underlies our LO-phonon counting technique. Now we seek to measure its size explicitly, and confirm the important relationship that the wavepacket size is determined by the pumping parameters. That allows us to begin moving towards a tunable wavepacket size, which could make interferometry easier. Besides, if we are to construct an interferometer, or improve our SES scheme bandwidth, we shall need to know the temporal size of the wavepacket.

We proceed by establishing the expected form of the wavepacket, and present measurements of the temporal and energy - domain sizes that confirm the relationship between the wavepacket size and pump action. This was published in PSSb in 2016. We show that this relationship is not fully explored, with some trends as yet unexplained.

Associated publication: **Time-resolved single-electron wave packet detection**

M. Kataoka, J. D. Fletcher, N. Johnson

**Physica Status Solidi B 254** 1521 *2016*

goo.gl/6ZPNby

*N.J. and J. D. F. performed the measurements and analysis; M.K. wrote the paper and devised the probability density approach.*

## 5.1 The measured wavepacket

We must first define our concept of wavepacket. For our system, there are two measurable quantities which we call the "measured arrival time distribution (mATD)" and the "measured arrival energy distribution (mAED)". Our previous mentions of electron arrival time distribution are formally referring to this measured distribution, the mATD. These are the range in which the transmission across the detector barrier, $T$, changes from 0 to 1 in each measurement domain of our detector barrier. The transmission across the detector barrier is measured as the fraction of the pumped current that is transmitted for a given potential $(V_{det}^{DC} + V_{det}^{AC})$:

$$T = \frac{I_d}{I_p} = \frac{I_d}{ef} \tag{5.1}$$

And so the mATD is measurable as the region in which $\frac{dT}{dt}$ is non-zero, and equivalently for the mAED $\frac{dT}{dE}$. Fig. 5.1 illustrates the concept. We take a square wave as the form of $V_{det}^{AC}$, which has a sharp step in time (Fig. 5.1(a)). The close up of the step (b) in the waveform shows the sharpest temporal change in $V_{det}^{AC}$, and this allows us to easily measure the wavepacket as the horizontal derivative of the step $dI_d/d\Delta t_d$ (c). We find that this mATD is fitted well by a Gaussian fit (red line), and we take the Full Width at Half Maximum (FWHM), $w_t$, to deduce the wavepacket size. We also observe a similar Gaussian form in the energy domain. In the example trace (c), $w_t \approx 10$ ps. Although we have defined

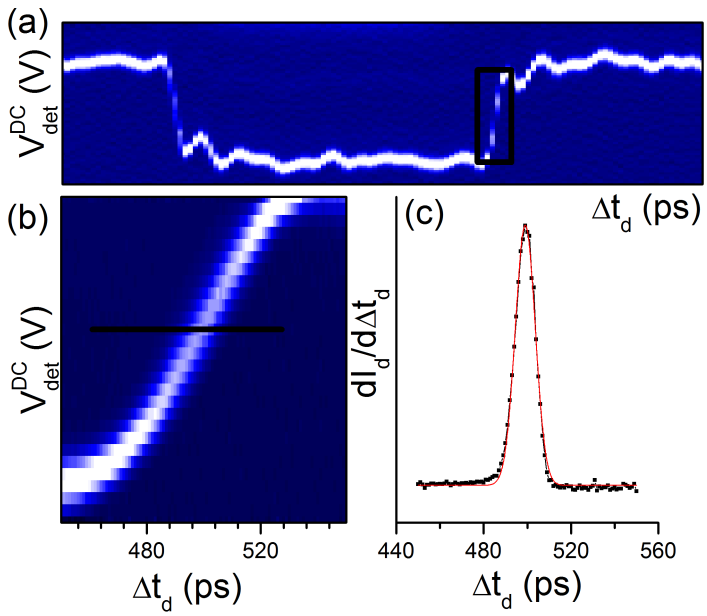


Figure 5.1: (a) A familiar square wave trace taken by using electrons to sample the square waveform $V_{det}^{AC}$ on the detector barrier. (b) Close up of boxed region of (a) shows the sharp riser we use to measure the temporal wavepacket. (c) Cut through as marked in (b) gives the wavepacket in the temporal domain. We define this as the measured arrival time distribution (mATD), with a Gaussian fit (red line).

the wavepacket at the sharpest rate of change in time and potential of the detector barrier, the concept is more general, and that any cut across the detector barrier, that includes a transmission range from 0 to 1, defines a mATD or mAED. We shall show why we only use the sharpest barrier points. Fletcher [8] was among the first to notice that $w_t$ could vary, even in regions where the barrier transmission was likely constant, and concluded the measured wavepacket mATD contains some information about the electron wavepacket (also discussed by Waldie [67]).

## 5.2 Physics of the Wavepacket

We understand the mATD to be the convolution of the electron wavefunction probability density $\rho(E,t)$ with the detector barrier transmission ($T(E,t) \propto dV_{det}^{AC}/dt$) [103].

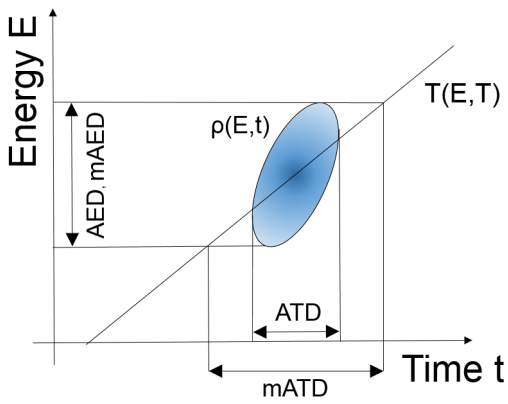


Figure 5.2: Sketch of $(E,t)$-space showing the electron wavepacket distribution $\rho(E,t)$ and its projections to each measurement axis defining the ATD and AED. The barrier transmission function is shown as a line $T(E,t)$ that is convoluted with $\rho(E,t)$ to give us the measured projections of the wavepacket mATD and mAED. Note that this is not the most general form of the convolution, but is drawn to match the following experimental results.

$$\frac{I_d}{ef} = \rho(E,t) * T(E,t) = \int \rho(t)T(t'-t)dt \tag{5.2}$$

We have the equivalent expression for the measured AED (mAED):

$$\frac{I_d}{ef} = \rho(E,t) * T(E,t) = \int \rho(E)T(E'-E)dE \tag{5.3}$$

We are assuming that $\rho(E,t)$ is separable as $\rho(E)\rho(t)$, which matches the experimental results to first order. Fig. 5.2 shows a sketch of the convolution. It is clear that the mATD $\equiv$ ATD in the limit that the detector barrier becomes an infinitely sharp riser (i.e. $V_{det}^{AC}$ is a perfect square wave).

The quantum mechanics of a free particle allows us to define an equivalent definition of an electron wavepacket as the envelope of the probability amplitude of the wave function, which is equivalent to our $\rho(E,t)$. This is usually referred to as the (electron) Arrival Time Distribution (ATD). We take an initial wavepacket to be Gaussian with form $\Psi(x,t) = \Psi(x,0) = Ae^{-ax^2}$, as plotted in Fig. 5.3 [104]. For a free particle moving in one dimension (such as in our edge state), this wavepacket will evolve according to the time dependent

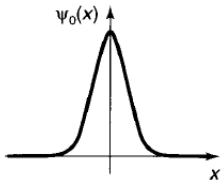


Figure 5.3: The solution to the free particle Schrödinger equation is a Gaussian wavepacket. Taken from Griffiths [104].

Schrödinger equation

$$\left(-\frac{\hbar^2}{2m}\frac{\partial^2}{\partial x^2}+V\right)\Psi(x,t)=i\hbar\frac{d}{dt}\Psi(x,t) \tag{5.4}$$

which can be solved by separation of variables [104] and remains Gaussian in shape, spreading with time.

This looks similar to what we have measured in Fig. 5.1(c). However, it is important to note that the measured wavepacket is not the same as the electron wavepacket.

According to the definition of the free particle wavepacket, the form of $\rho(E,t)$ should be circular in $(E,t)$ space. However, we draw the electron wavepacket $\rho(E,t)$ as having some elliptical form, which is a smearing effect from the dynamic quantum dot in the pump. We expect that the ATD is determined by the time taken to tunnel over the exit barrier $G_2$, and the AED from the energy broadening of the state in the QD. However, when the QD confining potential profile is dynamic, then we can expect to introduce an energy smearing that is proportional to $dV_{G1}^{AC}/dt$, i.e. the rate of change of the QD confining potential [68,86]. This in turn will couple in to the time domain, as the form of the pump exit barrier changes as a function of energy (studied theoretically by Ryu [68]). We will measure this to confirm this is so in the next section.

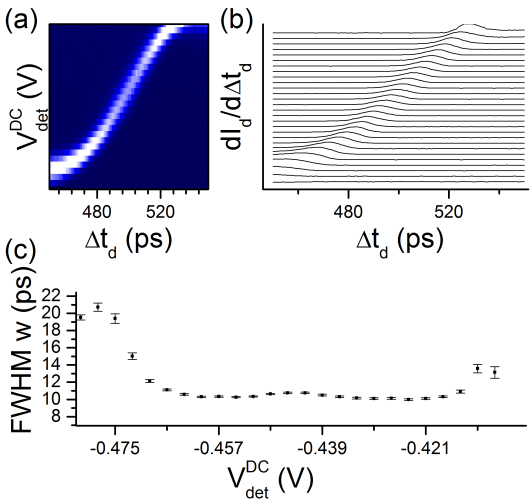


Figure 5.4: (a) As Fig. 5.1(b), we take only the sharp step to extract the mATD. (b) Plot of the derivative $\frac{dI_d}{d\Delta t_d}$ across the step. (c) The Full Width at Half Maximum (FWHM), $w_t$, for Gaussian fits to the traces in (b). The variation in $w_t$ tracks $\frac{dV_{det}^{AC}}{d\Delta t_d}$.

## 5.3 Measurements

In the discussion of measurements that follows, we utilise the detector barrier methods of Chapter 2. As we change the detector barrier potential such that transmission across the detector varies from 0 to 1, we recover the current trace of Fig. 5.1, the derivative of which in potential is the mAED, and in time, the mATD (AC barrier case). For this work we use a number of time of flight type samples, although all that is required is a detector barrier. We use only the short route, and all other gates are held constant. Multiple samples were used, with the observations and conclusions presented here common to all. In this first section, we describe the mechanics of measuring the mATD. The same method is applied to the mAED, and is a bit more straightforward to implement.

We start by applying a square wave as the form of $V_{det}^{AC}$, in addition to the offset $V_{det}^{DC}$. We proceed to use the detector in the SES scheme, by varying the DC level to sample the square waveform, as described in Ch. 2. The time delay between the pump drive $V_{G1}^{AC}$ and detector waveform $V_{det}^{AC}$, $\Delta t_d$, is swept as a function of $V_{det}^{DC}$ (as per the single electron sampling scheme but with the swept axis and stationary axis switched). We have approximately 0.5 mV and 1 ps resolution of these parameters. A plot of the step in the waveform is shown in Fig. 5.4(a),

where we are plotting the horizontal derivative $dI_d/d\Delta t_d$ in the colourscale. In Fig. 5.4(b) we plot the derivative plotted in (a) with $\Delta t_d$ for each $V_{det}^{DC}$ (offset vertically), which plot the mATD. They all appear to be well approximated by a Gaussian fit, which is marked on the plot. We see they have different amplitudes and full width at half maximum (FWHM) $w_t$. As we move between traces in this plot, we can expect that the form of $\rho(E,t)$ is unchanging (in the limit that the DC potential of the detector barrier does not have coupling or crosstalk to the pump), and so the variation in $w_t$ is a measurement of the change in $T(E,t)$ across the waveform. This highlights why it is not necessarily straightforward to extract $\rho(E,t)$ or the electron ATD. Finite bandwidth in the AWG and measurement lines means that the rate of change from upper to lower step will always give a less than vertical slope, giving a finite $dV_{det}^{AC}/d\Delta t_d$. We see the form of $T(E,t)$ changes but we cannot extract $\rho(E,t)$ yet. We note that we should be seeking to minimise the contribution from $T(E,t)$, i.e. maximise $dV_{det}^{AC}/d\Delta t_d$.

Fig. 5.4(c) shows a plot of FWHM $w_t$ against $V_{det}^{DC}$, extracted from the Gaussian fits to Fig. 5.4(b). To the sides of the plot, we know the waveform is at its turning points, and $T(E,t)$ becomes flat in time, giving a large $w_t$. As we move into the step of the waveform, $w_t$ quickly drops to about 10 ps. It is then seen to rise again in the middle, before dropping again to the minimum value. To understand this trace we need to examine how it changes with amplitude of the step $V_{det}^{AC}$. This is plotted in Fig. 5.5.

Here, we plot the equivalent trace as shown in Fig. 5.4(c), but at different peak-to-peak amplitudes, $V_{pk}$, of the waveform $V_{det}^{AC}$. Note that the horizontal axis is the DC offset $V_{det}^{DC}$, which is effectively shifting the pumped electron energy through the full amplitude of $V_{det}^{AC}$. We see that as we increase the amplitude, the traces settle to a single common minimum of $w_t \sim 8$ ps, and have the same characteristic shape. Where the amplitude is too small, e.g. $V_{pk} = 0.5$V, we see that we do not reach the minimum value of 8 ps, and this may be because $T(E,t)$ has weak time dependence (the step is very broad) and so the mATD is dominated by $T(E,t)$. By seeing a common value for the minimum $w_t$ appear as we increase $V_{pk}$, we

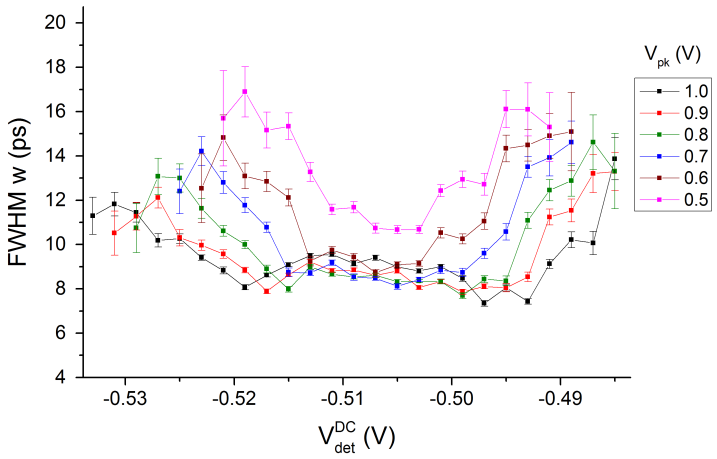


Figure 5.5: Traces of the FWHM $w_t$ across the step in the square waveform $V_{det}^{AC}$, for different amplitudes of $V_{det}^{AC}$, with peak-to-peak voltage $V_{pk}$.

assert this must be a value of $w_t$ dominated by $\rho(E,t)$ (we have checked that the slope of the step actually increases, so this is not some bandwidth limitation), and this is the value we should use to extract the ATD. The rise in $w_t$ in the middle of the step is harder to explain; perhaps this is because the sharp riser causes backaction on the pump. We select the point that gives this common minimum $w_t$ as our location in energy space ($V_{det}^{DC}$) and we will now vary $T(E,t)$ (amplitude of $V_{det}^{AC}$) to see how this minimum value changes.

To change the detector waveform amplitude, we can scale the waveform, using the AWG analogue peak-to-peak voltage output $V_{pk}$, or using software (i.e. define the waveform amplitude with less than the analogue output range), or change the number of AWG output points (output voltage values) that constitute the step (i.e. change the waveform shape). We use a combination of the first two methods, and keep the step as a defined single transition between two AWG points. We take our point in the transition chosen from above, and plot it as a function of $dV_{det}^{AC}/d\Delta t_d$ in Fig. 5.6(a), again, with the derivative $dI_d/d\Delta t_d$ in the colourscale. We see that as the amplitude decreases, the square wave shape is very shallow and the wavepacket becomes very broad, has smaller amplitude and becomes hard to define.

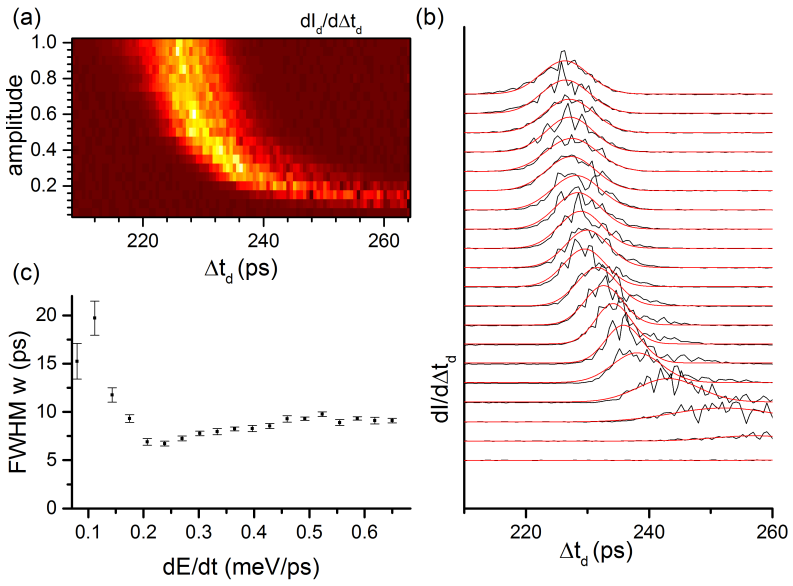


Figure 5.6: (a) Map of the change in a given part of the step of the detector waveform as a function of waveform amplitude ($\equiv T(E,t)$). (b) Plot of each line cut (black) showing the mATD. A Gaussian fit (red) is used to determine $w_t$. (c) Plot of the wavepacket $w_t$ with the amplitude of the detector waveform.

In Fig. 5.6(b) we plot each trace from (a) (black), and perform a Gaussian fit (red) to derive $w_t$. We plot each value of $w_t$ as a function of $T(E,t)$ in (c), which we can assign real units by evaluating the slope of the step. This trace clearly shows how the mATD varies with $T(E,t)$. When $T(E,t)$ is shallow, we record a large mATD, and as we increase the slope of $T(E,t)$ we see it drop to a minimum value, here $\sim$ 7 ps, and then begin to rise again. The minimum value implies the value where the mATD has mostly contribution from $\rho(E,t)$ (i.e. the mATD is closest in size to the ATD).

The minimum value of the mATD alone is not enough, as it only sets an upper bound to $\rho(E,t)$. We see that the value of $w_t$, and hence of our mATD, falls rapidly as we increase the slope. Then, it levels out, and slowly begins to increase in size again. The simple assumption made was that when $w_t$ is seen to be unchanging with $T(E,t)$, then the mATD is dominated by the contribution of $\rho(E,t)$ (refer to Fig. 5.2). Hence, in Fig. 5.6(c), we can identify the upper bound to the temporal size of the electron wavepacket to be $\sim$ 7 ps, as this is the turning point in the curve. However, we see that the value only saturates for a small range,

before increasing again, to the right of the plot. This can be explained in two ways. The first is that the nature of the wavepacket is being changed owing to backaction on the pump from the large amplitude square waveform. The second is that it arises from the energy broadening, which we explore next. We also must be careful that we cannot increase the amplitude arbitrarily, as we have a bandwidth imposed by the measurement lines. We are also limited by the ability of the AWG to produce the sharp steps we program, but this is incorporated into the above working definition of bandwidth.

Up to this point, we have neglected the assumption that we would expect that the energy and time domains are correlated, because the quantum dot is dynamic. This gives the elliptical shape sketched in Fig. 5.2. We have not yet established correlation is present, and so our next search is to see how the curve presented in Fig. 5.6(c) changes as we change the pumping parameters.

An unintended consequence of this measurement is that we mapped the linearity of the time delay control $\Delta t_d$, and found it to be not so linear. We must first understand the non-linearities in the time domain, as these have a big impact on our measurement of $w_t$.

### 5.3.1 AWG artefacts

The previous discussion has required that the time delay $\Delta t_d$ is swept linearly in the measurements. If it is not linear, we will likely record an artificially narrowed value of $w_t$. To set $\Delta t_d$, we use the AWG's (Tektronix 7122C) inbuilt I/Q modulation, which uses hardware and software to control the delay to 1 ps resolution. Delay can also be set by shifting the software voltage points relative to one another, but this control is much more coarse, only being accurate when we shift by an integer point (at maximum sampling rate this is 1/12 GS/s = 83.3 ps). When we began measurement we observed vertical lines in the colourmap plot of the waveform shape, as shown in Fig. 5.7(a). We see that these serve to bunch the signal so $w_t$ will appear very sharp. These jumps are fairly randomly placed throughout the delay time. In (b), we see that they will clearly affect the fit $w_t$, and make it artificially small.

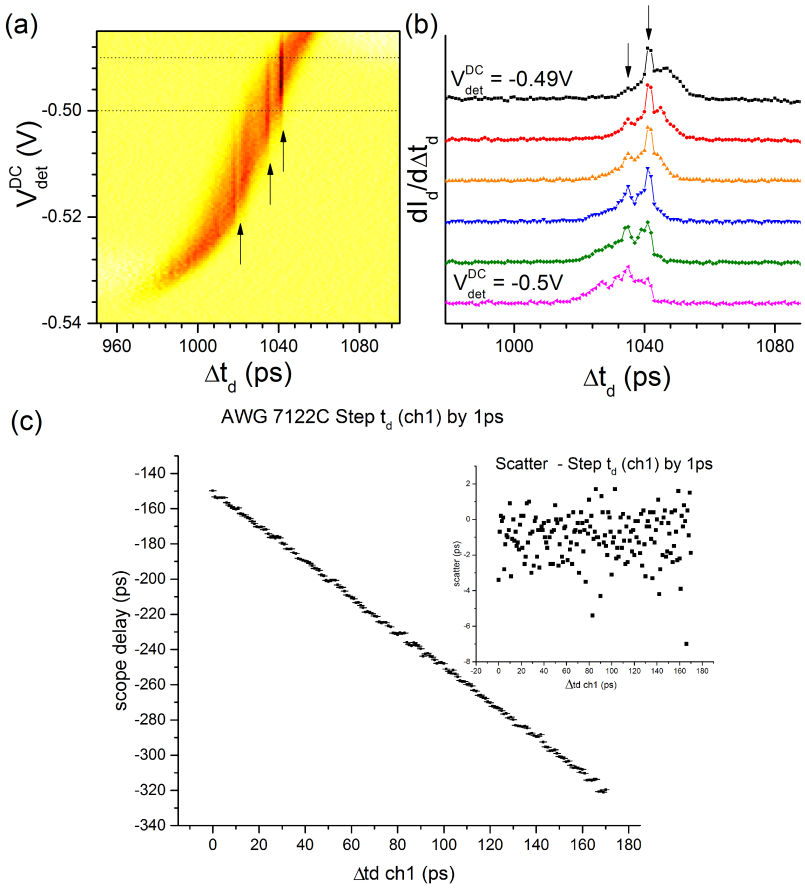


Figure 5.7: (a) Vertical lines, highlighted by arrows, appear in the square wave step when the delay control $\Delta t_d$ is not linear (compare to Fig. 5.4(a) for the clean case). (b) The mATD has a sharp peak that will serve to reduce $w_t$. (c) A plot of the delay $\Delta t_d$ against measured delay (using an external oscilloscope) shows clear regions where the delay gets stuck; the scatter in the inset shows an average step size of 1 ps, but with several ps variation possible.

When we plot the AWG's delay at picosecond increments, and use a sampling oscilloscope to check the actual delay, we record the traces in Fig. 5.7(c). Here, we see that overall the delay is approximately linear, but there are specific values of delay it cannot achieve, as it gets stuck. To some extent we can work around this a bit by using hardware skew and integer point shifts alone. The inset to (c) shows the scatter, which shows that the average step size is 1 ps, but it is possible to have several ps steps at points where the delay gets stuck. We switched to another AWG, a Tektronix 70K series, which was linear to the 1 ps level. This way we can achieve 1 ps accuracy.

## 5.4 Incorporating Energy Broadening

The shape of $w_t$ plotted in Fig. 5.6(c) can be understood using energy broadening of the electron wavepacket, created due to the dynamic quantum dot of the electron pump varying on a timescale faster than the tunneling time over the exit barrier. This gives the elliptical form expected of $\rho(E,t)$. We relax the requirement now that $\rho(E,t)$ is separable and write a combined energy-time wavepacket

$$\rho(E,t) = \frac{1}{2\pi\sigma_t\sigma_E}\exp\left(-\frac{(E-\beta t)^2}{2\sigma_E^2} - \frac{t^2}{2\sigma_t^2}\right) \tag{5.5}$$

where $\sigma_{E(t)}$ is the standard deviation in each axis $(E,t)$ with relation to experiment $\sigma_t = w_t/\left(2\sqrt{2\ln 2}\right)$ and $\sigma_E = w_E/\left(2\sqrt{2\ln 2}\right)$. $\beta$ represents the correlation - the slope of the semi-major axis defining $\rho(E,t)$.

In Fig. 5.8 we plot a comparable dataset to Fig. 5.6(c) and fit the above form of $\rho(E,t)$ as follows. As shown in Fig. 5.2, the mAED is approximately equivalent to the AED, so $w_E$ is a direct measure of the energy broadening [8]. We find this to be about 2.4 meV. We assume that $T(E,t)$ is a step function, with the step centred about $t = 0$, for ease of calculation. The slope of measurement (horizontal axis in Fig. 5.6)(c) is then incorporated into the energy broadening $E$. In this case, the current distribution reduces to the simpler

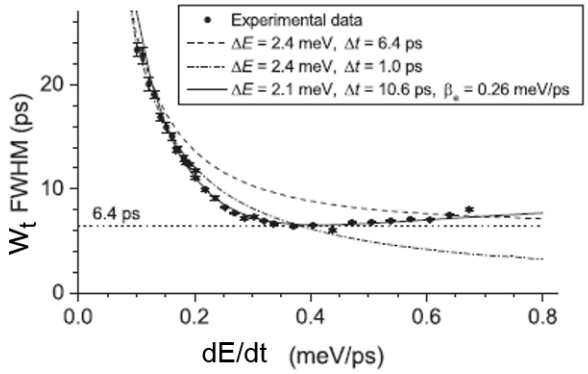


Figure 5.8: The variation in $w_t$ with slope of step of the detector can be explained by allowing a correlation term $\beta$ in the form of $\rho(E,t)$. Data, points, is equivalent to that plotted in Fig. 5.6(c). The dashed line is a best fit, using the minimum measured $w_t \equiv \Delta t$ of 6.4 ps. The dot-dashed line plots a fit taking a minimum value of $w_t = 1$ ps. Neither of these traces presents a good fit, but a much better fit can be found if we introduce the correlation $\beta$, as plotted with the solid line. Taken from Kataoka [77].

form $dI_d/d\Delta t_d = \rho(t)$, where $I_d$ is the transmitted fraction of $ef$ at a given time $\Delta t_d$. We know $w_E$ from experiment ($w_E$ is simply derived from a DC detector barrier scan), so we can reconstruct the form of $\rho(E,t)$. If we assume that the minimum recorded value, $w_t = 6.4$ ps, is entirely constituted by $\rho(E,t)$, then we get the case of the dashed line in Fig. 5.8 ($\beta = 0$ here), which does not fit the data. If we let $w_t = 1$ ps, the small size limit, we get the dash-dotted line, which again is a poor fit. We see that we have to let there be a non-zero $\beta$. Numerical analysis of tuning $\beta$ gives the solid curve, and we arrive at an optimum $\beta = 0.26$ meV/ps and an electron ATD $w_t = 10.6$ ps for this particular pump and pumping configuration.

So, this result shows us there is a strong likelihood of energy-time correlation in $\rho(E,t)$, as we would expect for a dynamic quantum dot. It shows us the fraction of the mATD that is attributable to the ATD and the barrier transmission.

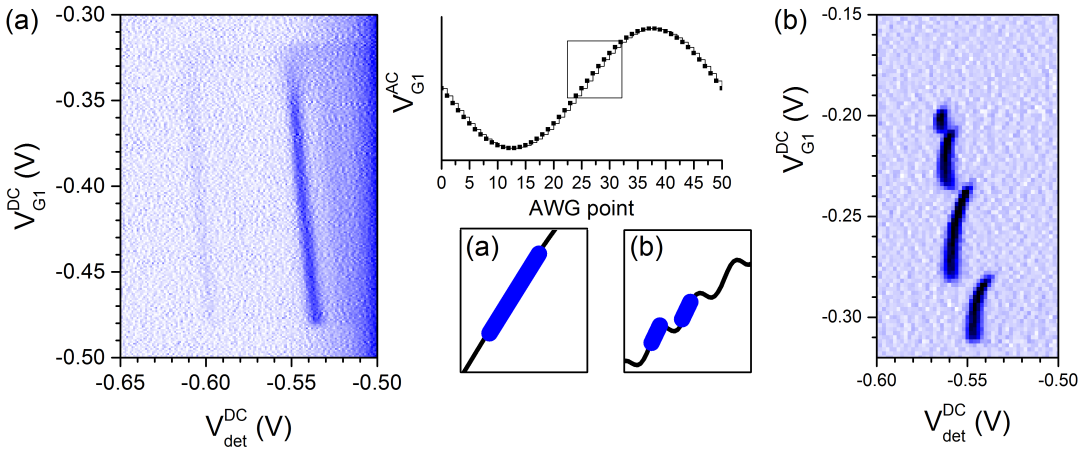


Figure 5.9: Comparison of emission energy and mAED for (a) a smooth filtered sine wave and (b) Unfiltered sine wave, with AWG harmonics present. The centre sketch shows the constructed waveform $V_{G1}^{AC}$ in each case, with the blue line highlighting the region of electron emission in the waveform in the lower sketches, corresponding to the boxed region in the full period plot.

## 5.5 Towards control of $\rho(E,T)$

We have developed a method to obtain the form of $\rho(E,t)$. We need to now establish if $\rho(E,t)$ changes as a function of the pumping parameters, as we would expect if it is modulated by a dynamic quantum dot. To some extent, showing $\beta \neq 0$ has shown this, but we want to work towards tunability of the wavepacket (say, for increasing the SES bandwidth). To give us more scope to change $dV_{G1}^{AC}/dt$ we remove the filter on the AWG output. This means the pump is driven by a sine wave which has 12 GHz oscillations superimposed, an artefact of the AWG 12GS/s sampling rate, as we saw in Fig. 2.8. Emission from a pump driven by this waveform was studied extensively by Waldie [67], and it is known the electron emission times and energies jump from oscillation peak to oscillation peak as we change $V_{G1}^{DC}$. Rather than just move around the pump quantisation map and going through the process detailed above, we can just examine the energy and temporal widths of electrons from these oscillations in a simple transport map. This is shown in Fig. 5.9.

In Fig. 5.9(a) we plot the arrival energy of the pumped current as a function of $V_{G1}^{DC}$, which shifts the point in the waveform at which the electron is loaded and emitted. In the

case of a sine wave, emission shifts smoothly along the curve, and there is hardly a change in energy, as the almost vertical solid line shows. The corresponding sketch in the centre shows the sine wave form of $V_{G1}^{AC}$, and the boxed area shows the approximate emission point. When we remove the filter however, we see that emission is no longer smooth, but jumps around between segments. This is why the current is discontinuous as a function of pump driving waveform, and is a result of the AWG DAC sampling rate oscillations (as we measured in Ch. 2). Further we see some curvature, which probably reflects the shape of the pump drive waveform at the point of emission. The key observation is a clear variation in width of the mAED in the energy (horizontal) axis, which is an indicative sign that we can change the form of $\rho(E,t)$ with pump parameters. This shows we can measure the point in the pump cycle $V_{G1}^{AC}$ at which the electron is emitted from the pump, and this tells us where we should change $V_{G1}^{AC}$ so that we can choose the gradient $dV_{G1}^{AC}/dt$ that will allow selection of the ATD. A larger $dV_{G1}^{AC}/dt$ will give a smaller ATD. Through the correlation $\beta$, this also gives control of the AED.

Fig. 5.10 puts this to the test. In (a), we plot the form of $V_{G1}^{AC}$ where we have modified a sine wave to have a small step in it, at the location we expect emission from the pump to occur. In (b), we plot the equivalent map to Fig. 5.9(b), for this modified sine wave. We see that now each emission segment is not of approximately the same size, and there is one long segment, marked by the bracket. This corresponds to emission from our step, and shows we have precise control over the point in the pumping cycle at which forward tunneling occurs [1]. We now compare some different sized steps, corresponding to a different $dV_{G1}^{AC}/dt$, to see if the ATD changes. To be quantitative, we note that the minimum recorded $w_t$ is highly dependent on the parameter $\beta$. As we expect $\beta$ to change with pumping parameters, we can expect the minimum $w_t$ to change, and so tracking the change in this minimum is all we need to do to show dependence on the pump. Our experimental pump parameters ultimately change one thing: $dV_{G1}^{AC}/dt$, which affects how much energy broadening will be seen in the

[1]This has important implications for pump accuracy: higher accuracy has been achieved by reducing $dV_{G1}^{AC}/dt$ in the part where loading occurs [16].

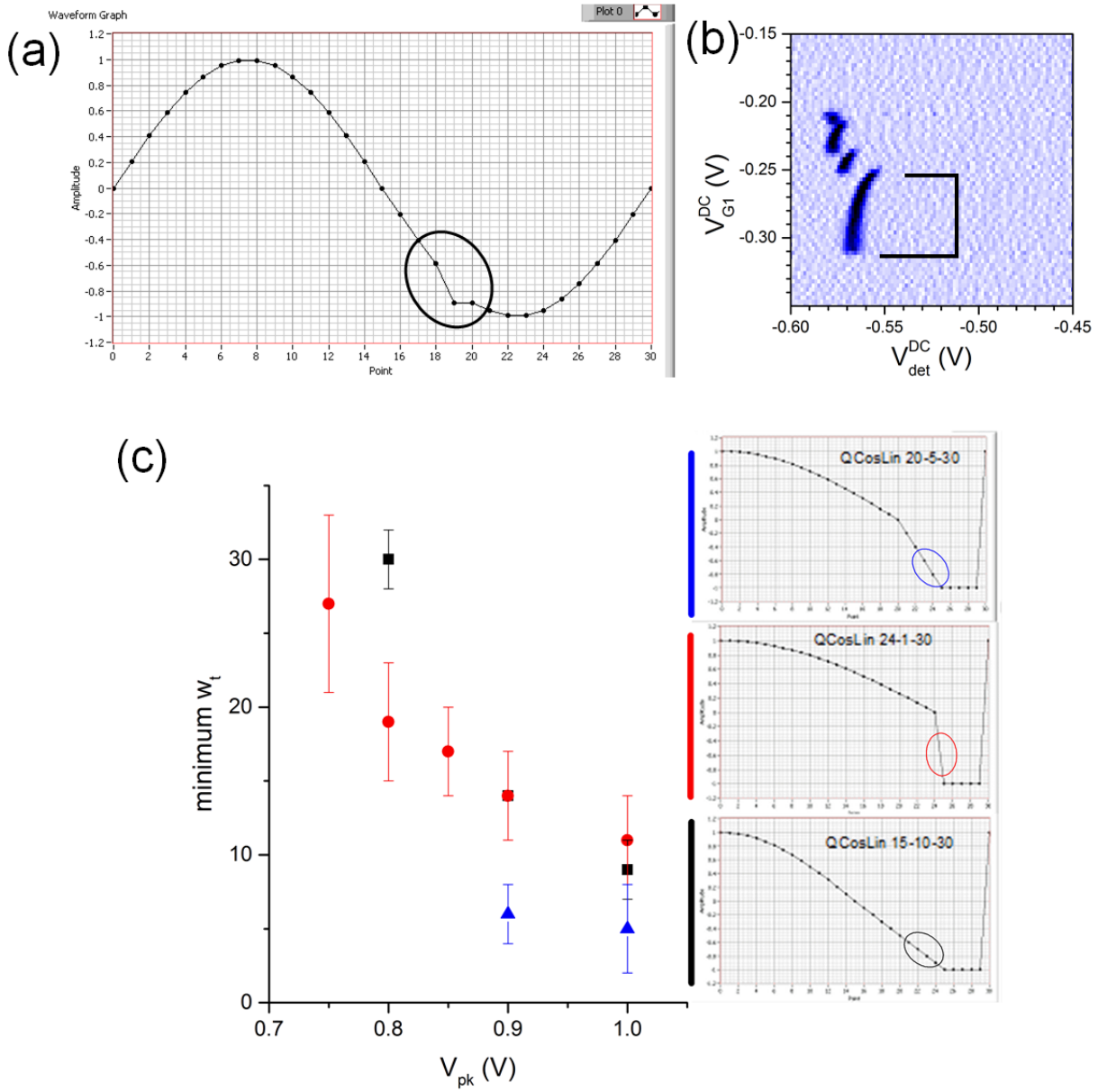


Figure 5.10: Identifying the point of electron emission in the driving waveform. (a) We devise a sinusoidal waveform for $V_{G1}^{AC}$, where we have inserted a small step near the point of electron emission from the pump (circled). (b) The map of the ejection point, similar to Fig. 5.9(c), but we see a larger line of emission, attributable to the larger step between AWG points, highlighted with the bracket. (c) We construct three waveforms with different sized steps, to give different rates of pump quantum dot change in profile with time $dV_{G1}^{AC}/dt$, in an attempt to tune the size of $\rho(E,t)$ through observation of $w_t$. Whilst there is qualitative agreement, there is some ambiguity about a direct relationship between slope and ATD size. Colour of circles highlighting the steps matches the colour of the data points.

exit barrier tunneling time. This derivative is changed by the experimental parameters waveform shape, frequency, offset and amplitude. In addition we could change the electron wavefunction, e.g. by changing $B$, which would change the wavepacket size to vary with the magnetic length. Here, we will just focus on the waveform, and in Fig. 5.10(c), we plot the minimum $w_t$ (i.e. minimum mATD) for different amplitudes ($V_{pk}$) of three different waveforms. Each waveform is plotted to the right, with the circle locating the point where emission occurs. We see that the minimum mATD size does change with $dV_{G1}^{AC}/dt$, becoming smaller with a faster rate of change of the QD confining potential, in agreement with what we expect. There is a little ambiguity here, as the waveforms show clear variations in gradient at the emission point, but are less conclusive in the plot of minimum $w_t$. For example, we would expect the red waveform to deliver the fastest rate of change and so give the smallest wavepacket, but this is not so. The reasons for this are unclear at the moment. Maybe this arises because there are oscillations from the AWG projected on to the step, which change in amplitude as a function of overall output amplitude. This is where we could use the SES scheme to identify the complete waveform shape on chip, but we note that we would have to run it at the full 1 V peak-to-peak amplitude on the detector, which we cannot do owing to the huge back-action and crosstalk this would induce on the pump, and would distort our waveform finer features.

## 5.6 Conclusions

To conclude, we have defined and confirmed the form of our measured temporal and energy wavepackets that we had been implicitly using in the preceding chapters. We found the measured wavepackets consist of two components, the electron distribution and the barrier transmission function. We found a way to separate the two components and found that the electron energy and temporal wavepacket sizes are correlated, which is what we should expect to see from a dynamic quantum dot. We explored how the pump driving waveform $V_{G1}^{AC}$,

which defines the pump quantum dot confinement, affects the electron temporal distribution, by affecting the tunneling time over the exit barrier $G_2$. This indicates tunability should be very possible, and we should be able to create electron wavepackets with specified size. However, this turned out to be more difficult in practice; although we can determine the point in the pump drive cycle at which the electron is emitted straightforwardly, it seems the temporal size control at the emission point is very sensitive to the finer harmonics present in the waveform, and so is harder to control. Perhaps we are also very sensitive to the electron wavefunction within the dot - perhaps, say, through the magnetic length, which determines the size of the wavepacket in the quantum dot, implying we may need to tweak all the pumping parameters (field, dot shape, size, etc.; see section 1.4). If we overcome this though, this could serve as a readout of a prescribed state, or to boost the bandwidth of the SES scheme.

Combined with the detection methods of Ch. 2, we can build up a comprehensive picture of the electron wavepacket, with its energy and temporal spread, its time of arrival, and any energy loss (scattering) that may have occurred. With the LO-phonon mode suppression, we have the tools in place to begin to build the interferometer, which is where we shall head next.

# Chapter 6

# Towards a Single Electron Interferometer

## 6.1 Introduction

Over the previous chapters we have got to know our hot pumped single electrons. We have understood their propagation, by mapping the potential profile of the edge states. We have measured their speed in these edge states. We have got to grips with their relaxation modes, and found a solution to suppress this by orders of magnitude. We have characterised the notion of "wavepacket" for this system. Technologically speaking, we have developed a highly sensitive detector barrier capable of picosecond and meV resolution, with a very high bandwidth. By suppressing LO phonon relaxation we can create devices with many microns of path length. These results hint at coherence of the wavefunction across the device, which could be of technological use. But we must go one step further, and prove coherence, by observing interference. That is the task of this chapter.

In this final chapter I detail our attempts to do this. It proved to be a mighty technical challenge, requiring a new device with new fabrication techniques. We were unlucky to be hit by technical difficulties and a lack of time. That said, my body of work should make this

entirely possible to do in the near future. We begin by discussing the theory, and what we should expect to find in our sample. Next, we proceed to detail our efforts, and we finish by concluding the next design.

## 6.2 Interference

We wish to demonstrate phase coherence of our hot electron, from pump to detector. This is an important step in showing we can create a prescribed state. Scattering events, such as emission of an LO phonon, do not preserve the state. It may not be possible to create a scattering free environment, as the acoustic mode work hints at, with a continuous emission process happening from the moment of pumping, but this may only reduce the visibility of interference effects [81]. The easiest way to show coherence is to observe an interference pattern. Specifically, we will look for the Aharonov-Bohm effect.

### 6.2.1 Aharanov-Bohm Effect

The Aharanov-Bohm (A-B) Effect is a manifestation of the effect of electromagnetic potentials, even when the related electric and magnetic fields may be zero. One of the traditional ways of demonstrating this effect, and relevant to our situation, is that of an electron wavepacket being split and travelling around a solenoid and then recombining, as sketched in Fig. 6.1 [105, 106].

Here we have a solenoid which contains a region of enclosed space of area $S$, in which $\mathbf{B} = B_z \neq 0$. Outside the solenoid, $B = 0$, including in the electron path lengths $l_1, l_2$. From Maxwell's equations we can write $\mathbf{B} = \nabla \times \mathbf{A}$, with $\mathbf{A}$ the vector potential. $\mathbf{A}$ is not uniquely defined, however one way we can express it is as $\mathbf{A} = \frac{SB}{2\pi r}\hat{\phi}$, with $SB$ the magnetic flux enclosed in the solenoid and $r$ the radius of the electron path from the centre of the solenoid (we use polar coordinates, c.f. Fig 6.1). The electron traveling in the path around the solenoid will evolve according to the Schrödinger equation with Hamiltonian

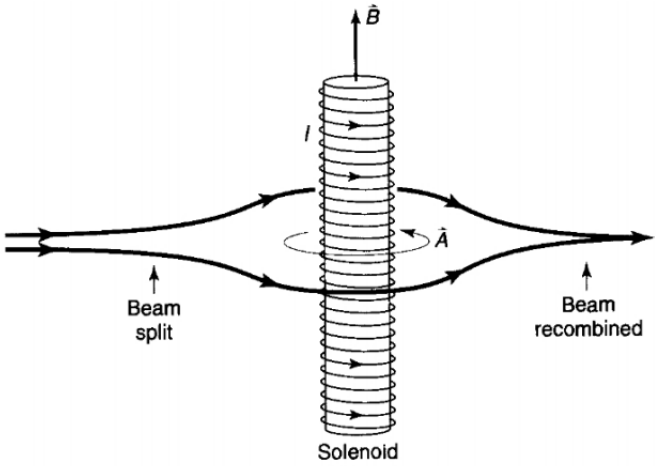


Figure 6.1: One method of demonstrating the Aharanov-Bohm (A-B) effect. A current is split to traverse a region surrounding a solenoid in which the field $B$ is non-zero inside the solenoid but zero elsewhere. An interference pattern will result, due to the vector potential $\mathbf{A}$ being non-zero on the paths, and causing a phase difference to arise between the paths. Taken from Griffiths [106].

$H = \frac{1}{2m}\left(-i\hbar\nabla - e\mathbf{A}\right)^2$ (plus a term for the electric potential, but we take it to be zero). It can be shown that the solution to this Schrödinger equation is a wavefunction that we may write as $\Psi = e^{ig(\mathbf{r})}\Psi_0$, where $e^{ig(\mathbf{r})}$ is the phase [104,106,107]. As $B = 0$ throughout the path, we have path independence outside of the solenoid, and so we may write the phase factor $g(\mathbf{r}) = \frac{e}{\hbar}\int_{l_1}\mathbf{A}.d\mathbf{r} = \frac{e}{2\hbar}S.B$ [106–110]. The phase difference, $\phi$, between the two routes is then the difference between the two line integrals $\phi = \frac{e}{\hbar}\left(\int_{l_1}\mathbf{A}.d\mathbf{r} - \int_{l_2}\mathbf{A}.d\mathbf{r}\right) = \frac{2\pi SB}{\Phi_0}$, with $\Phi_0 = h/e$ the magnetic flux quantum, and it is this phase difference that gives rise to the A-B effect.

Some parallels of the solenoid setup described and our experiment are clear: our electron paths will be defined by the hot edge states, and we can use a gate, analogous to the deflection barrier, to split the pumped current. Our detector barrier will serve to readout the transmitted current and observe the expected oscillations in this current that will be the signature of the A-B effect.

To get an idea for the specifics of the device design, we turn to the literature which has many examples. Of interest are the explorations and observations of A-B interference

using quantum Hall edge channels, as these act as our (hot) waveguides, in which interference has been successfully observed [111, 112]. Some common geometries used include tunneling to/from antidots [113,114] or quantum dots [115], Fabry-Perot [87], where counter-propagating edge states are brought close together so tunneling can occur between them, or the Mach-Zehnder geometry [116–119], in which edge states are split. A Mach Zehnder type idea, where edge states are split, is close to what we have already done when conducting the velocity measurements, and we shall utilise this geometry in our design. Theoretical descriptions of interference in these geometries or the closely related Hanbury Brown Twiss geometry explain well the above observations [81, 82, 120–123], and we use these works as a guide to the expected action in our system.

Of particular interest is the work by Ji [118] and Neder [119], who utilise not just the Mach Zehnder geometry common to the above works, but also the same GaAs/AlGaAs gated heterostructure as employed in our system. They successfully measured the A-B effect in a single edge state (integer quantum Hall effect, filling factor $\nu = 1$) that was partitioned and recombined by two surface gates at the Fermi Energy. This is the closest analogue to our system, and we use these works to be the basis of our design. Fig. 6.2(a) shows their device and (b) their results, showing clear oscillations.

Using their observations, and the work governing transport in edge states by Büttiker [82], we expect that the current in the detector will vary according to the phase difference as

$$I \propto \left|t_1 t_2 + r_1 r_2 e^{i\phi}\right|^2 = \left|t_1 t_2\right|^2 + \left|r_1 r_2\right|^2 + 2\left|2 t_1 t_2 r_1 r_2\right| \cos(\phi) \tag{6.1}$$

with $t_i$ being the transmission across the i$^{\text{th}}$ deflection barrier, and $r_i$ the reflection, and the phase $\phi = 2\pi BS/\Phi_0$ as above and $t_i^2 + r_i^2 = 1$. We see then that the important experimental parameters are the field $B$ and the area $S$. $S$ will be fixed in the design and then we may vary $B$ to observe the oscillations (although we can use depletion gates to move the edge state position, it will not change $S$ much). We define a period of oscillation $\Delta B = \Phi_0/S$,

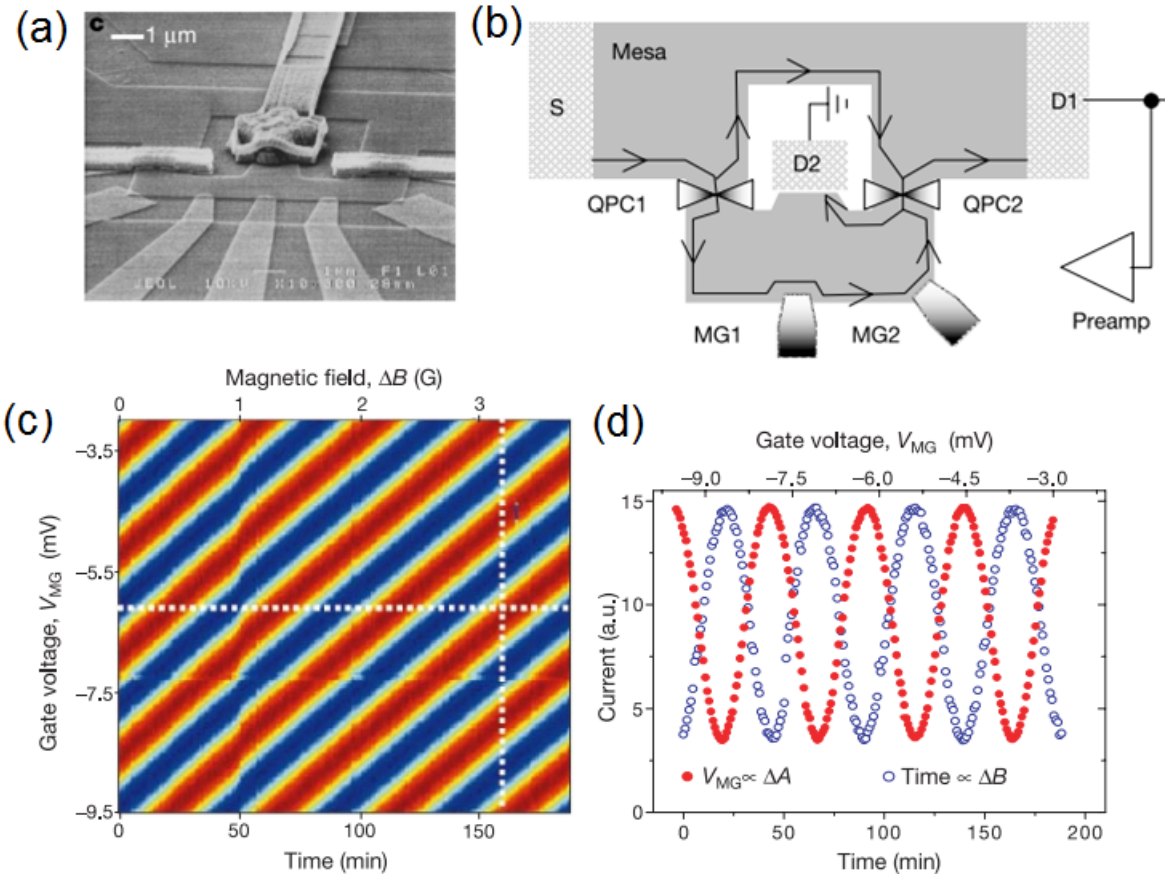


Figure 6.2: The device and results of Ji et al. [118], which most closely resemble the realisation of the A-B effect we will attempt in this chapter. (a) Image of the device used. The A-B ring is defined by e-beam etching, with surface gates used to partition current. Lower, thinner surface gates serve to change the area enclosed. The small ohmic drain is visible in the centre of the ring, connected to ground by an air bridge. (b) Schematic of the Mach Zehnder geometry employed using edge states at the Fermi Energy. (c) Resultant interference pattern observed in the drain D1 as a function of field $B$ and area $s$ (via the lower modulation gates). (d) Cut through of interference pattern shown in (c), at the points marked with white dashed lines. In red the vertical cut showing oscillation in current change with area, and in blue the horizontal cut showing oscillation with field. All taken from Ji et al., [118].

and we see that we need the area $S$ to be as small as possible to maximise $\Delta B$. Our control of the fridge magnet is probably not better then 1 mT (its loss is a few mT per week) which gives a maximum $S \approx 4\ \mu\text{m}^2$.

Hence, we will design a Mach - Zehnder geometry based closely on this design. We will vary the magnetic field perpendicular to the 2DEG plane, and expect to observe current oscillations of the form derived above. We will need to use depletion gates to stop phonon scattering which will dephase the current. The visibility of the oscillations is defined as $\nu = (I_{d_{max}} - I_{d_{min}})/(I_{d_{max}} + I_{d_{min}})$ and is maximised when both deflection gates are tuned to 1/2. Ji reported visibility of up to 0.6, and Neder 0.5. If we pump at our standard frequency of 240 MHz, our input current to the interferometer is $\approx$ 38 pA. At half transmission, the maximum variation in the current for both partition gates at half transmission is $\approx \frac{1}{4} \approx 10$ pA and should be detectable. We cannot achieve full visibility with finite temperature, and as we are working far above the Fermi energy, we cannot expect to match the published visibilities. We also must contend with crosstalk, which will serve to oscillate $t$ about the half-transmission. We will use depletion gates to remove LO-phonon emission. If we are unlucky, all of these will impact the visibility to be of order 1 pA or less and it becomes undetectable. Our best insurance is to minimise the area $s$. However, this is further complicated by the need to drain excess charge from the ring (see Fig. 6.2(a), (b)). Ji et al. uses an ohmic contact to act as a sink to stop current making multiple laps of the ring, which could cause charging and unwanted electron-electron interactions. We will need to implement a drain also.

## 6.3 Design

The design has much in common with the devices explored in the previous chapters, however we have developed some new features that have required a change to the conventional NPL fabrication methods. We shall describe the new features of this device and their intended

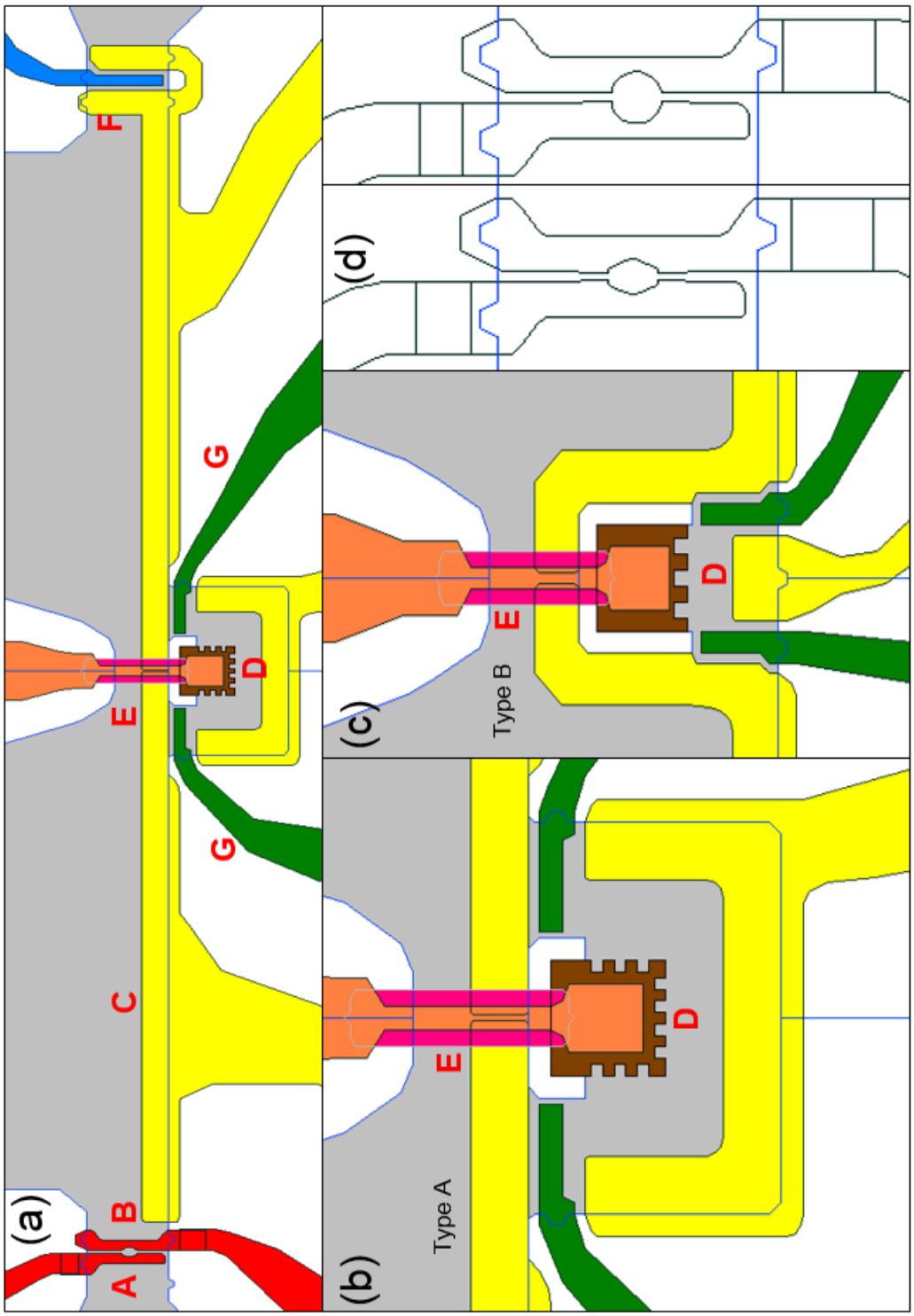


Figure 6.3: TurboCAD device design. (a) The complete device, with 2DEG region shaded grey, pump gates in red, detector in blue, depletion gates in yellow, partition gates in green, the small ohmic in brown, connected to ground via the orange line. New features are labeled with red letters, A - elliptical quantum dot based pump; B - two stage e-beam gate writing; C - large separation between pump and interferometer and interferometer and detector; D - small ohmic contact; E - bridge to connect ground line to small ohmic contact; F - Detector barrier surrounded by depletion gate; G - deflection barriers for partitioning current. (b), (c) The two different ring designs, Types A and B, defining the handedness of the interferometer. (d) The new elliptical pump, left, compared with the standard circular pump, right.

use. Fig. 6.3(a) shows a TurboCAD image of the device design. We have our 2DEG, shaded in grey, and we design a four terminal device, with Ohmic contacts out of view. The same colour coding is employed to label devices as per previous chapters: electron pump - red, depletion gates - yellow, deflection gates - green, detector - blue. We use the same mask as has been used for the previous devices, giving the contacts as shown in Fig. 1.2. The new features are labelled with red letters, which we shall now describe.

A **Elliptical pump** This is designed to have an elongated QD shape, which may change the form of the exit barrier profile the electron tunnels across to be pumped. The logic here is that we might be able to decrease the wavepacket temporal size by presenting an exit barrier thickness that changes less rapidly with distance than in the circular QD case. We may need better temporal resolution to view A-B oscillations, or to view the crosstalk between gates, so we may counter it. Additionally we could use this device to explore more aspects of wavepacket control. This may give the wavepacket a smaller energy distribution, as it is tunneling from the pump faster, which could increase visibility. We also make some devices using the tried-and-tested circular pump, as used in previous chapters. We compare the two pumps in panel Fig. 6.3(d).

B **Two stage e-beam gate** We test thinner gates for the length spanning the 2DEG. In the previous devices we had used a single e-beam stage to write the gates, of typical thickness 45-80 nm. The new two stage process allows for the 2DEG span to be written first, with thickness 25-30 nm, and then the leads as before, which have the thickness to climb up the etch onto the previous stage. The idea with the thinner gates is to allow finer control in the fabrication of smaller structures. As we move towards wavepacket tunability, we may become more sensitive to pump gate geometry. On this device, all gates, not just the pump, are 2-stage.

C **Long separation between AC gates and active area of device** Knowing that we can suppress LO-phonons for lengths of up to 1 mm, we can afford to spread components on the device apart. This should give reduced crosstalk between AC signals and DC gates,

that we have found impacts upon our energy resolution, in the LO-phonon measurements. Separating the pump from everything else should reduce this effect. Of course, the yellow depletion gates span the complete length. We fabricate two lengths - 10 and 15 $\mu$m separation in case unknown effects become apparent in very long path lengths. The detector is separated from the ring by the same amount.

**D Small Ohmic Contact** This acts as drain for the ring area. Electrons proceeding around the ring many times may lead to charging and unwanted electron-electron interactions. The contact would be grounded at all times to prevent more than one traversing of the ring. This required a new method and so will be discussed in a section of its own later.

**E Bridge** This is the support that allows e-beam defined gate metal to cross into the ring centre to connect with the small ohmic contact. This has to be done in a way that allows the hot current to continue underneath unperturbed, and for the depletion gates to extend underneath such that we can remove the possibility of LO-phonon emission occuring underneath the bridge.

**F Detector** The detector is much the same as before, except that we extend the depletion gate to surround it. The logic here is to see if the extra depletion and profile potential barrier will make it harder for rectified current to propagate across the detector and swamp the measurement. Here, rectified current is current generated by a potential difference across the detector transmitted and reflected current Ohmic terminals due to pick up from the pump drive $V_{G1}^{AC}$ [46]. It is seen in all devices and can be problematic when it occurs within our desired measurement space.

**G Deflection Barriers** In the search for A-B interference, we would expect to set these gates at half transmission, and hold them there, without crosstalk from the pump drive changing the transmission. One way we combatted this is to increase the path length (C). Another way is to change the sample holder so that we can introduce AC signals to these two gates too. That way, we can use an AWG to output a null waveform, so that the gate potential is very rapidly reaffirmed to the set value. It is difficult but not impossible to

construct an AC waveform to counter the pump drive pickup.

Finally, we design two different ring geometries: Type A and Type B, drawn in Fig. 6.3(b) and (c). These have slightly different areas, of 7 $\mu$m$^2$ and 3 $\mu$m$^2$, giving our expected period $\Delta B \sim 0.5$ and 1.4 mT respectively. Whilst the 0.5 mT period may be pushing our field control, we could let the field decay naturally over time to observe the oscillations. They have different handedness, and different ratios of path lengths. Additionally, we may find that the small ohmic with or without an etch around most of its perimeter is more easy or difficult to fabricate (an early concern was whether it would stick - it turns out the etch was not critical in this).

With this design we can already see one weakness: there is a possibility there will be an LO-phonon emission under the bridge that cannot be removed by depletion. This will reduce the visibility as there will be unequal currents at the pumped energy recombining on the second paertition gate. Because of the formidable challenge of constructing the bridge, we will have to live with that for now.

The above features should allow us to maximise our visibility. Two particular features required new techniques: the small ohmic, which we discuss next, and the bridge, which we discuss in the device batches to follow.

## 6.4 Ohmic Contacts

Our usual Ohmic contacts used to connect with the 2DEG in the samples of previous chapters have an approximate area of $\sim 5.1 \times 10^{-8}$ m$^2$, and are made optically using a Au/Ge/Ni slug (co-evaporated elements), with a further optical layer of Au to bond. For spike-down, they are baked for 80 s at 430 °C. Typical resistance is a few k$\Omega$.

We expect that it is not straightforward to scale down the area with the same recipe. This is because it is understood that the density of spikes is dependent on the Ge content, so as we reduce the material we will reduce the density of spike-downs. The spike down process

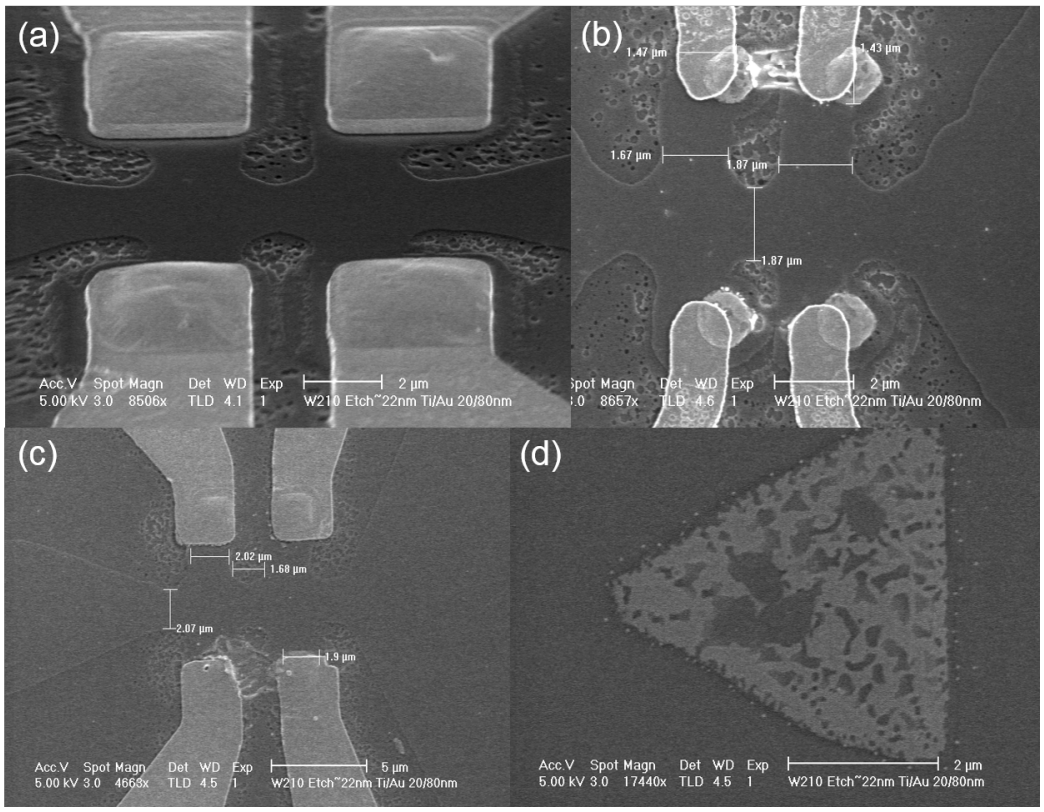


Figure 6.4: First batch of small ohmic contacts. (a) e-beam etching defines a Hall Bar (darker region) on which the contacts connect to, with e-beam gate metal used to make contact. (b), (c) In some cases, we see alignment as an issue, and the etch after deposition of the contact seems to affect the contacts. (d) A test structure contact, with no surface gate Au metal connection, shows clear surface roughness. Is this evidence of spike down?

is not well understood, but we see that it is very sensitive to the annealing process and ratios of elements [124–130]. Au/Ge/Ni are widely reported as the most used and having the highest success rate of contacts, so we can probably use the same materials. Because this will be a drain, and not used for measurement, we can forgo some of the requirement to minimise resistance, as long as it works reliably at the small size.

Owing to the probable high rate of failure that would arise from using our conventional method with a smaller size contact, we tested small contacts in a separate batch before fabricating the complete device. To test the contacts, we simply perform a two terminal resistance measurement between pairs of contacts across a Hall bar, as shown in Fig. 6.4 in a 4 K dip.

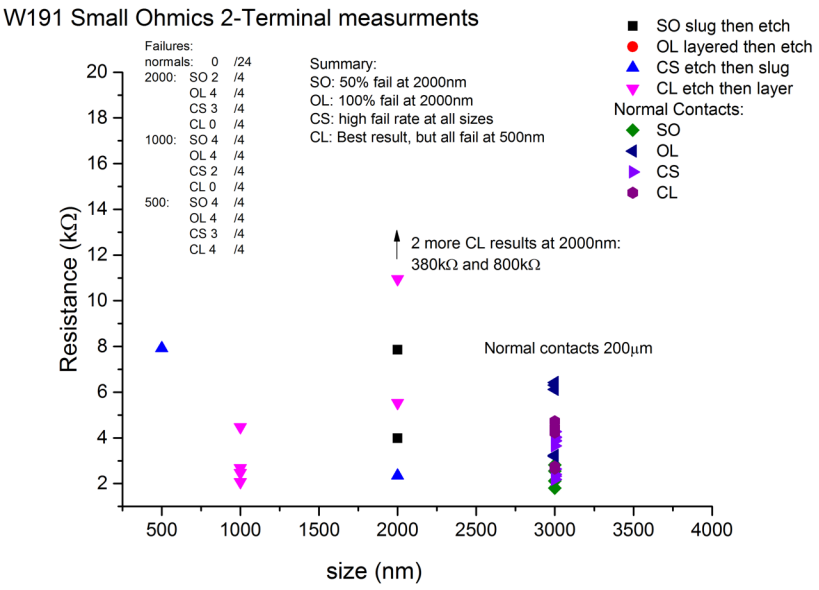


Figure 6.5: Two terminal resistance measurements of the first small ohmics batch, including statistics of failure rate.

The first batch of these tested two parameters: slugs vs. layers and etch first vs. etch after, where this etch is the e-beam etch that defines the path around the ohmic (see Fig. 6.3), giving four designs. The slug is the same as previous work, Au/Ge/Ni, or layered Ni/Au/Ge/Ni/Au, where a thin layer of Ni is added first, believed to help adhesion. The annealing recipe is the same for all samples and is the previously used 80 s at 430 °C. On each sample, we test three sizes of contacts: squares with side length 2000, 1000 and 500 nm. Fig. 6.4(d) shows a contact without the Au surface metal. We see clear surface roughness, and perhaps this is a good indicator of spike-down, because material has moved around to create the inhomogeneities. The resistances are plotted in Fig. 6.5.

The striking result is the high number of failures. These are contacts that are not at all conducting at 4 K, or freeze out on cooldown (conduction drops to zero as temperature decreases). This occurred in all of the layering then etching, and many of the other samples too. All of the 500 nm size except one, and many of the other sizes also failed. This failing may be because of a low density of spikes in the spike down, or maybe not enough material to induce spike down at all. There were no failures in the side (200 $\mu$m) size contacts perhaps

because there was sufficient material over a large area to get the spike-down. The results are not conclusive, but hint that etching then layering is best. Etching first makes sense, because the etch process may damage the ohmic material and unseat the contact, which may be occurring in Fig. 6.4(b).

We take forward that layering seems to give us the highest chance of success, with the e-beam etch around the contact to be done first. We fabricated a complete sample batch using this contact using a 1000 nm size, as it seemed a fair shot. However, we found that they did not conduct at all on this batch, as we detail later. This led to the testing of a second batch of small ohmics, where we tried different recipes.

### 6.4.1 Second Batch

We did not have much success with the contacts when they were embedded in the device, even though they performed with moderate success rate on the Hall bar tests. We now look to other recipes to see if we can boost the success rate. (Here, we simply mean conduction at 4 K, we are not in a position to specify a resitance limit, although we acknowledge that lower resistance is better). This work was based on Göktaş et al., [129,130], which examined techniques to minimise ohmic contact area and understand the spike-down process. They found an approximately half success rate for contacts of side length 750nm. In this batch, we compare our standard annealing recipe with that of Göktaş et al., and test the extreme limits. The annealing recipes are:

- 80 s @ 430 °C, the standard procedure
- 120 s @ 370 °C, then 50 s @ 440 °C, from Göktaş et al.
- 200 s @ 370 °C, the cold limit anneal
- 80 s @ 480 °C, the hot limit anneal

We will compare the rate of success of our recipe with Göktaş's recipe, and see how the conduction success tails off at the cold and hot ends. For all contacts in this batch, we switch to e-beam lithography to create the ohmics, including the large size edge contacts.

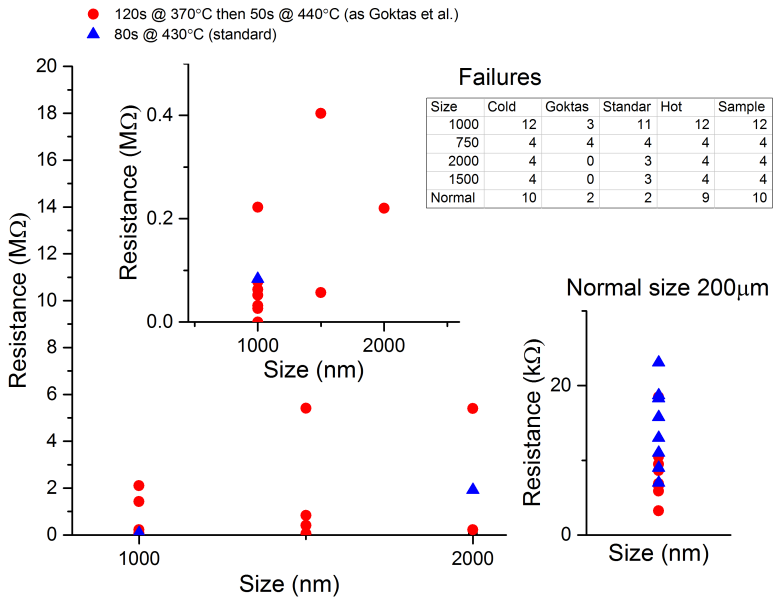


Figure 6.6: Results of two terminal resistance measurements of the second batch of small Ohmics.

Again, this batch is fabricated as contacts on a Hall bar and two terminal resistance was measured at 4 K. We tested four sizes in these batches, 750, 1000, 1500, 2000 nm side lengths. The results are plotted in Fig. 6.6.

The key result is that the success rate is less across all recipes. The extreme hot and cold limit values failed completely, including the large sized contacts. This highlights how sensitive the annealing process is to temperature and time. Our recipe and the published recipe give about equal MΩ resistances, but the published recipe has a much higher success rate. All contacts at 750 nm were non-conducting, in contrast to the publication. At 1000 nm, 11/12 contacts failed in our recipe vs. 3/12 for the published recipe, which is a promising result. Our recipe failed in 3/4 contacts at the larger sizes vs. no failures in the published recipe. This result is fairly conclusive: we should use Göktaş's recipe.

## 6.5 Interferometers

We now construct the full device with the variants described above. Due to the fabrication problems detailed next, we made three separate batches, of the same design.

### 6.5.1 First Batch

At the time of fabrication of this batch, we had only performed the first small Ohmics test, so we used a recipe of etch then layered Ni/Au/Ge/Ni/Au, annealed for 80 s at 430 °C (evaporated, not e-beam). To recap, design variants in this device are:

- lengths 10 or 15 $\mu$m
- Geometries A and B
- circular and elliptical pumps
- PMMA bridge or unsupported bridge

Because we were not sure how well the bridge would perform, we added this extra variant, which we discuss below. There were multiple issues and no sample proved to be working. In this first batch, we did not use two stage e-beam gates. Fig. 6.7 shows the collection of errors we have experienced.

We fabricated 12 samples, of which all presented at least one problem, making them unusable for the experiment. We encountered (with reference to Fig. 6.7) (a) Lift off issues; including in one case a missing gate, and in multiple cases metallisation of the whole ring area; (b), (c) An unknown contaminant that etches deeply into the heterostructure in all samples; it seems to etch GaAs more than AlGaAs, creating overhangs that then appear to collapse; (d) Bridge climb-up; (e) small ohmic adhesion - at least 2 small ohmics were missing. Two samples were tested, but it was found that the conventional Ohmic contacts froze out quickly on cooldown, rendering the devices unusable. The small ohmics did not appear to conduct, but this could be because of the bridge or the ohmic. Frustratingly, the test structures (f), (g) appear to not have any issues (they were not usable because the

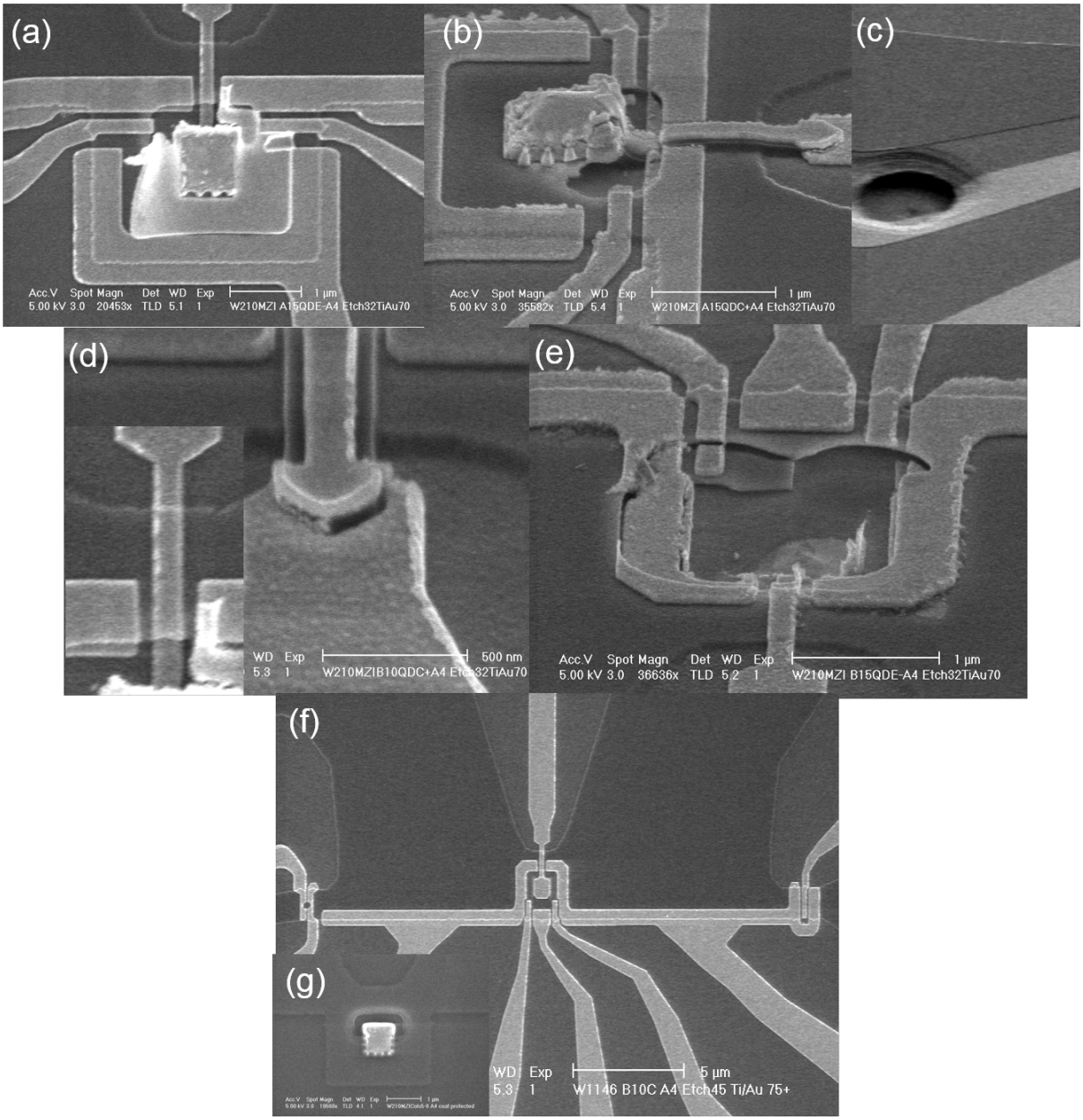


Figure 6.7: The problems encountered in the first batch of interferometers (refer to Fig. 6.3 for the design): (a) Poor liftoff (b), (c) An unknown contaminant that served to etch away GaAs (d) Bridge climb-up not successful (e) Small Ohmic adhesion (also contaminant etch present) (f) The test structure (no small ohmic) appears correct (g) Small ohmic adhesion and alignment in the test batch was good. Images courtesy of Dr. Patrick See.

gate test structure did not have a small ohmic contact, and the small ohmic alignment test structure did not have gates).

So, what has caused all of this? The main problem seems to be the unknown contaminant. This is a material we could not identify, but causes deep etching. To identify the contaminant, the samples were returned to an HCl dip, to see if that would cause further etching, but it left the structures untouched, with no visible change under the SEM. The fact the test structure (f) does not seem contaminated could be becuase there were no ohmics implanted, and that during the ohmic deposition the contaminant was introduced, perhaps from a contaminated evaporator. Perhaps this caused large contact freeze-out, which is very rarely observed with this standard Ohmic recipe. This maybe impacts on the adhesion of the small ohmic too. Lift off is a standard procedure so this is something that should not have failed, and so maybe lingering contaminant could have caused it.

Additionally, we see we have a design problem with the bridge. Fig. 6.7(d) shows the two types of bridge - direct and via PMMA step. Direct, where we e-beam a gate across the surface of the sample, as per the design of the potential barriers, seems to be fine for climbing up from the channel etch, but the small ohmic presents too high a step to reach the top of the contact. This was why we introduced the PMMA bridge, to present two smaller steps. It was inconclusive at the small ohmic side as to whether clear contact with the top metal was made. However, as is shown, the PMMA step is too thick for the drain lead metal to climb up.

Conclusions we draw from this batch are to use less PMMA in the bridge, and that we were unlucky with the contaminant.

### 6.5.2 Second Batch

Batch 2 was fabricated directly after Batch 1, and so used the same Ohmic recipe of etching first, then a layered Ni/Au/Ge/Ni but this time by e-beam with 80 s @ 430 °C anneal. All devices in this batch also failed, although for some different reasons. We introduced a diffuse

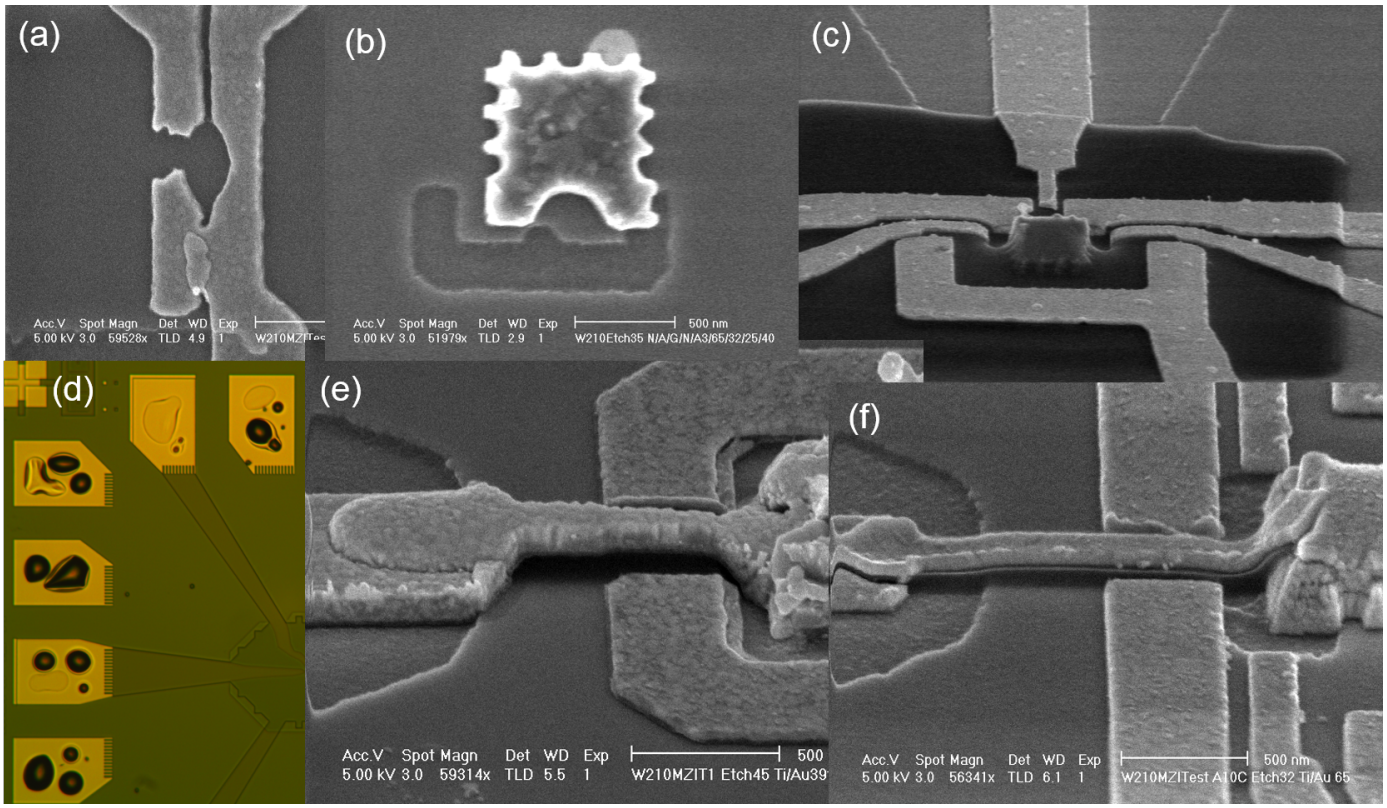


Figure 6.8: Results of the second batch of devices (refer to Fig. 6.3 for the design). (a) e-beam writing issues caused gates to fuse, not be straight or material missing. (b) Some small ohmics were misaligned. (c) PMMA used for bridge flooded some samples. (d) Normal side contacts seem blistered and not annealed, and froze out. (e), (f) On a positive note, the PMMA bridge seems to be successful, showing climb up on both sides.

PMMA bridge, to reduce the step height to get climb-up (again, we made some samples without any PMMA to compare). We give the small ohmic an indentation to give a greater surface area to increase the chance of climb up on to the contact.

There were some failures, but there is also more to be hopeful for as Fig. 6.8 shows. 14 samples were fabricated, and none proved usable. We once again saw lift off problems, affecting six samples. Six samples showed some form of contaminant etch, although not as severely as the last batch. Two samples had no small ohmic present, and further, we encountered some new problems too. The biggest of these was an e-beam write issue, as shown in Fig. 6.8(a), which should have been standard procedure. In the case of the small ohmics this caused misalignment (b). There seems to have been an issue with the PMMA

coating a large area (c). Some of the side contacts (optically made) show blistering (d), perhaps a sign of under- or over-annealing. Those appearing normal froze out when tested, in the same way as before.

But there are some success stories in this batch too. Some of the PMMA bridges seem to work well (Fig. 6.8(e),(f), with probable climb-up on both sides. In this batch, 1 sample looked fabricated without errors (one more than the previous batch!), but sadly its ohmics froze out on cool down.

Going forward, it felt like we were getting close. The e-beam write error was examined and resolved, we had less problems with the contaminant etch (except for the edge contacts), and we had learned the hard way the amount of PMMA required for the bridge.

### 6.5.3 Third Batch

Sadly it was not third time lucky. Because most of the previous errors were failures of standard practice, it was felt not much of the design needed to change. We introduced two stage e-beam gates for this batch. The small ohmics were e-beam written as before, with layered Ni/Au/Ge/Ni and annealed for 80 s at 430 °C. We got the furthest in this batch, managing to test some pumps. However, there were problems with all the devices.

This was a batch of 16 samples, and we tested 11. One sample showed poor lift off and two had no small ohmic present - certainly lower rates than seen previously. Of the others, the active area of the device looked fine. Fig. 6.9(a), (b) show a problem-free device. The two stage e-beam has worked well, and the bridge seems to certainly connect with the small ohmic when using diffuse PMMA. The main problem, shown in (c), is that the side ohmics appear underdosed. This made them extremely difficult to bond to, with bond wire often pulling all of the surface metal away so no further bonds could be made, and reveals little ohmic material in place. We lost several samples in this way. (d) Shows a difficult way around we attempted to recover some devices, using Ag glue. This is quite an invasive process and unsurprisingly the devices did not behave well, probably due to a loss of ESD

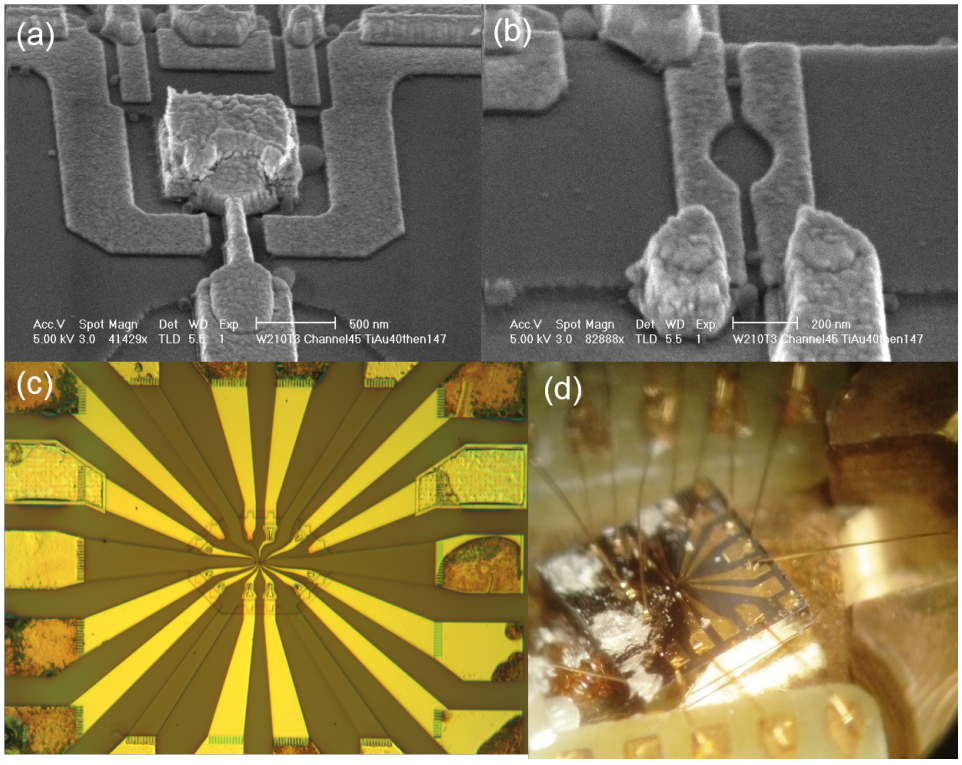


Figure 6.9: Results from the third batch of interferometers (refer to Fig. 6.3 for the design). (a) The active area of the devices looked without problem for the majority of the devices. The bridge looks convincingly to make contact. (b) Two stage e-beam process seems to have gone without a loss of continuity. (c) Side Ohmic contacts were underdosed, resulting in the discolouration. (d) The contacts were very difficult to bond, resulting in the need to use Ag adhesive to bond, which is difficult and compromises ESD safety.

control whilst applying the silver.

In the 4 K dip, some of these contacts did not conduct at all, suggesting insufficient material to spike-down. Some did however, and we managed to test some devices at 4 K (no previous device got this far). We found a new problem, in that the pumps on all the tested devices were poor, even for the established circular design. Fig. 6.10 shows the quantisation maps and the step-like current traces. In (a) we show the best and worst of the elliptical designs, and in (b) the best and worst of the circular design. Each plot contains a quantisation map (c.f. Fig. 1.3(d)) and line cuts that ideally would be step-like. None of these pump maps show good quantisation, with many previous devices easily achieving better than this at 4 K. This is a surprise, considering the circular design has been shown to be better in the past on the same wafer.

These are barely good enough to work with, but there was no opportunity to work with them anyway as the devices had other issues, namely not all side ohmic contacts were conducting and/or the small ohmic not conducting.

This batch was almost a success, and if the fabrication of the ohmic contacts had been routine, we could have found a working device. The quality of pumps was a surprise, and there is no clear cause of the poor performance. With field and lower temperature the pumps may have improved, but it serves to show that it is worth pretesting pumps in the same way as the small ohmics to save a lengthy multi-stage fabrication process.

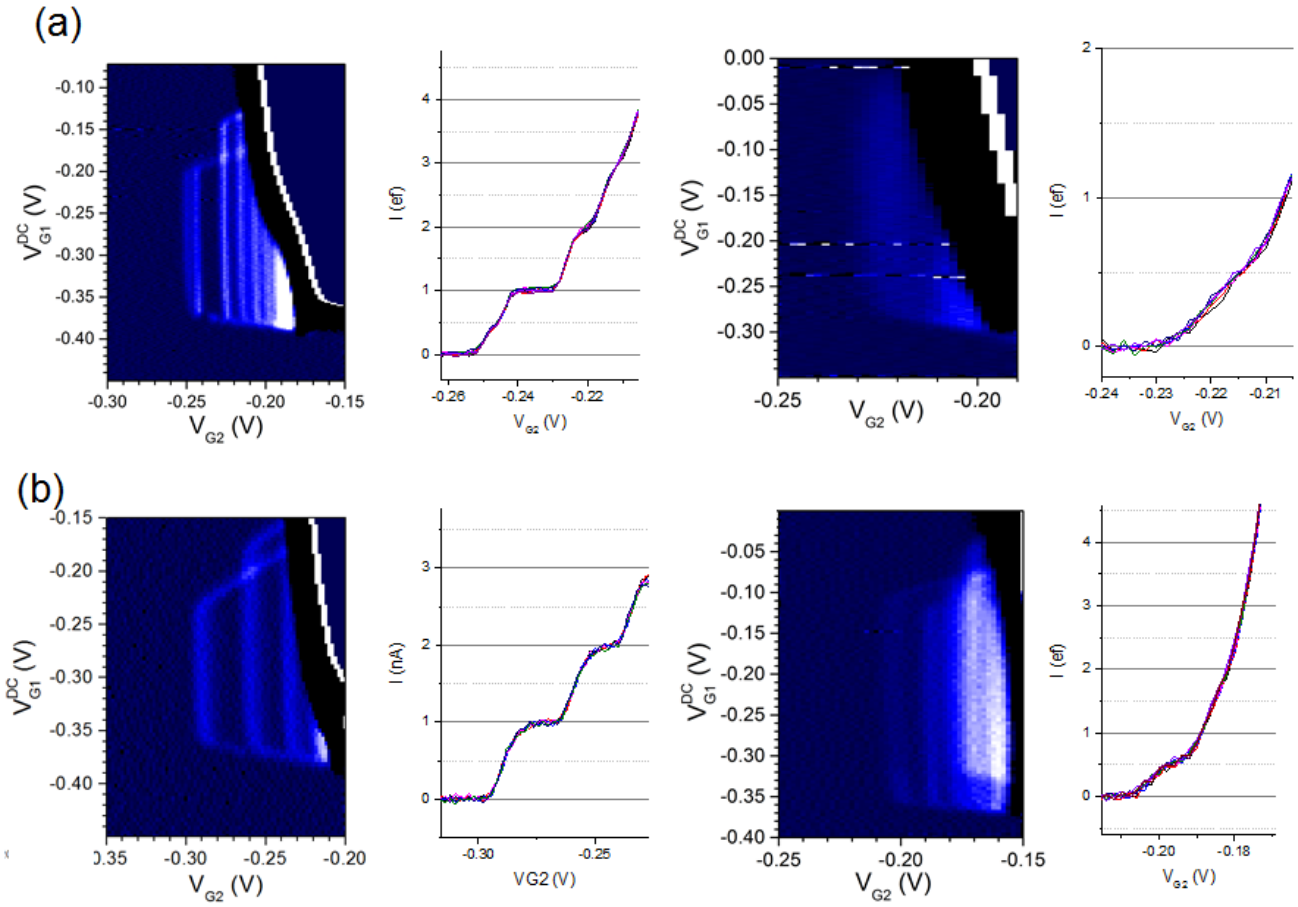


Figure 6.10: Example pump quantisation maps from batch 3. The pumps on this batch are all found to be poor. (a) Performance of the elliptical pump, showing fair (left) and poor (right) quantisation. In the colour map we present a quantisation map (compare with Fig. 1.3(d) for the expected map), and in the right hand plot we present the step-like plot demonstrating current quantisation (compare with Fig. 1.3(c) for an example plot showing good quantisation). (b) The tried and tested circular pump performed similarly, with at best disappointing quantisation.

## 6.6 Next Steps

So, we are no closer to seeing interference. All of our problems have been "technical" - that is, arise from the fabrication, but we could be quite close to them working. Of our design features, we think we have got the Ohmic recipe correct for the next batch such that we can boost the yield of small contacts using Göktaş's recipe. The bridge looks like it is quite reliable now, using the diffuse PMMA. We cannot comment on the effectiveness of the design itself or the other features, but the next batch should allow us to put these features to the test.

For the next batch, we may incorporate a third design variant, which would be a variation of Type A but with a larger ohmic contact (say 2000 nm). Whilst observation of interference would be very difficult owing to the larger area enclosed, it may be important to show we can partition and recombine the current, and test the effectiveness of the bridge conclusively.

We do not know the effectiveness of these designs in resolving the interference pattern; we may find our visibility to be very small, maybe due to differences in path lengths (timing of electron arrival at the second partition), or due to acoustic scattering events. This device will be excellent for studying these processes, even if we cannot see interference, and we can also explore electron wavepacket timing. Hong Ou Mandel type shot noise suppression, another signature of the coherence of the wavepacket, would also be measurable on this device, by measuring the cross correlation of noise between the small ohmic and the detector channels [14, 131, 132].

## 6.7 Conclusions

The interferometers were not a success, partly because of bad luck, and partly because we pushed the current fabrication techniques. However, I am happy we are at the stage where realising the device should be straightforward.

The future work of the interferometer has already begun. There are ongoing separate

studies into fabrication of air bridges: what metal is best, required thickness and method of fabrication and small ohmic contacts, to increase the yield. Pumps are being tested on new wafers to establish what quantum dot size is required for the specific carrier density. With the right small ohmic, bridge and pump, this device becomes very realisable, and we can move on to studying the rich physics it should surely present.

I am happy to have contributed to the group, in particular mapping the LO-phonon emission, which is a plague for hot electron transport, and finding a solution to suppress it. This will allow devices with more complexity and larger path lengths to be fabricated, and the possibilities for multiple paths and pumps becomes extensive. Also, I have contributed to improving the bandwidth of the electron detector barrier, which will become more important as studies start to move towards prescribing electron wavepackets of specified energy and temporal sizes, and establishing times of arrival at barriers.

I have no doubt, using an AC detector, and depletion gates, coherence of the pumped electron wavefunction is possible in the near future, and technological applications of this system are just that bit closer.

# Bibliography


[1] C. W. J. Beenakker. Theory of coulomb-blockade oscillations in the conductance of a quantum dot. *Phys. Rev. B 44 1646*, 1991.

[2] O. Glöckl, U. L. Andersen, and G. Leuchs. *Lectures in Quantum Information, Ch. 30.* Wiley, 2008.

[3] I. M. Ross. The invention of the transistor. *Proc. IEEE, VOL. 86, No. 1*, 1998.

[4] J. H. Neave, P. J. Dobson, B. A. Joyce, and J. Zhang. Reflection high-energy electron diffraction oscillations from vicinal surfaces-a new approach to surface diffusion measurements. *Appl. Phys. Lett. 47 100*, 1985.

[5] S. Clarke and D. D. Vvedensky. Growth mechanism for molecular-beam epitaxy of group-IV semiconductors. *Phys. Rev. B. 37 11*, 1988.

[6] H. L. Störmer, R. Dingle, A. C. Gossard, W. Wiegmann, and M. D. Sturge. Two-dimensional electron gas at a semiconductor-semiconductor interface. *Solid State Comms. 29 (10) 705*, 1979.

[7] T. Mimura, S. Hiyamizu, T. Fujii, and K. Nanbu. A new field-effect transistor with selectively doped GaAs/n-$Al_xGa_{1-x}As$ heterojunctions. *Japan. J. Appl. Phys. 19 5 L225*, 1980.

[8] J. D. Fletcher, P. See, H. Howe, M. Pepper, S. P. Giblin, J. P. Griffiths, G. A. C. Jones, I. Farrer, D. A. Ritchie, T. J. B. M. Janssen, and M. Kataoka. Clock-controlled emission of single-electron wave packets in a solid-state circuit. *Phys. Rev. Lett. 111 216807*, 2013.

[9] B. J. van Wees, H. van Houten, C. W. J. Beenakker, J. G. Williamson, L. P. Kouwenhoven, D. van der Marek, and C. T. Foxon. Quantized conductance of point contacts in a two-dimensional electron gas. *Phys. Rev. Lett. 60 848*, 1988.

[10] T. J. Thornton, M. Pepper, H. Ahmed, D. Andrews, and G. J. Davies. One-dimensional conduction in the 2D electron gas of a GaAs-AlGaAs heterojunction. *Phys. Rev. Lett. 56 1198*, 1986.

[11] A. Palevski, M. Heiblum, C. P. Umbach, C. M. Knoedler, A. N. Broers, and R. H. Koch. Lateral tunneling, ballistic transport, and spectroscopy in a two-dimensional electron gas. *Phys. Rev. Lett. 62 1776*, 1989.

[12] M. W. Keller, J. M. Martinis, N. M. Zimmerman, and A. H. Steinbach. Accuracy of electron counting using a 7-junction electron pump. *App. Phys. Lett. 69 1804*, 1996.

[13] G. Fève, A. Mahé, J.-M. Berroir, T. Kontos, B. Plaçais, D.C. Glattli, A. Cavanna, B. Etienne, and Y. Jin. An on-demand coherent single-electron source. *Science 316, 1169*, 2007.

[14] E. Bocquillon, F. D. Parmentier, C. Grenier, J.-M. Berroir, P. Degiovanni, D. C. Glattli, B. Plaçais, A. Cavanna, Y. Jin, and G. Fève. Electron quantum optics: Partitioning electrons one by one. *Phys. Rev. Lett. 108, 196803*, 2012.

[15] L. P. Kouwenhoven, A. T. Johnson, N. C. van der Vaart, C. J. P. M. Harmans, and C. T. Foxon. Quantized current in a quantum-dot turnstile using oscillating tunnel barriers. *Phys. Rev. Lett. 67, 1626*, 1991.

[16] S. P. Giblin, M. Kataoka, J. D. Fletcher, P. See, T. J. B. M. Janssen, J. P. Griffiths, G. A. C. Jones, I. Farrer, and D. A. Ritchie. Towards a quantum representation of the ampere using single electron pumps. *Nature Comms. 3 930*, 2012.

[17] D. Zumbühl. Semiconductor device fabrication (lecture notes). *University of Basel*, 2014.

[18] Ioffe Physico-Technical Institute. *GaAs entry in* New semiconductor materials, characteristics and properties. *online, http://www.ioffe.ru/SVA/NSM/Semicond/AlGaAs/basic.html*, 1998.

[19] Ioffe Physico-Technical Institute. *AlGaAs entry in* New semiconductor materials, characteristics and properties. *online, http://www.ioffe.ru/SVA/NSM/Semicond/AlGaAs/basic.html*, 1998.

[20] Argonne National Laboratory. Lattice constants and crystal structures of some semiconductors and other materials. *online, http://7id.xray.aps.anl.gov/calculators/crystal_lattice_parameters.html*, 2017.

[21] M. D. Blumenthal, B. Kaestner, L. Li, S. Giblin, T. J. B. M. Janssen, M. Pepper, D. Anderson, G. Jones, and D. A. Ritchie. Gigahertz quantized charge pumping. *Nature Phys. 3 343*, 2007.

[22] A. Fujiwara, N. M. Zimmerman, Y. Ono, and Y. Takahashi. Current quantization due to single-electron transfer in Si-wire charge-coupled devices. *App. Phys. Lett. 84 1323*, 2004.

[23] W. G. van der Wiel, S. De Franceschi, J. M. Elzerman, T. Fujisawa, S. Tarucha, and L. P. Kouwenhoven. Electron transport through double quantum dots. *Rev. Mod. Phys. 75 1*, 2003.

[24] L. P. Kouwenhoven, T. H. Oosterkamp, M. W. S. Danoesastro, M. Eto, D. G. Austing, T. Honda, and S. Tarucha. Excitation spectra of circular, few-electron quantum dots. *Science 278 1788*, 1997.

[25] L. P. Kouwenhoven, D. G. Austing, and S. Tarucha. Few-electron quantum dots. *Rep. Prog. Phys. 64 701*, 2001.

[26] S. Tarucha, D. G. Austing, T. Honda, R. J. van der Hage, and L. P. Kouwenhoven. Shell filling and spin effects in a few electron quantum dot. *Phys. Rev. Lett. 77 3613*, 1996.

[27] S. P. Giblin, S. J. Wright, J. D. Fletcher, M. Kataoka, M. Pepper, T. J. B. M. Janssen, D. A. Ritchie, C. A. Nicoll, D. Anderson, and G. A. C. Jones. An accurate high-speed single-electron quantum dot pump. *New J. Phys. 12 073013*, 2012.

[28] C. Leicht, P. Mirovsky, B. Kaestner, F. Hohls, V. Kashcheyevs, E. V. Kurganova, U. Zeitler, T. Weimann, K. Pierz, and H. W. Schumacher. Generation of energy selective excitations in quantum hall edge states. *Semicond. Sci. Tech. 26 055010*, 2011.

[29] M. Seo, Y.-H. Ahn, Y. Oh, Y. Chung, S. Ryu, H.-S. Sim, I.-H. Lee, M.-H. Bae, and N. Kim. Improvement of electron pump accuracy by a potential-shape-tunable quantum dot pump. *Phys. Rev. B 90 085307*, 2014.

[30] S. J. Wright, M. D. Blumenthal, G. Gumbs, A. L. Thorn, M. Pepper, T. J. B. M. Janssen, S. N. Holmes, D. Anderson, G. A. C. Jones, C. A. Nicoll, and D. A. Ritchie. Enhanced current quantisation in high-frequency electron pumps in a perpendicular magnetic field. *Phys. Rev. B 78 233311*, 2008.

[31] J. D. Fletcher, M. Kataoka, S. P. Giblin, S. Park, H.-S. Sim, P. See, D. A. Ritchie, J. P. Griffiths, G. A. C. Jones, H. E. Beere, and T. J. B. M. Janssen. Stabilization of single-electron pumps by high magnetic fields. *Phys. Rev. B 86 155311*, 2012.

[32] M. Kataoka, J. D. Fletcher, P. See, S. P. Giblin, T. J. B. M. Janssen, J. P. Griffiths, G. A. C. Jones, I. Farrer, and D. A. Ritchie. Tunable nonadiabatic excitation in a single-electron quantum dot. *Phys. Rev. Lett. 106 126801*, 2011.

[33] M. Seo, Y.-H. Ahn, Y. Oh, Y. Chung, S. Ryu, H.-S. Sim, I.-H. Lee, M.-H. Bae, and N. Kim. Improvement of electron pump accuracy by a potential-shape-tunable quantum dot pump. *Phys. Rev. B 90 085307*, 2014.

[34] F. Stein, D. Drung, L. Fricke, H. Scherer, F. Hohls, C. Leicht, M. Götz, C. Krause, R. Behr, E. Pesel, K. Pierz, U. Siegner, F. J. Ahlers, and H. W. Schumacher. Validation of a quantized-current source with 0.2ppm uncertainty. *Appl. Phys. Lett. 107, 103501*, 2015.

[35] M.-H. Bae, Y.-H. Ahn, M. Seo, Y. Chung, J. D. Fletcher, S. P. Giblin, M. Kataoka, and N. Kim. Precision measurement of a potential-profile tunable single-electron pump. *Metrologia 52 195*, 2015.

[36] A. Rossi, T. Tanttu, K. Yen Tan, I. Isakka, R. Zhao, K. Wai Chan, G. C. Tettamanzi, S. Rogge, A. S. Dzurak, and M. Möttönen. An accurate single-electron pump based on a highly tunable silicon quantum dot. *Nano Lett. 2014, 14, 3405*, 2014.

[37] G. Yamahata, S. P. Giblin, M. Kataoka, T. Karasawa, and A. Fujiwara. Gigahertz single-electron pumping in silicon with an accuracy better than 9.2 parts in 10[7]. *Appl. Phys. Lett. 109 013101*, 2016.

[38] M. R. Connolly, K. L. Chiu, S. P. Giblin, M. Kataoka, J. D. Fletcher, C. Chua, J. P. Griffiths, G. A. C. Jones, V. I. Fal'ko, C. G. Smith, and T. J. B. M. Janssen. Gigahertz quantized charge pumping in graphene quantum dots. *Nature Nanotech. 8, 417*, 2013.

[39] S. D'Hollosy, M. Jung, A. Baumgartner, V. A. Guzenko, M. H. Madsen, J. Nygård, and C. Schönenberger. Gigahertz quantized charge pumping in bottom-gate-defined inas nanowire quantum dots. *Nano Lett. 15 (7), 4585*, 2015.

[40] M. R. Astley, M. Kataoka, C. J. B. Ford, C. H. W. Barnes, D. Anderson, G. A. C. Jones, I. Farrer, D. A. Ritchie, and M. Pepper. Non-invasive charge detection in surface-acoustic-wave-defined dynamic quantum dots. *Appl. Phys. Lett. 109 183501*, 2016.

[41] N. M. Zimmerman and M. W. Keller. Electrical metrology with single electrons. *Meas. Sci. Tech. 14 1237*, 2003.

[42] M. W. Keller, F. Piquemal, N. Feltin, B. Steck, and L. Devoille. Metrology triangle using a watt balance, a calculable capacitor and a single-electron tunnelling device. *Metrologia 45 330*, 2008.

[43] F. Piquemal and G. Genevès. Argument for a direct realization of the quantum metrological triangle. *Metrologia 37 207*, 2000.

[44] N. M. Zimmerman, E. Hourdakis, Y. Ono, A. Fujiwara, and Y. Takahashi. Error mechanisms and rates in tunable-barrier single-electron turnstiles and charge-coupled devices. *J. Appl. Phys. 96 5254*, 2004.

[45] S. P. Giblin, P. See, A. Petrie, T. J. B. M. Janssen, I. Farrer, J. P. Griffiths, G. A. C. Jones, D. A. Ritchie, and M. Kataoka. High-resolution error detection in the capture process of a single-electron pump. *Appl. Phys. Lett. 108, 023502*, 2016.

[46] S. P. Giblin, M. Kataoka, J. D. Fletcher, P. See, T. J. B. M. Janssen, J. P. Griffiths, G. A. C. Jones, I. Farrer, and D. A. Ritchie. Rectification in mesoscopic alternating current-gated semiconductor devices. *J. App. Phys 114 164505*, 2013.

[47] B. Kaestner, V. Kashcheyevs, G. Hein, K. Pierz, U. Siegner, and H. W. Schumacher. Robust single-parameter quantized charge pumping. *App. Phys. Lett. 92 192106*, 2008.

[48] B. Kaestner, C. Leicht, V. Kashcheyevs, K. Pierz, U. Siegner, and H. W. Schumacher. Single-parameter quantized charge pumping in high magnetic fields. *Appl. Phys. Lett. 94 012106*, 2009.

[49] V. Kashcheyevs and B. Kaestner. Universal decay cascade model for dynamic quantum dot initialization. *Phys. Rev. Lett. 104 186805*, 2010.

[50] B. I. Halperin. Quantized hall conductance, current-carrying edge states, and the existence of extended states in a two-dimensional disordered potential. *Phys. Rev. B 25 2185*, 1982.

[51] J. K. Jain. *Composite Fermions, Ch. 3.* Cambridge University Press, 2007.

[52] S. Datta. *Transport in Mesoscopic Systems, Ch.1.* Cambridge University Press, 1995.

[53] C. L. Kane and M. P. A. Fisher. *Perspectives in Quantum Hall Effects: Novel Quantum Liquids in Low-dimensional Semiconductor Devices; Ch.4 Edge State Transport.* Wiley, 2004.

[54] M. Heiblum, M. I. Nathan, D. C. Thomas, and C. M. Knoedler. Direct observation of ballistic transport in GaAs. *Phys. Rev. Lett. 55 2200*, 1985.

[55] U. Sivan, M. Heiblum, and C. P. Umbach. Hot ballistic transport and phonon emission in a two-dimensional electron gas. *Phys. Rev. Lett. 63 9*, 1989.

[56] K. J. Thomas, M. Y. Simmons, J. T. Nicholls, D. R. Mace, M. Pepper, and D. A. Ritchie. Ballistic transport in one dimensional constrictions formed in deep two dimensional electron gases. *App. Phys. Lett. 67 109*, 1995.

[57] D. Taubert, C. Tomaras, G. J. Schinner, H. P. Tranitz, W. Wegscheider, S. Kehrein, and S. Ludwig. Relaxation of hot electrons in a degenerate two-dimensional electron system: Transition to one-dimensional scattering. *Phys. Rev. B 83, 235404*, 2011.

[58] N. J. Curson, R. Nemutudi, N. J. Appleyard, M. Pepper, D. A. Ritchie, and G. A. C. Jones. Ballistic transport in a GaAs/AlxGa1-xAs one-dimensional channel fabricated using an atomic force microscope. *App. Phys. Lett. 78 3466*, 2001.

[59] D. B. Chklovskii, K. A. Matveev, and B. I. Shklovskii. Ballistic conductance of interacting electrons in the quantum hall regime. *Phys. Rev. B 47 12605*, 1993.

[60] C. W. J. Beenakker and H. van Houten. Quantum transport in semiconductor nanostructures. *Solid State Phys. 44 1*, 1991.

[61] R. J. Schoelkopf, P. Wahlgren, A. A. Kozhevnikov, P. Delsing, and D. E. Prober. The radio-frequency single-electron transistor (RF-SET): A fast and ultrasensitive electrometer. *Science 280 1238*, 1998.

[62] J. M. Elzerman, R. Hanson, L. H. Willems van Beveren, B. Witkamp, L. M. K. Vandersypen, and L. P. Kouwenhoven. Single-shot read-out of an individual electron spin in a quantum dot. *Nature 430 431*, 2004.

[63] D. Loss and D. P. DiVincenzo. Quantum computation with quantum dots. *Phys. Rev. A 57 (1) 120*, 1998.

[64] J. R. Petta, A. C. Johnson, J. M. Taylor, E. A. Laird, A. Yacoby, M. D. Lukin, C. Marcus, M. P. Hanson, and A. C. Gossard. Coherent manipulation of coupled electron spins in semiconductor quantum dots. *Science 309 2180*, 2005.

[65] N. Johnson, J. D. Fletcher, D.A. Humphreys, P. See, J.P. Griffiths, G.A.C. Jones, I. Farrer, D.A. Ritchie, M. Pepper, T.J.B.M Janssen, and M. Kataoka. Ultrafast voltage sampling using single-electron wavepackets. *Appl. Phys. Lett. 110 102105*, 2017.

[66] J. M. Elzerman, R. Hanson, J. S. Greidanus, L. H. Willems van Bevere, S. De Franceschi, L. M. K. Vandersypen, S. Tarucha, and L. P. Kouwenhoven. Few-electron quantum dot circuit with integrated charge read out. *Phys. Rev. B 67 161308R*, 2003.

[67] J. Waldie, P. See, V. Kashcheyevs, J. P. Griffiths, I. Farrer, G. A. C. Jones, D. A. Ritchie, T. J. B. M. Janssen, and M. Kataoka. Measurement and control of electron wave packets from a single-electron source. *Phys. Rev. B 92, 125305*, 2015.

[68] S. Ryu, M. Kataoka, and H.-S. Sim. Ultrafast emission and detection of a single-electron gaussian wave packet: A theoretical study. *Phys. Rev. Lett. 117 146802*, 2016.

[69] Various, Ed. S. Braunstein, H.-K. Lo, and P. Kok. *Scalable Quantum Computers: Paving the Way to Realization*. J. Wiley and Sons, 2005.

[70] H. M. Wiseman and G. J. Milburn. *Quantum Measurement and Control*. Cambridge University Press, 2011.

[71] D. J. Reilly. Engineering the quantum-classical interface of solid-state qubits. *NPJ Quantum Information 1 15011*, 2015.

[72] Tektronix. Techniques for extending real-time oscilloscope bandwidth (technical brief).

[73] Keysight Technologies. What is the difference between an equivalent time sampling oscilloscope and a real-time oscilloscope? (application note), 2013.

[74] P. Pupalaikis. Digital bandwidth interleaving. *LeCroy technical brief*, 2010.

[75] T. H. O'Dell. *Circuits for Electronic Instrumentation*. Cambridge University Press, 1991.

[76] Agilent Technologies. Techniques to achieve oscilloscope bandwidths of greater than 16 GHz. *Agilent Application Note*, 2010.

[77] M. Kataoka, J. D. Fletcher, and N. Johnson. Time-resolved single-electron wave packet detection. *Phys. Status Solidii B 254 1521*, 2016.

[78] C. H. Bennett and D. P. DiVincenzo. Quantum information and computation. *Nature 404 247*, 2000.

[79] J. Splettstoesser, M. Moskalets, and M. Büttiker. Two-particle nonlocal Aharonov-Bohm effect from two single-particle emitters. *Phys. Rev. Lett. 103 076804*, 2009.

[80] M. Yamamoto, S. Takada, C. Bäuerle, K. Watanabe, A. D. Wieck, and S. Tarucha. Electrical control of a solid-state flying qubit. *Nature Nanotech. 7 247*, 2012.

[81] G. Haack, M. Moskalets, J. Splettstoesser, and M. Büttiker. Coherence of single-electron sources from Mach-Zehnder interferometry. *Phys. Rev. B 84 081303R*, 2011.

[82] M. Büttiker. Four-terminal phase-coherent conductance. *Phys. Rev. Lett. 57 1761*, 1986.

[83] R. C. Ashoori, H. L. Stormer, L. N. Pfeiffer, K. W. Baldwin, and K. West. Edge magnetoplasmons in the time domain. *Phys. Rev. B 45, 3894(R)*, 1992.

[84] N. B. Zhitenev, R. J. Haug, K. v. Klitzing, and K. Eberl. Time-resolved measurements of transport in edge channels. *Phys. Rev. Lett. 71, 2292*, 1993.

[85] H. Kamata, T. Ota, K. Muraki, and T. Fujisawa. Voltage-controlled group velocity of edge magnetoplasmon in the quantum hall regime. *Phys. Rev. B 81 085329*, 2010.

[86] N. Kumada, H. Kamata, and T. Fujisawa. Edge magnetoplasmon transport in gated and ungated quantum hall systems. *Phys. Rev. B 84, 045314*, 2011.

[87] D. T. McClure, Y. Zhang, B. Rosenow, E.M. Levenson-Falk, C.M. Marcus, L.N. Pfeiffer, and K.W. West. Edge-state velocity and coherence in a quantum hall fabry-perot interferometer. *Phys. Rev. Lett. 103 206806*, 2009.

[88] S. Das Sarma and A. Madhukar. Study of electron-phonon interaction and magneto-optical anomalies in two-dimensionally confined systems. *Phys. Rev. B 22 2823*, 1980.

[89] T. W. Hickmott, P. M. Solomon, F. F. Fang, and F. Stern. Sequential single-phonon emission in $GaAs - Al_xGa_{1-x}$ tunnel junctions. *Phys. Rev. Lett. 52 2053*, 1984.

[90] J. S. Blakemore. Semiconducting and other major properties of gallium arsenide. *J. Appl. Phys. 53 R123*, 1982.

[91] A. Mittal, R. G. Wheeler, M. W. Keller, D. E. Prober, and R. N. Sacks. Electron-phonon scattering rates in GaAs/AlGaAs 2DEG samples below 5K. *Surf. Sci. 361-362 537*, 1996.

[92] S. Komiyama, H. Hirai, M. Ohsawa, Y. Matsuda, S. Sasa, and T. Fujii. Inter-edge-state scattering and nonlinear effects in a two-dimensional electron gas at high magnetic fields. *Phys. Rev. B 45 11085*, 1992.

[93] P. J. Price. Hot electrons in a GaAs heterolayer at low temperature. *J. App. Phys. 53, 6863*, 1982.

[94] D. Taubert, G. J. Schinner, H. P. Tranitz, W. Wegscheider, C. Tomaras, S. Kehrein, and S. Ludwig. Electron-avalanche amplifier based on the electronic venturi effect. *Phys. Rev. B 82 161416R*, 2010.

[95] C. Emary, A. Dyson, S. Ryu, H.-S. Sim, and M. Kataoka. Phonon emission and arrival times of electrons from a single electron source. *Phys. Rev. B 93, 035436*, 2016.

[96] S. Das Sarma and J. J. Quinn. Collective excitations in semiconductor superlattices. *Phys. Rev. B 25 7603*, 1982.

[97] L. J. Brillson. *Surfaces and Interfaces of Electronic Materials, Appendix 6.* Wiley, 2012.

[98] B. K. Ridley. *Electrons and Phonons in Semiconductor Multilayers, Ch. 1.* Cambridge University Press, 2009.

[99] J. I. Climente, A. Bertoni, G. Goldoni, and E. Molinari. Phonon-induced electron relaxation in weakly confined single and coupled quantum dots. *Phys. Rev. B 74 035313*, 2006.

[100] D. M. Larsen. Cyclotron resonance of polarons confined to a surface. *Phys. Rev. B 30 4595*, 1984.

[101] J. T. Devreese and A. S. Alexandrov. Fröhlich polaron and bipolaron: recent developments. *Rep. Prog. Phys. 72 066501*, 2009.

[102] S. C. Johnson and T. D. Gutierrez. Visualizing the phonon wave function. *Am. J. Phys 70 227*, 2002.

[103] K. F. Riley, M. P. Hobson, and S. J. Bence. *Mathematical Methods for Physics and Engineering (Third Edition).* Cambridge University Press, 2006.

[104] D. J. Griffiths. *Introduction to quantum mechanics, Ch. 2.* Prentice-Hall, 1995.

[105] Y. Aharonov and D. Bohm. Significance of electromagnetic potentials in the quantum theory. *Phys. Rev. 115, 485*, 1959.

[106] D. J. Griffiths. *Introduction to quantum mechanics, Ch. 10.* Prentice-Hall, 1995.

[107] S. Datta and M. J. McLennan. Quantum transport in ultrasmall electronic devices. *Rep. Prog. Phys. 53 1003*, 1990.

[108] R. Healey. *Gauging What's Real: The Conceptual Foundations of Gauge Theories, Ch. 2.* Oxford University Press, 2007.

[109] M. Peshkin and A. Tonomura. *The Aharonov-Bohm Effect.* 1989.

[110] D. H. Kobe. Berry phase, Aharonov-Bohm effect and topology. *J. Phys. A: Math. Gen. 24 3551*, 1991.

[111] A. D. Stone. Magnetoresistance fluctuations in mesoscopic wires and rings. *Phys. Rev. Lett. 54 2692*, 1985.

[112] R. A. Webb, S. Washburn, C. P. Umbach, and R. B. Laibowitz. Observation of h/e Aharonov-Bohm oscillations in normal-metal rings. *Phys. Rev. Lett. 54 2696*, 1985.

[113] J. D. F. Franklin, I. Zailer, C. J. B. Ford, P. J. Simpson, J. E. F. Frost, D. A. Ritchie, M. Y. Simmons, and M. Pepper. The Aharonov-Bohm effect in the fractional quantum hall regime. *Surface Science 361/362 17*, 1996.

[114] M. Kataoka, C. J. B. Ford, G. Faini, D. Mailly, M. Y. Simmons, D. R. Mace, C.-T. Liang, and D. A. Ritchie. Detection of Coulomb charging around an antidot in the quantum hall regime. *Phys. Rev. Lett. 83, 160*, 1999.

[115] S. Gustavsson, R. Leturcq, M. Studer, T. Ihn, K. Ensslin, D. C. Driscoll, and A. C. Gossard. Time-resolved detection of single-electron interference. *Nano Letters 8 2547*, 2008.

[116] L. V. Litvin, A. Helzel, H.-P. Tranitz, W. Wegscheider, and C. Strunk. Edge-channel interference controlled by Landau level filling. *Phys. Rev. B 78, 075303*, 2008.

[117] D. S. Wei, T. van der Sar, J .D. Sanchez-Yamagishi, K. Watanabe, T. Taniguichi, P. Jarillo-Herrero, B. I. Halperin, and A. Yacoby. Mach-Zehnder interferometry using spin- and valley-polarized quantum Hall edge states in graphene. *Arxiv 1703.00110v1*, 2017.

[118] Y. Ji, Y. Chung, D. Sprinzak, M. Heiblum, D. Mahalu, and H. Shtrikman. An electronic Mach Zehnder interferometer. *Nature 422 415*, 2003.

[119] I. Neder, M. Heiblum, Y. Levinson, D. Mahalu, and V. Umansky. Unexpected behaviour in a two-path electron interferometer. *Phys. Rev. Lett. 96, 016804*, 2006.

[120] J. Splettstoesser, M. Moskalets, and Markus Büttiker. Two-particle nonlocal aharonov-bohm effect from two single-particle emitters. *Phys. Rev. Lett. 103, 076804*, 2009.

[121] D. Dasenbrook, J. Bowles, J. B. Brask, P. P. Hofer, C. Flindt, and N. Brunner. Single-electron entanglement and nonlocality. *New Journal Phys. 18 043036*, 2016.

[122] G. Campagnano, O. Zilberberg, I. V. Gornyi, D. E. Feldman, A. C. Potter, and Y. Gefen. Hanbury Brown Twiss interference of anyons. *Phys. Rev. Lett. 109, 106802.*

[123] P. Samuelsson, E.V. Sukhorukov, and M. Büttiker. Two-particle Aharonov-Bohm effect and entanglement in the electronic Hanbury BrownTwiss setup. *Phys. Rev. Lett. 92 026805*, 2004.

[124] M. Kamada, T. Suzuki, F. Nakamura, Y. Mori, and M. Arai. Investigation of orientation effect on contact resistance in selectively doped AlGaAs/GaAs heterostructures. *Appl. Phys. Lett. 49, 1263*, 1986.

[125] L. Greuter. Fabrication and characterization of ohmic contacts. *Masters' thesis, University of Basel*, 2009.

[126] S. M. Sze and K. K. Ng. *Physics of Semiconductor Devices, Ch. 3.* Wiley, 2006.

[127] K. C. Saraswat. Ohmic contacts - advanced integrated circuit fabrication processes lecture notes. *Stanford University*, 2006.

[128] R. J. Haug. Edge-state transport and its experimental consequences in high magnetic fields. *Semicon. Sci. Tech. 8 131*, 1993.

[129] O. Göktaş. Small alloyed ohmic contacts to 2DES and submicron scale Corbino devices in strong magnetic fields: observation of a zero bias anomaly and single-electron charging. *PhD thesis, Universität Stuttgart*, 2009.

[130] O. Göktaş, J. Weber, J. Weis, and K. von Klitzing. Alloyed ohmic contacts to two-dimensional electron system in AlGaAs/GaAs heterostructures down to submicron length scale. *Physica E 40 1579*, 2009.

[131] E. Bocquillon, V. Freulon, J. M Berroir, P. Degiovanni, B. Plaçais, A. Cavanna, Y. Jin, and G. Fève. Coherence and indistinguishability of single electrons emitted by independent sources. *Science 339 (6123) 1054*, 2013.

[132] S. Olkhovskaya, J. Splettstoesser, M. Moskalets, and M. Büttiker. Shot noise of a mesoscopic two-particle collider. *Phys. Rev. Lett. 101, 166802*, 2008.

# Chapter 7

# Summary

In this work we have continued and developed the previous studies of the single electron output of the NPL electron pump. In chapter 1, we introduced the electron pump. There is much in common with other electron pumps in other systems. In chapter 2, we introduced high - energy edge state transport, which creates a waveguide that the pumped electron propagates in. We detailed a method for detecting electron propagation in this edge state, which we call the electron detector barrier. The detector barrier is capable of identifying the hot electron arrival energy and time to meV and ps resolution. Further, we can use the barrier as a single electron sampling oscilloscope. In a reversal of the method we can use the detector barrier to identify electron energy and arrival time, we can get the electrons to reveal the form of an unknown waveform applied to the detector barrier. We identified the bandwidth of this system, and found it to be very high, in excess of 30 GHz. This could be used as a high bandwidth signal readout in the cryostat, where it would be difficult to get the signal out to room temperature instrumentation without significant loss, owing to the many joints and meters of cabling required.

We used the detector barrier to measure the electron velocity, using a time of flight measurement along a known path length in chapter 3. We believe this is the first direct measurement of electron velocity in this semiconductor system. From the velocity, we derived

the edge potential profile, and found it to be parabolic. At the same time, we realised that we could control the primary mode of relaxation of the electrons - the LO phonon - by use of a surface gate covering the entire electron path.

Chapter 4 detailed the mechanism by which the depletion gate worked to suppress LO-phonon emission. We found the two elegant results that the action of the gate is to change the curvature of the profile, and so reduce the overlap between states, with the scattering rate explained elegantly from Fermi's Golden Rule; secondly, that this has significant technological importance as it allows us to create a lossless state in which coherence could be maintained. We encountered too that the measured rates are in excess of the theory of LO-mode only scattering, and suggest acoustic mode phonons may be responsible for this.

With the possibility that, the LO-mode emission suppressed to be undetectable, coherent transport should be possible in the edge state, we characterised the wavepacket in chapter 5. Here, we measured the arrival time and energy distributions of the wavepacket incident upon the detector, and derived a method to separate the electron wavepacket from the barrier transmission function. We showed successfully the form of the electron distribution is related to the pump's quantum dot potential profile, a key indicator that there is coherence of the wavepacket across the device. We showed we had some limited ability to control the form of this wavepacket by changing the pump operating conditions.

To be conclusive regarding coherence of the wavepacket, we wanted to show interference, which was the subject of chapter 6. Unfortunately, we ran into technical difficulties and the device was not realised. However, we came close, and this final step should be very possible to achieve. Once we have demonstrated this, everything should be in place for work to begin in creating prescribed states, with the detector barrier a read-out.

This work provides many avenues for future work. For example, it should be possible to refine the energy resolution of the detector barrier, so we can search for acoustic phonon emission. We can continue to explore the tunability of the electron wavepacket, by examining other pumping parameters as well as the confining potential due to the pump drive waveform.

Finally, we can work to observe interference, incorporating the new fabrication features. If interference is observed, and we conclude we can maintain a coherent state, we can begin to examine how we can make a prescribed state, which will combine the work of all chapters: the detector barrier as read out, the wavepacket size determined by the pump, the velocity across the device to the detector and low energy scattering events. Eventually detector barriers employing the SES scheme and tuned wavepackets could be interfering with electrons from other pumps, (e.g. a Hong Ou Mandel type geometry), to move towards a quantum information protocol or flying qubit system.